TÉCNICO
LISBOA

Control of Dynamic Stall in a H-Darrieus VAWT Using Blade Leading Edge Protuberances

Afonso Dias Nogueira Capelo Gonçalves

Thesis to obtain the Master of Science Degree in

Mechanical Engineering

Supervisors: Prof. João Manuel Melo de Sousa
Prof. José Manuel da Silva Chaves Ribeiro Pereira

Examination Committee

Chairperson: Prof. Carlos Frederico Neves Bettencourt da Silva
Supervisor: Prof. José Manuel da Silva Chaves Ribeiro Pereira
Member of the Committee: Prof. João Manuel Ribeiro Costa Baltazar

December 2021

Acknowledgements

I would like to thank professor João M. M. de Sousa for all the guidance, expertise, availability, and for the opportunity to perform this work as my master thesis. Furthermore, I would also like to thank professor José M. C. Pereira for his availability, support and indispensable knowledge.

Resumo

As perdas dinâmicas afectam a grande maioria das turbinas eólicas de eixo vertical; no entanto, o défice de desempenho associado é de especial relevância em turbinas de menores dimensões como, por exemplo, no caso da aplicação em áreas urbanas. No trabalho descrito nesta tese, foram aplicadas protuberâncias sinusoidais aos bordos de ataque de uma turbina com o intuito de avaliar experimentalmente a eficácia destas modificações no controlo das perdas dinâmicas mencionadas.

Um estudo numérico foi realizado em primeiro lugar, de maneira a estabelecer a geometria optimizada do bordo de ataque que foi posteriormente testada no túnel de vento. Para tal, construíram-se duas turbinas e também um sistema para a medição de desempenho das mesmas.

As medições do túnel de vento demonstraram um aumento considerável do coeficiente de potência da turbina modificada face ao desempenho da turbina base. O aumento relativo de C_P foi de 46% a 20% para uma gama de velocidades de escoamento entre 5.5 m/s e 9 m/s. A turbina modificada também revelou uma capacidade de arranque substancialmente melhor. A influência da velocidade especifica (*tip speed ratio*) no comportamento da turbina não foi afectada pelas modificações sinusoidais do bordo de ataque.

Palavras-chave: Turbina eólica de eixo vertical, perda dinâmica, estudo experimental, mecânica de fluidos computacional, protuberâncias de bordo de ataque, geradores de vórtices

Abstract

Dynamic stall flow conditions affect the performance of most Vertical Axis Wind Turbine (VAWT) designs; however, the associated losses are especially relevant in smaller turbines, such as those typically used in urban environment applications. The work described in this dissertation experimentally evaluated the efficacy of leading edge protuberances in controlling the aforementioned stall behaviour.

A numerical study was first performed to define the optimised leading edge geometry to be subsequently tested in the wind tunnel. A custom experimental setup was also developed for this purpose.

The wind tunnel measurements of the modified turbine showed significant performance gains over the baseline and a considerably improved self-starting behaviour. The power coefficient increase was between 46% and 20% for wind speeds ranging from 5.5 m/s to 9 m/s. The tip speed ratio behaviour of the studied turbine was not meaningfully affected by the leading edge protuberances.

Contents

List of Figures

List of Tables

List of Symbols

Greek symbols

α - Angle of attack [°]

α_{ss} - Static stall angle of attack [°]

β_Q - Absolute systematic errors in torque measurements [$N \cdot mm$]

β_U - Absolute systematic errors in flow velocity measurements [m/s]

ε_{Cp} - Absolute random errors in C_P measurements [-]

ε_Q - Absolute random errors in torque measurements [$N \cdot mm$]

ε_r - Absolute random errors in angular velocity measurements [rpm]

θ - Rotor azimuth angle [°]

λ - Tip speed ratio [-]

λ_{Cpmax} - Tip speed ratio at which max C_p is achieved [-]

λ_{vg} - Wavelength of leading edge protuberances [m]

μ_t - Turbulent (eddy) viscosity [$kg/m \cdot s$]

ν - Kinematic viscosity [m^2/s]

ρ - Specific mass [kg/m^3]

σ - Rotor solidity [-]

Ω - Rotor angular velocity [rad/s or rpm]

Roman symbols

a - Axial-induction factor [-]

A - Rotor swept area [m^2]

A_{vg} - Amplitude of leading edge protuberances [m]

AR - Rotor aspect ratio (shape factor) [-]

AR_b - Blade aspect ratio [-]

c - Blade chord [m]

C_Q - Torque coefficient [-]

C_P - Power coefficient [-]

D - Rotor diameter [m]

$eRPM$ - Electric rotational speed [$rpm \cdot pole\ pairs$]

F_c - Centripetal force [N]

F_D - Drag force [N]

F_N - Normal force component [N]

F_L - Lift force [N]

F_T - Tangential force component [N]

g - Gravitational acceleration [m/s^2]

H - Rotor height (blade span) [m]

I - Motor current [A]

k - Reduced frequency [Hz]

K_V - Motor velocity constant [rpm/V]

K_T - Motor torque constant [$N \cdot m/A$]

m - mass [kg]

N - Number of blades [-]

P - Turbine power [W]

P_{atm} - Atmospheric pressure [Pa]

P_∞ - Power in free-stream flow [W]

Q - Torque [$N \cdot m$]

Q_m - Motor torque [$N \cdot m$]

R - Rotor radius [m]

Re_c - Chord Reynolds number [-]

$R_{specific}$ - Specific gas constant [$J/kg \cdot K$]

t - Time [s]

T_{air} - Air temperature [K]

U - Local flow (wind) velocity [m/s]

U_∞ - Free-stream flow (wind) velocity [m/s]

V - Tangential velocity [m/s]

W - Apparent velocity [m/s]

y^+ - Non-dimensional wall distance in wall units [-]

z - Vertical coordinate (co-linear with turbine axis) [m]

List of Acronyms

2D Two-Dimensional.

3D Three-Dimensional.

ADC Analog-to-Digital Converter.

CFD Computational Fluid Dynamics.

DES Detached Eddy Simulations.

DNS Direct Numerical Simulations.

FDM Fused Deposition Modelling.

HAWT Horizontal Axis Wind Turbine.

LES Large Eddy Simulations.

LSWT Low-Speed Wind Tunnel.

RANS Reynolds-Averaged Navier–Stokes.

SST Shear Stress Transport.

URANS Unstedy Reynolds-Averaged Navier–Stokes.

VAWT Vertical Axis Wind Turbine.

1   Introduction

Horizontal Axis Wind Turbines (HAWTs) have long been established as the best turbine configuration for large scale onshore and offshore wind power production. For smaller scale power generation, however, the advantages offered by lift type Vertical Axis Wind Turbine (VAWT) designs can outweigh the disadvantages that typically make them less ideal in larger scale scenarios. As such, vertical axis architectures are often more suitable for smaller scale wind power production than the more commonly adopted HAWTs.

These advantages range from an intrinsic insensitivity to wind direction and lower noise production to an overall better performance under turbulent and skewed flow conditions, which makes VAWTs especially appropriate to urban areas and, in general, environments with transient and unsteady wind characteristics.

Nevertheless, complex rotor aerodynamics due to constantly changing angles of attack and poor self-starting behaviour are still characteristic of VAWT designs, which contribute to an altogether typically lower efficiency, particularly in smaller turbines and at lower blade speeds.

1.1   Main objectives

The main purpose of the work described in this thesis was to develop a small vertical axis turbine, and the associated performance measuring setup, in order to experimentally investigate the efficacy of a promising blade modification—leading edge protuberances as vortex generators—in reducing the dynamic stall effects and thus increasing the efficiency of a small scale vertical axis wind turbine. CFD models were also to be employed to aid the design of a suitable modified blade geometry.

Several other CFD studies have been performed on this leading edge morphology, both in fixed wings and in wind turbines, but only one experimental study has been published on the contribution to the startup behaviour of a VAWT [1]. To the author's knowledge, the improvement of a VAWT's efficiency under nominal operation through the use of leading edge protuberances has yet to be experimentally tested.

1.2   Topic overview

Wind turbines can generally be differentiated between lift (Fig. 1.1 (a) and (b)) and drag-type designs (Fig. 1.1 (c)), where the lift-driven configurations are the most commonly studied and adopted, mainly thanks to significantly greater efficiency. Regarding Vertical Axis Wind turbines, the most established design is the straight bladed Darrieus machine (or H-Darrieus, Fig. 1.1 (b)).

As mentioned above, VAWT designs, and more particularly H-Darrieus designs, present many benefits in comparison with the more typical HAWT configuration:

- The vertical axis design, where the rotor axis is always perpendicular to the horizontal wind direction, has an inherent insensitivity to wind direction, requiring no yaw mechanism to align the rotor with the flow.

(a) Darrieus   (b) H-Darrieus   (c) Savonius
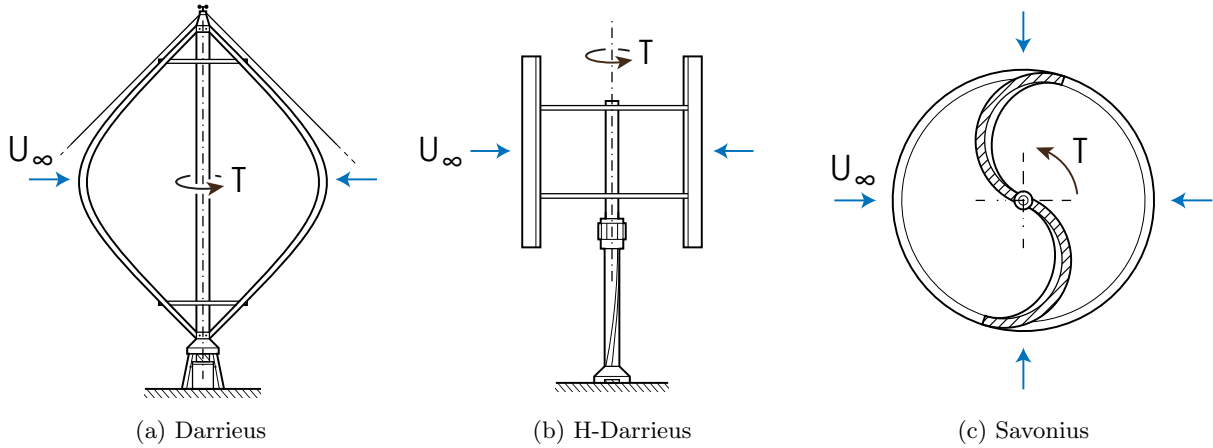
Figure 1.1: Lift-type Darrieus turbines (a) and (b), and Drag-type Savonius turbine (c) [2].

- The Performance of VAWTs have also been shown not to suffer as much with complex and unsteady wind conditions as HAWTs do. Möllerström *et al.* [3] recorded the influence of turbulence in a H-Darrieus rotor over a period of 14 months and showed how suitable the design is to environments with turbulent winds (e.g., urban environments [4]). Additionally, Mertens *et al.* [5] studied the performance of a H-rotor turbine in skewed flow, also a common situation in urban environments, where the wind direction is not perpendicular to the vertical rotor axis, and reported a performance increase in such conditions. Ferreira *et al.* [6] showed similar results in skewed flow and described how the performance increase is an outcome of the changes in the interaction between the upwind and the downwind rotor sections.

- The optimal shape of H-Darrieus rotor blades is often considerably simpler than those of its horizontal axis counterparts, from aerodynamic, structural and manufacturing complexity points of view. Even helical Gorlov rotors (Fig. 7.1), that do not present the same structural and manufacturing simplicity, can still be easier to study, thanks to blade profiles and geometric angles of attack that are constant along the span.

- In a turbine with a vertical axis design, the gearbox and all the power generation components can be placed lower down, or even at the base of the assembly, which can be a major advantage, especially in larger scale architectures.

- Due to the typically lower tip speed ratios required to achieve maximum power, VAWTs often generate less noise noise than HAWTs.

- In the case of wind farms, with multiple turbines placed next to each other, VAWTs can be placed closer together without suffering from the interaction with the upwind turbines' wake [7]. In fact, specific layouts can increase the total power output [8], [9].

Nevertheless, VAWTs present several significant disadvantages that still justify the prevalence of HAWT designs in most environments.

- Darrieus and H-Darrieus turbines are generally less efficient than comparable HAWT design. Some designs also present poor self-starting performance.

- A contributing factor for this lower performance is an inability to access higher quality winds present at higher sections of the atmospheric boundary layer, seeing how HAWTs are normally taller for the same swept area.

- A disadvantage specific of straight bladed Darrieus turbines is the fluctuation of rotor torque throughout each rotation, which poses added wear and fatigue loading to the rotor, drivetrain and electric components. This issue is often mitigated with more complex helical rotor designs.

- High blade bending moments from centrifugal loads, especially in small scale turbines, see 1.2.3.

1.2.1 H-Darrieus VAWT working principle

All lift driven wind turbines generate their torque through the aerodynamic lift generated by one or more rotating blades, however the aerodynamics of a VAWT's rotor are more complex than those of a fixed wing. The simplified 2D schematic in Fig. 1.2 shows the velocity and force kinematics that govern the rotor aerodynamics of a three bladed Darrieus VAWT.
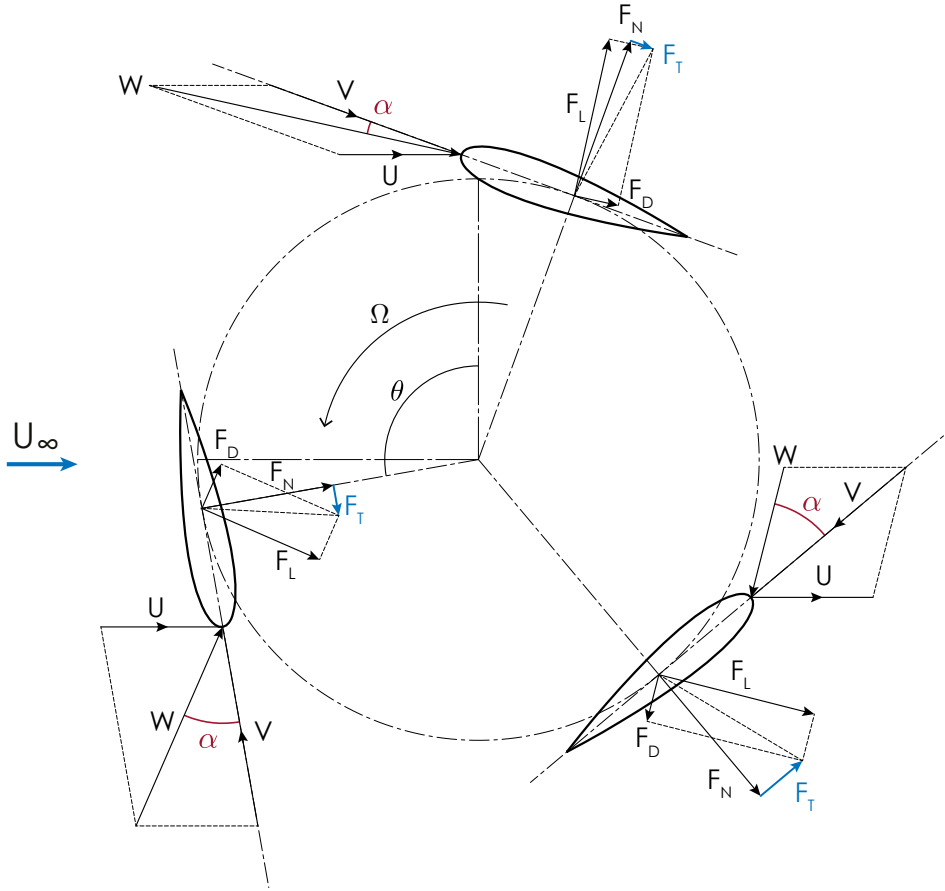
Figure 1.2: VAWT velocity and force vectors.

Apparent wind velocity

The velocity triangle that describes the apparent wind velocity experienced by each rotating blade element, W, comprises the tangential velocity component, V, from the rotor's angular velocity, Ω:

$$V = -\Omega \times R \tag{1.1}$$

and the local wind velocity, U.

Considering U as the freestream wind velocity (i.e., $a = \frac{U_\infty - U}{U_\infty} = 0 \rightarrow U = U_\infty$) and neglecting the rotor effects on the incoming flow, the apparent velocity is the sum of the tangential velocity vector and the local wind vector:

$$W = V + U \tag{1.2}$$

Angle of attack

The angle of attack of each blade relative to the apparent flow velocity, α, will thus vary with the rotor azimuth angle, θ, following:

$$\alpha = cos^{-1}\left(\frac{W \cdot -\hat{i}_{chord}}{\|W\|}\right) \ , \quad \hat{i}_{chord} = \begin{bmatrix} -cos\theta \\ -sin\theta \end{bmatrix} \tag{1.3}$$

where $\hat{i}_{chord}$ is the unit vector that defines the chord line direction.

In a more conventional fixed wing reference frame, where the outside blade surface is equivalent to the wing's upper (suction) surface, and the angle of attack is positive if the direction of the approaching flow is below the chord line, α is given by:

$$\alpha = \begin{cases} -cos^{-1}\left(\frac{W \cdot -\hat{i}_{chord}}{\|W\|}\right) & 0° \leq \theta < 180° \\\\ cos^{-1}\left(\frac{W \cdot -\hat{i}_{chord}}{\|W\|}\right) & 180° \leq \theta < 360°. \end{cases} \tag{1.4}$$

Equation (1.3) can also be written in function of the tip speed ratio, λ:

$$\alpha = tan^{-1}\left(\frac{sin\theta}{\lambda + cos\theta}\right), \tag{1.5}$$

where tip speed ratio is defined as

$$\lambda = \frac{\Omega R}{U}. \tag{1.6}$$

To better illustrate the oscillation of the incident flow on each blade during a single rotation, Eq. (1.5) is plotted for multiple values of tip speed ratio in Fig. 1.3.

For $\lambda < 1$, the angle of attack of the blade will vary between $\alpha = 0°$ and $\alpha = 180°$ in the upwind section ($0° < \theta < 180°$) and between $\alpha = -180°$ and $\alpha = 0°$ on the downwind side ($180° < \theta < 360°$). At $\lambda = 1$, however, α will not exceed $\pm 90°$. Only at $\lambda > 1$ will the flow start approaching the profile from the front in every rotor position, with $\alpha = 0$ at $\theta = 180°$.

As the tip speed ratio increases, the angle of attack curve will get progressively smoother with decreasing amplitude.

Rotor torque and power

The aerodynamic lift and drag forces (F_L, F_D) developed by the blade's profile are also dependent on the azimuth angle, seeing how they are a result of the apparent incoming flow's angle of attack. The contribution of the aerodynamic forces to the total rotor torque, T, is conveyed more clearly by decomposing F_L and F_D into normal and tangential force components; F_N and F_T:

$$F_N = F_L cos\alpha + F_D sin\alpha \tag{1.7}$$

$$F_T = F_L sin\alpha - F_D cos\alpha. \tag{1.8}$$

4
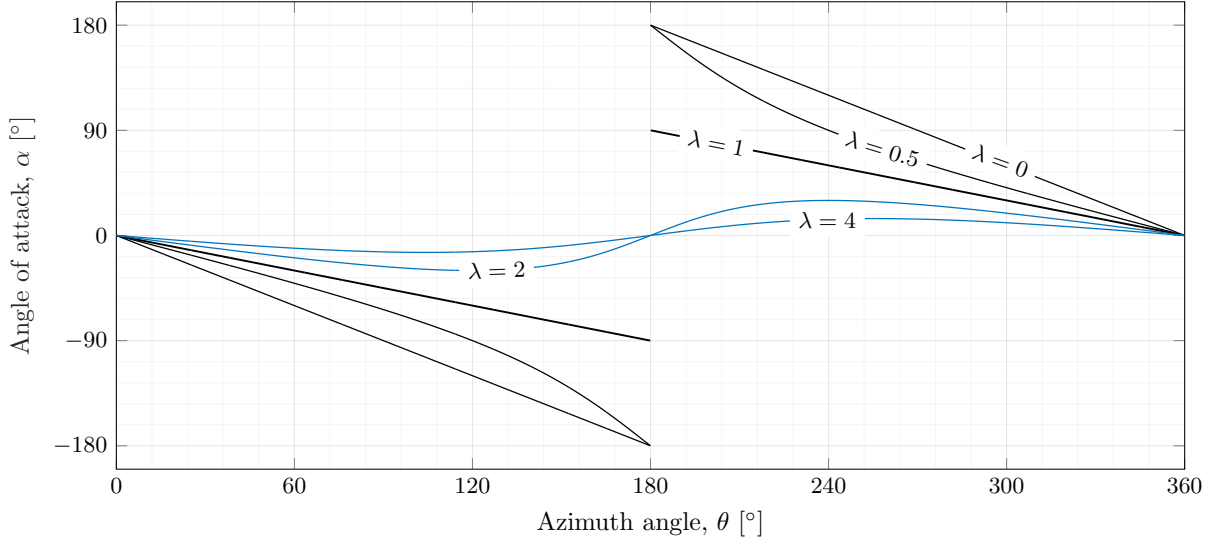
Figure 1.3: Angle of attack of one blade during one rotation.

The blade's pitching moment is usually neglected in the rotor torque calculation as it is relatively small and with opposing directions that cancel out between the upwind and downwind parts of the rotation.

The blade torque and power can subsequently be calculated from F_t:

$$Q = F_T R \tag{1.9}$$

$$P = Q\,\Omega. \tag{1.10}$$

Generally, it is more convenient to use the dimensionless torque and power coefficients, C_Q and C_P, where the latter is especially useful to compare the efficiency of different turbines. Both are, respectively, given by:

$$C_Q = \frac{Q}{\frac{1}{2}\rho U_\infty^2 RA} \tag{1.11}$$

$$C_P = \frac{P}{P_\infty} = \frac{P}{\frac{1}{2}\rho U_\infty^3 A}, \tag{1.12}$$

where A is the rotor swept area ($A = 2RH$ for a straight bladed VAWT).

Fig. 1.4 shows the coefficient of torque of a three balded H-Darrieus turbine for one full rotation. As with most other parameters, the torque produced by the rotor also varies significantly with the azimuthal position of the blades.

Typically, each blade produces the majority of its torque as it moves through the upwind region, with the peak generally just before $\theta = 90°$, hence the three torque peaks shown in this plot.

Flow curvature

The oscillating flow around each blade, and its changing incidence angle, causes the lift curve of the profile to diverge from the static airfoil values. This behaviour is exacerbated by the curved nature of the flow, as seen from the blade's rotating reference frame, which results in a disturbance to the lift generation comparable to the effects of camber on traditional airfoils under linear flow conditions—i.e., virtual camber (Fig.1.5).

Considering also the chord length of the blades over the curved flow, it is apparent that the angle
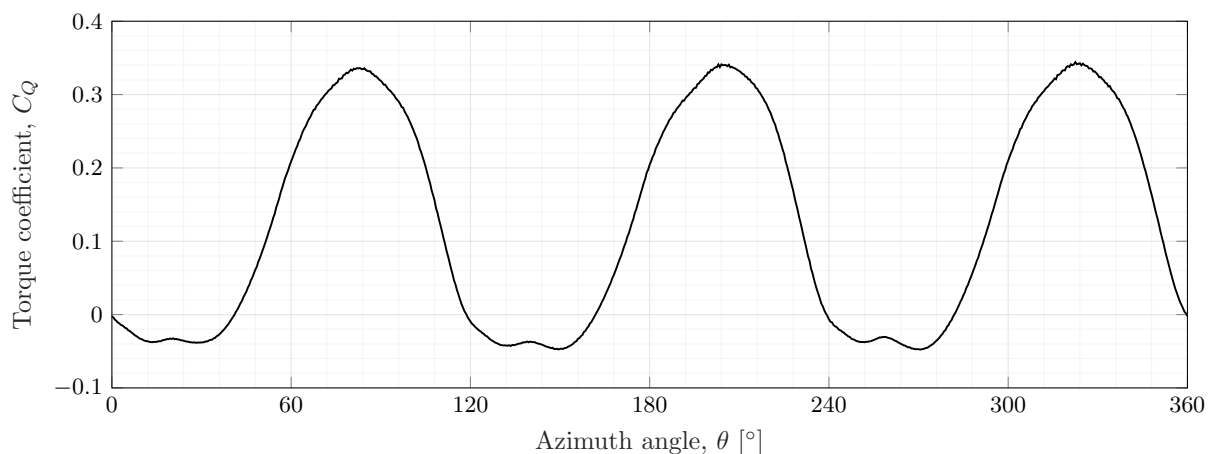
Figure 1.4: C_Q curve of a three bladed Darrieus VAWT operating at $\lambda = 1.65$ - data from infinite blade CFD study.

(a) Curved flow around profile

(b) Equivalent camber in linear flow
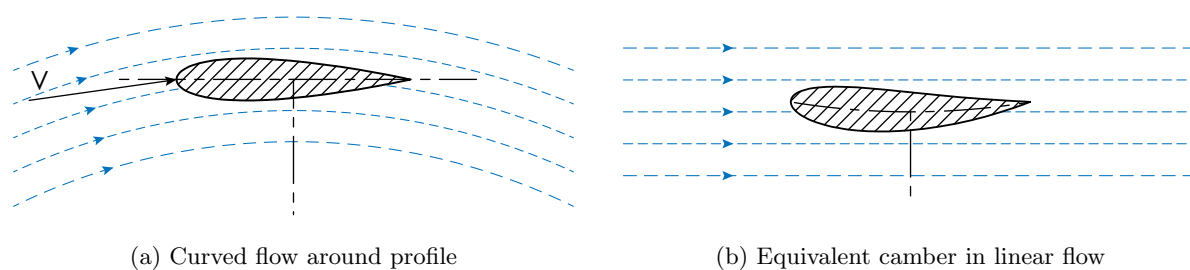
Figure 1.5: Virtual camber.

of attack will vary along the profile and that the effective angle of attack at the leading edge is slightly different, seeing that the tangential velocity, V is no longer tangential with the chord line, as shown in Fig.1.5 (a).

The amount of induced camber and the significance of these effects will vary with λ and solidity, σ, defined as [1]:

$$\sigma = \frac{Nc}{2R}, \tag{1.13}$$

being more relevant for higher solidity rotors, where c is larger in comparison with the total circumference of the rotor.

1.2.2 Dynamic stall

Dynamic stall is a major contributing factor to the typically lower efficiency of VAWTs in the low tip speed ratio range, which consequently also degrades the start up performance and the overall efficiency in transient wind conditions.

This flow phenomenon normally occurs at $\lambda < 5$ [10], precisely as a result of the oscillating nature of the flow over the blades' surfaces, when the effective angle of attack exceeds the static stall angle of the airfoil, α_{ss}.

Figure 1.6 shows the amplitude of the variation of α as a function of tip speed ratio. It is evident, also

---

[1] Some authors define solidity with the radius, R, instead of the diameter, $D = 2R$, doubling the σ values as a result.

from Fig. 1.3, that as λ decreases, the value of the maximum and minimum angle of attack increases, surpassing α_{ss} (measured to be around $\alpha_{ss} = \pm 10.5°$ by Laneville and Vittecoq [10] for a NACA0018 airfoil at $Re = 3.8 \times 10^4$) in progressively larger sections of the rotation cycle.
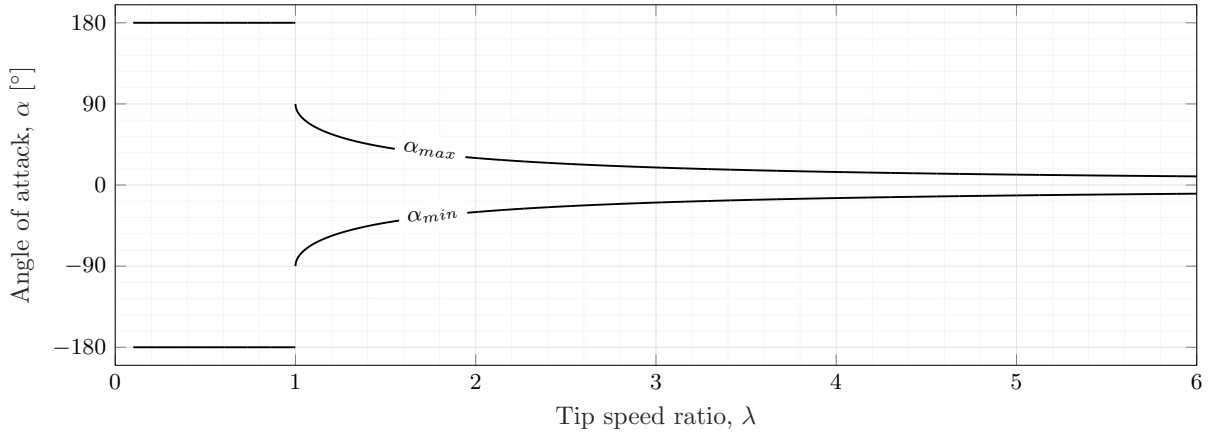
Figure 1.6: Maximum and minimum angle of attack as a function of λ.

Beyond the critical angle of attack, the flow detaches from the airfoil surface, resulting in and abrupt drop in lift and increase in drag. However, the high rate of change in direction of the incident flow produces a hysteresis effect on the lift curve, delaying the onset of stall and prompting and increase in the peak lift value, see Fig. 1.7.
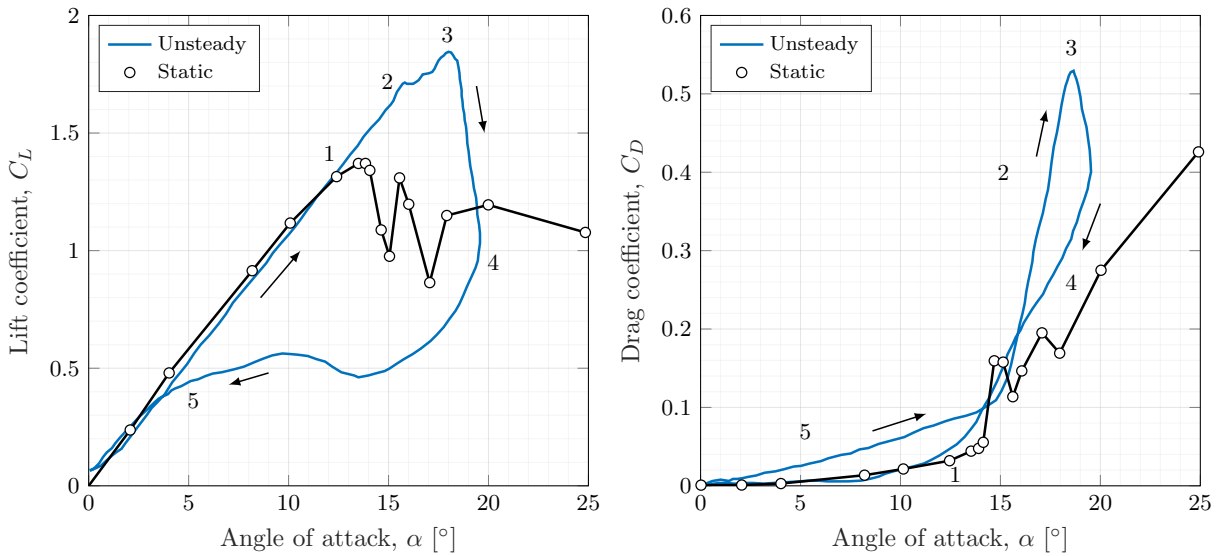
Figure 1.7: Dynamic and static loads of airfoil during dynamic stall from [11].

The overall structure and morphology of the flow surrounding an airfoil during the dynamic stall process was described by Leishman [11] (see also Fig. 1.8), as summarised bellow.

As the angle of attack increases from low incidence angles and exceeds α_{ss} (stage 1), the previously attached suction side boundary layer starts to develop some flow reversal just before the trailing edge. This phase represents an unsteady response of the boundary layer and the subsequent delay in the start of flow separation, also aided by the effects of virtual camber, which reduces the adverse pressure gradient. As the increase in angle of attack progresses, the flow reversal advances toward the leading edge.

The progression of this flow reversal promotes the formation of a leading edge vortex (stage 2), which provides additional lift while over the airfoil surface and moves the centre of pressure rearward, as the

7

vortex grows, detaches and is swept downstream, towards the trailing edge (from stage 2 to stage 3). Additionally, a counter-rotating vortex is typically formed in the trailing edge.

After this leading edge vortex reaches the trailing edge and is shed into the wake, it can no longer maintain the flow curvature over the profile that was prolonging the lift generation. As such, when stage 4 is reached, the flow has progressed in to full separation; therefore, the lift coefficient has dropped abruptly.

When the flow's incidence angle returns to a low enough value, the flow reattachment can occur, accompanied by the subsequent recovery of the aerodynamic forces, stage 5 in Fig. 1.7. Nevertheless, this process can be significantly delayed by the interaction of the shed vortices and by the virtual camber effects, prolonging the reattachment of the flow from the fully separated state, as the reattachment point moves towards the leading edge. Consequently, the angle of attack can fall far below the static stall value before the flow can be considered as fully reattached.
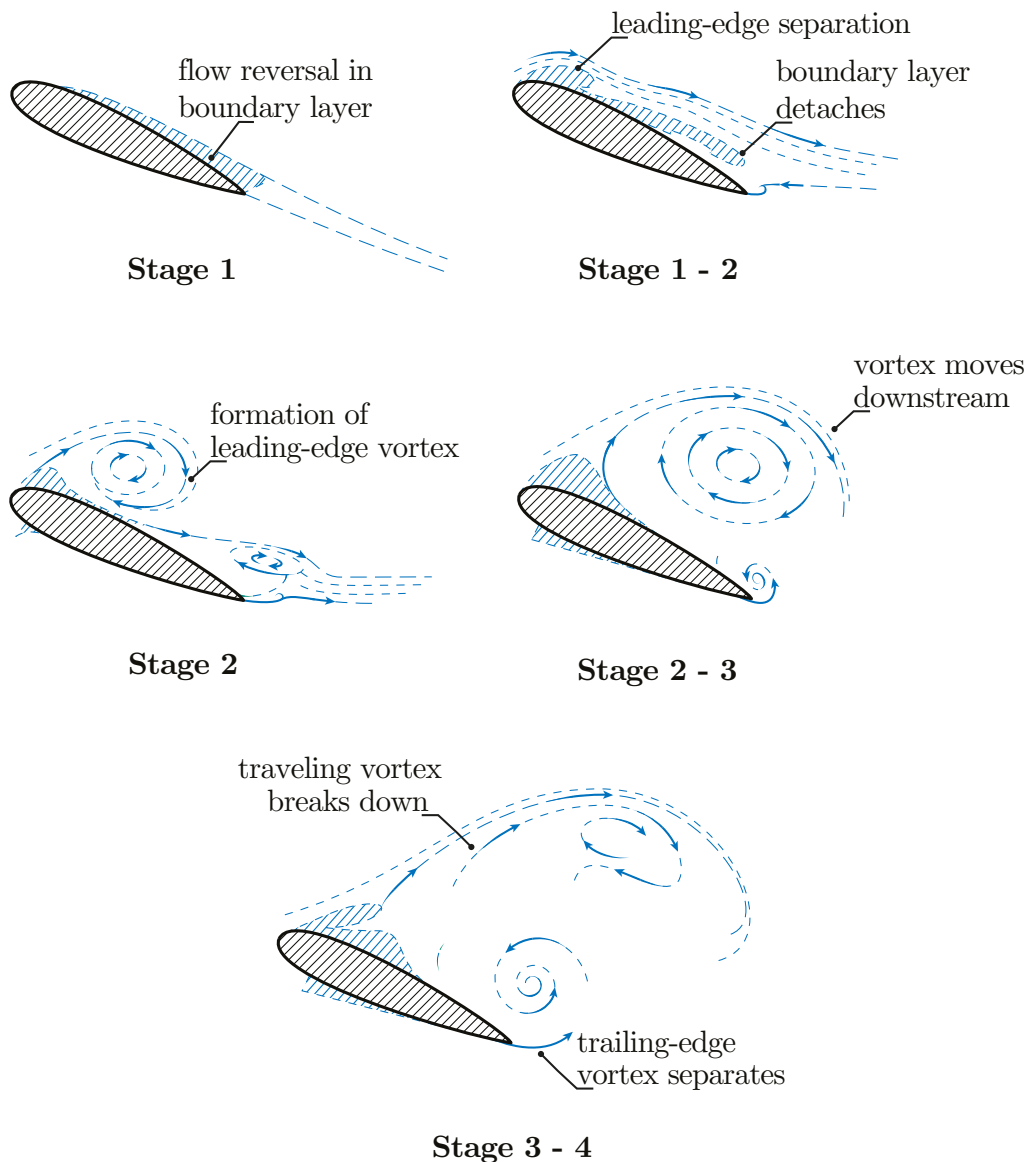
Figure 1.8: Typical flow structure over airfoil during dynamic stall (adapted from [2] with data cited in [12] and complemented with information from [11].

The tip speed ratio, λ, was already established as the operational variable that most influences the intensity and significance of dynamic stall. However, through the definition of the reduced frequency, k,

(Eq. 1.14)—a non-dimensional parameter that can be used to characterise the level of unsteadiness of a system—it is possible to also identify the ratio $c\,/\,D$ as a relevant variable to the degree of unsteadiness of a specific tip speed ratio.

$$k = \frac{\Omega c}{2U} = \frac{c}{2R}\lambda = \frac{c}{D}\lambda \tag{1.14}$$

The ratio $c\,/\,D$ is equivalent to the solidity ($\sigma = \frac{Nc}{2R}$) if the number of blades, N, is considered constant. The conclusion is that the effects of dynamic stall will thus scale with the solidity ratio.

Fujisawa and Shibuya [13] also visualised the flow around a rotor in dynamic stall and reported that the wake of the stall process described above develops into two counter-rotating vortices for each blade rotation. Said vortices will travel downstream and likely impact the performance of the downwind portion of the rotor, as they interact with the blades in this section (Fig. 1.9). The structure of the flow was reported to be somewhat independent of the tip speed ratio, however the blade position, θ, at which each vortex pair is formed was shown to vary with said parameter.
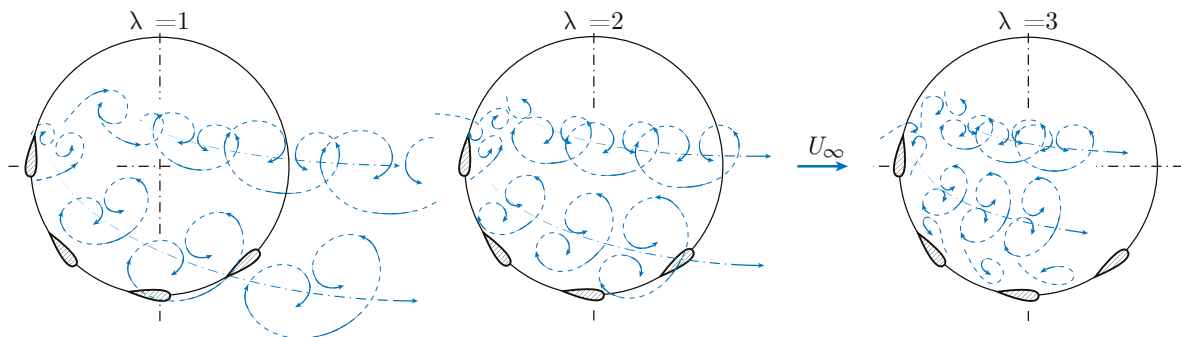
Figure 1.9: Vortex shedding through rotor during dynamic stall, adapted from [2] (see also [13]).

1.2.3 Relevance of improving performance of small scale turbines under dynamic stall

The dynamic stall effects can be mitigated in large vertical axis turbines just by increasing the operational tip speed ratio and thus preventing the incident flow from exceeding the critical angle of attack (at least during nominal operation). In turn, the same cannot be accomplished in rotors with small diameters without a very significant increase in the structural loads.

Whereas λ is proportional both to the turbine rotational speed, Ω, and to the rotor diameter, D, (Eq. 1.6), the centripetal force applied to each blade is also proportional to D but scales with the square of the rotational speed:

$$F_c = \frac{mV^2}{R} = m\Omega^2 R \tag{1.15}$$

In essence, if the rotor diameter can not be widened, the same increase in tip speed ratio is only achieved by proportionally increasing Ω, which is accompanied by the subsequent squared centripetal loads.

As such, improving turbine performance under dynamic stall is especially relevant to small scale VAWT power generation, where this turbine design is often the more appropriate configuration.

1.3 State of the art

Significant research on VAWT design and performance has been carried out throughout the years. The first major studies were conducted in the 1970s at the Sandia National Laboratories, which provided a great deal of data on the design of lift type VAWTs. Such initial research ranges from theoretical performance prediction models [14] and wind tunnel test of a small scale turbine ($D = 2m$) [15] to studies of large scale turbines: a 17 meter [16] and a 34 meter [17] turbine.

Until now, numerous experimental and computational studies have been published, further describing the design and behaviour of VAWTs.

Specifically on H-Darrieus configurations, examples are: the numerical analysis performed by Bianchini *et al.* [18], that provides several aerodynamic design guidelines; the investigation by Rezaeiha *et al.* on the impact of solidity and number of blades on turbine performance [19]; and the experimental work of Du *et al.*, where the influence of several parameters was also investigated [20]. A more comprehensive review of the design guidelines described in the available research is performed in chapter 2, concerning several dimensional and operational variables.

More recently, plenty of studies have been published regarding potential improvements to the H-Darrieus rotor designs and use cases where VAWTs are possibly more suitable than the established HAWT designs, like small turbines in urban environments and dense wind farms (as discussed above), [3]–[9].

In the case of small vertical axis turbines, hindered by the effects of dynamic stall, many flow control solutions have been studied. Also of interest, are other studies of passive and active control methods applied to static wings and HAWTs to improve performance under similar dynamic stall conditions.

Dynamic stall control

Various passive and active dynamic stall control measures have been researched. Joo *et al.* [21] employed a nose droop and a Gurney flap to a rotor airfoil (NACA0012) and showed an improvement in the aerodynamic forces generated in dynamical stall conditions. Similarly, the use of fixed slats was investigated by Carr *et al.* in [22], where the authors reported a delay on the onset of stall for lower angles of attack and a reduction in the severity of stall for larger angles.

Vortex generators have also been studied and used in many fields as a way to suppress or delay separation in quasi-static conditions [23]. Concerning wind turbines, Zhu *et al.*, [24] and [25], analysed the effects of more traditional vortex generators on a oscillating airfoil (commonly used in wind turbines), using URANS simulations with the SST $k-\omega$ turbulence model. The authors reported an effective delay of dynamic stall and an increase in the maximum C_L. Tavernier *et al.* [26] performed a similar experimental study and also described an increase in the maximum lift, stall angle and drag.

Gerontakos and Lee [27], [28] experimented with active trailing and leading edge flaps, with positive results in the first case. Boundary layer blowing and suction methods were investigated in [29] and [30], respectively. McCloud *et al.* [29] reported a successful delay in the stall boundary and Karim *et al.* [30] showed the usefulness of the leading edge suction strategy they used in partially suppressing the dynamic stall vortices developed in the airfoil's suction side. Magill and McManus [31] also showed positive results through the use of pulsed vortex generator jets. Similarly, Yen and Ahmed [32] investigated the use of synthetic jets on a VAWT and demonstrated improved dynamic stall control for low tip speed ratios.

Another promising active technique, specific to H-Darrieus turbines, are synchronous variable pitch blades, where the angle of attack oscillations are mitigated by varying the pitch of each blade continuously. Firdaus *et al.* [33] performed numerical simulations and wind tunnel tests on a turbine with a variable pitch mechanism at low tips speed ratios and the increase in power output was clear.

Leading edge protuberances vortex generators

Recently, leading edge vortex generators inspired by the protuberances of humpback whales' flippers have prompted several research studies, e.g., [34]–[36]. This leading edge modification has been show to trigger the formation of two counter rotating vortices between each protuberance that can potentially improve the stall performance of the airfoil [37]–[39].

Johari *et al.* tested several sinusoidal leading edge geometries in [40] on an airfoil at $Re = 1.83 \times 10^5$. The water tunnel tests showed an overall different stall behaviour for the modified airfoils. The protuberances degraded slightly the pre-stall performance but increased the lift coefficients after the critical stall angle of the baseline airfoil and displayed overall smoother lift curves. The results from this paper also show that the amplitude of the sine wave that defines the leading edge shape plays a bigger role in the airfoil's behaviour than the wavelength.

Guerreiro and Sousa also studied these sinusoidal leading edges in the wind tunnel at lower Reynolds numbers ($Re = 7.0 \times 10^4 - 1.4 \times 10^5$) and for different aspect ratios [38]. The authors reported similar improvements to the stall regime of the airfoils, especially at $Re = 7.0 \times 10^4$ and for the wing with the larger aspect ratio, in which the influence of the wingtip vortices was less significant. These results further reinforce the utility of this leading edge morphology to wings operating in the stall regime.

The numerical study by Câmara and Sousa [37] showed similar results using Detached Eddy Simulations (DES) and further elucidated the streamwise vortices structure. The results from the infinite wing simulations were similar between wingspans equal to one and two leading edge wavelengths; however, the authors described that at least two wavelengths were necessary to capture the apparently bi-periodic vortex structure.

Additionally, the capability of numerical RANS and DES approaches to accurately predict the effects of leading edge protuberances in finite wings was further evaluated by Esmaeili *et al.* [41] and compared with experimental measurements. In [41], the influence of the finite wing's aspect ratio was also measured, where the leading edge modification was reported to only have a substantial impact on the post-sall regime in the larger aspect ratio wing.

Leading edge protuberances vortex generators were also applied to horizontal axis wind turbines in a few numerical and experimental studies [42] [43] with mixed results, suggesting that the effects of this technology in HAWTs will vary significantly with the rotor design and operating conditions. The experimental results from [43] showed improvements for a small scale HAWT at low wind speeds. The experimental study by Zhang *et al.* [44] also indicated improved performance for thick airfoils typically used in the root of HAWT blades.

Concerning the application of this technology in VAWTs, a few numerical studies have been published. Wang and Zhuang [45] analysed the performance of leading edges protuberances (serrations) in a small two bladed H-Darrieus turbine, operating at $\lambda < 4$. The 3D unsteady RANS simulations, using the realizable $k - \epsilon$ turbulence model, showed a promising increase in power output (between 50% and 15%) throughout the whole tip speed ratio and wind speed range. This for the best leading edge geometry analysed: $\lambda_{vg} = 1/3c$; $A_{vg} = 0.025c$.

The subsequent numerical study by Wang *et al.* [46] described the optimisation of a three bladed VAWT with similar overall dimensions and solidity and the influence of twist angle (helical rotor) was also considered. For both the helical and straight blade rotor configurations, the best leading edge geometry was equivalent to the one proposed in [45], but with half of the wavelength (i.e., $\lambda_{vg} = 1/6c$; $A_{vg} = 0.025c$).

Another article, by Yan *et al.* [47], points to better performance, for a higher solidity VAWT, with a more conservative leading edge geometry: $\lambda_{vg} = 0.4c$; $A_{vg} = 0.01c$.

In the experimental VAWT research performed by Du [1], a wind tunnel comparison was also made

between a standard VAWT design and one fitted with leading edge protuberances. While the baseline turbine failed to self-start, the modified geometry was able to reach its maximum tip speed ratio in under 100 seconds, clearly showing the potential of this technology to also improve the starting behaviour of VAWTs.

Further possible improvements of a VAWT's efficiency under nominal operation through the use of leading edge protuberances have yet, to the author's knowledge, to be experimentally tested.

1.4   Thesis outline

This section outlines the subsequent structure of this document.

- In chapter 2, the parameters and constraints considered in the design process of the unmodified rotor are delineated and discussed, and a final baseline turbine configuration is established. In the last section, the design process used to define the modified leading edge geometry is presented.

- Chapter 3 describes the infinite blade parametric CFD study carried out to establish the leading edge geometry employed in the experimental study.

- The design, construction, and operation of the entire experimental setup is depicted in chapter 4. The calibration and validations of the instrumentation used is also described in this chapter.

- In chapter 5, the experimental results are presented and the performance of the leading edge protuberances is evaluated and compared with the baseline values.

- Chapter 6 portrays the half-turbine (finite blade) study, performed mainly to validate the numerical settings used to define the leading edge geometry in the parametric analysis. As such, the numerical results obtained are also compared with the experimental values in this chapter.

- Finally, in chapter 7, the main conclusions drawn from the numerical results and from the experimental study are outlined. A second section briefly discussing the possible focus of future works on the subject is also included.

2   Turbine design

2.1   Design considerations and final dimensions

The design and characteristics of the turbine model used in the experimental and numerical studies were mainly constrained by the wind tunnel's test area dimensions. Several non-dimensional performance parameters and design guidelines were also considered to ensure that the final turbine design is reasonably optimised and efficient, and that the results from this study are also applicable to the more common small and medium scale Darrieus wind turbine designs.

2.1.1   Number of blades

The power generated by a wind turbine depends mainly on the swept area:

$$A = H \times D, \tag{2.1}$$

not on the blade area. However the number of blades can strongly influence the efficiency and other factors that contribute to the overall performance of the turbine, e.g. self-starting behaviour [48].

One of the parameters that is heavily affected by the number of blades is solidity, σ, increasing the number of blades increases σ considerably (assuming D constant). However, Gosselin *et al.* [49] showed how the number of blades does not impact significantly the maximum C_P when σ is kept constant.

The number of blades, N, of Darrieus wind turbines typically ranges between two and five. Four and five-bladed designs were not considered since they do not show significant performance gains and add manufacturing complexity [50]. Two bladed designs have advantages in simplicity and in the structural design but suffer from large torque ripples throughout their rotation [49], [51], which reduces the longevity of the structural components. Poor self-starting capability is also common, two-bladed turbines are generally capable of self-starting, but not in all the possible starting positions. Comparatively, three-bladed designs are shown to be able to initiate rotation in almost all initial position (and with lower wind speeds [52]) and to produce a torque curve with significantly less amplitude.

As such, a three-bladed configuration was chosen for this study, also noting that it is probably the most common design in smaller commercial VAWTs.

2.1.2   Rotor aspect ratio

The rotor aspect ratio, defined as the ratio of turbine height to rotor diameter:

$$AR = H/D, \tag{2.2}$$

seems to moderately affect the turbine's efficiency and the λ at witch max power occurs (it should be noted that this ratio is also referred as *rotor shape factor* in some literature).

Brusca *et al.* [53] demonstrated how decreasing the AR increases the Re_c (defined in Eq. 2.5), and thus the turbine's overall efficiency, concluding that the rotor should have the smallest AR possible, ideally with values around $AR = 0.4$ or below.

Nevertheless, the majority of articles do not seem to suggest the same relationship and present an increase in efficiency for larger AR values, which also corresponds to the characteristics of most commercial available VAWTs. Li *et al.* [54] employed the panel method in a three dimensional analysis to investigate the effects of the aspect ratio and of the rotor solidity (σ) in the turbine's performance. The authors found that the increase in the blade's aspect ratio:

$$AR_b = \frac{H}{c}, \tag{2.3}$$

associated with the increase of AR (within the range of $AR = 0.4$ to 1.2), reduced the influence of the induced velocity generated by the tip vortices, which resulted in an increase of the maximum C_P. Fig. 2.1 (b) shows how there is almost no change in max C_P when the AR_b was kept constant.

(a) consign σ

Fig. 9 Fluctuation of power coefficient curve against the tip speed ratio λ in the case of the fixed
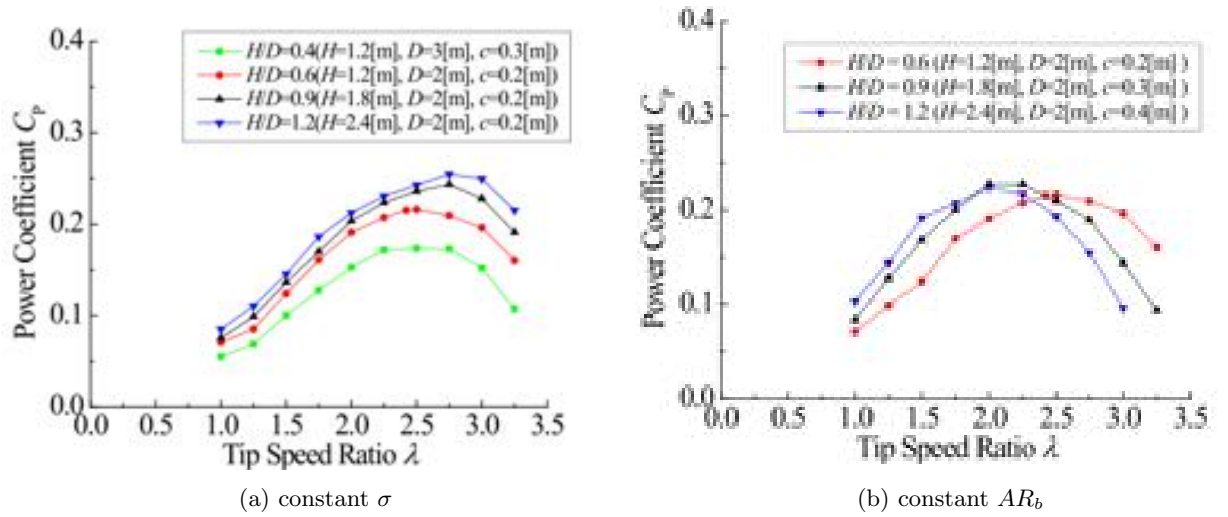
tions of power coefficient are compared with a fixed solidity in different rotor aspect ratios, ng on the tip speed ratio. The ratio of the diameter and blade span length are $H/D = 0.4$, 0.6 [54].

Roy *et al.* [55] also reported similar results and studied the sensitivity of the relation between the C_P curves and AR to different chord Reynolds number (Fig. 2.2), using a double multiple streamtube model. The authors concluded that an $AR = 1.0$ is a good compromise between good performance at lower and higher Reynolds numbers and that it provides suitable efficiency over a good range of λ.
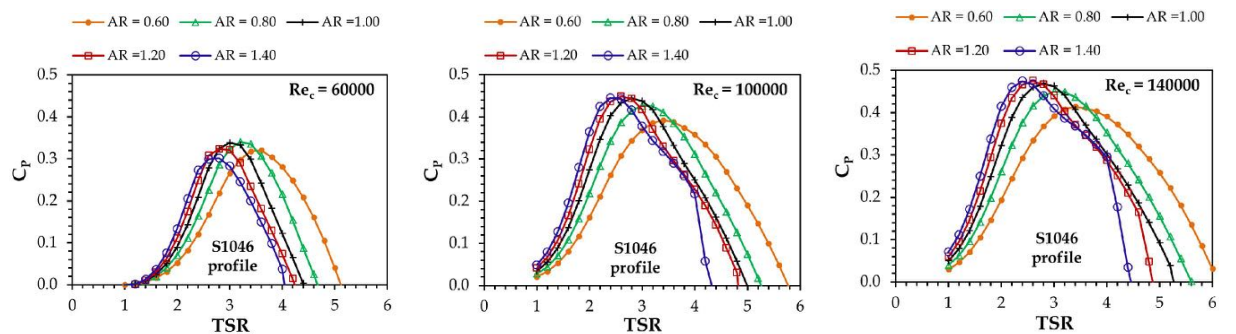
Figure 2.2: C_P curves for multiple rotor aspect ratios at three different Re_c, reproduced from Roy *et al.* [55].

12

From the results discussed above, and taking into account the wind tunnel's test area dimensions and

the manufacturability of the model, the aspect ratio of the turbine was set to $AR = 1.0$. The available literature (e.g., [50], [55]) shows no significant performance discrepancies for the values between $AR = 1.0$ to 1.2 and $AR = 1.0$ is a good compromise between a larger AR_b (for a significantly improved self-starting capability [20]) and a smaller solidity (further discussed below).

2.1.3 General dimensions

The main limiting factor of the overall dimensions of the rotor is the size of the test area on the wind tunnel—i.e., $1350 \times 800 \ mm^2$. The tests were performed in a open jet setup, with the model at least $1 \ m$ away from the end of the contraction section, to prevent noticeable blockage effects.

To further ensure that the wake was fully enclosed in the tunnel's cross-sectional area and that the jet's growing turbulent shear layers also didn't interact meaningfully with the turbine, it was stipulated that the turbine's rotor should have a maximum height of $H \leq 450 \ mm$ and that the diameter should also not exceed $D \leq 450 \ mm$ ($\frac{1350}{3}$). This equates to a rather high blockage ratio of around 19%. This is, however, considering the total swept area of the turbine (A), the actual frontal area of the blades is much smaller in any position. Calculated only with the blades' frontal area, the actual blockage ratio should be below 7%. van Bussel *et al.* reported no meaningful blockage effects with a blockage ratio of 14% and considered 43% a reasonable limit for a open jet wind tunnel.

Considering also the desired aspect ratio, $AR = 1.0$, the height, H, and the diameter, D, of the rotor were hence both set to $450 \ mm$.

2.1.4 Turbine solidity

The solidity, σ, is a non-dimensional parameters heavily related with the performance of any Darrieus turbine, defined in Eq. 1.13.

A variation in σ is typically linked to a change in the maximum C_P and larger values of solidity reduce the tip-speed-ratio (λ) at which maximum power occurs (Fig. 2.3).

Increasing σ can also be used to enhance the self-starting behaviour of a turbine, as larger values (in the range of $\sigma = 0.4$ to 0.6) increase the torque produced, which reduces the average start-up time [20]. In inconsistent wind speed scenarios, a better self-starting capability can make up for the slight reduction in max C_p of larger σ values, in terms of overall turbine efficiency.

Roy *et al.* [55] studied the effects of solidity in the C_P curves for a turbine with an aspect ratio of $AR = 1.0$ and the sensitivity of the results to the chord Reynolds number. The study showed the most efficient values to be around $\sigma = 0.2$. The effect of σ in the λ_{Cpmax} is also apparent.
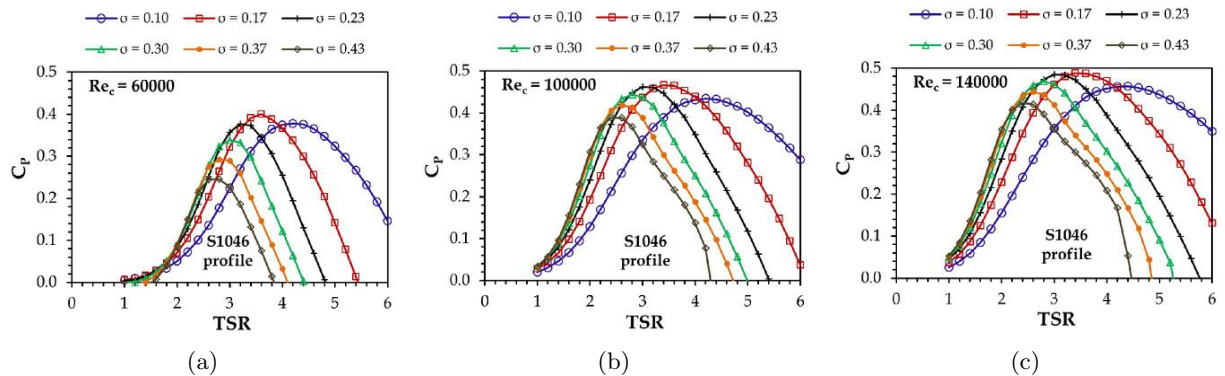
Figure 2.3: C_P curves for multiple rotor solidities at three different Re_c, reproduced from Roy *et al.* [55].

The numerical study performed by Sagharichi *et al.* [56] also showed similar results with peak efficiency at $\sigma = 0.3$.

Another important consideration is the minimum acceptable blade chord (c) dimension, taking in to account that reducing the chord also reduces the size and the resolution of the proposed leading edge modifications. An acceptable trade-off was found with $c = 75\ mm$ and $\sigma = 0.5$. This also places the AR_b at a value of 6, which is higher than the $AR_b = 5.7$ shown in the analysis by Worasinchai [57] to be required for self-start (although at low wind speed $U = 6\ m/s$).

For a turbine with similar solidity, $\sigma = 0.48$, Fiedler and Tullis [58] reported a maximum $C_P \approx 0.34$ (Fig. 2.4) (also using a symmetrical airfoil - NACA0015 and with $Re_c \approx 3.6 \times 10^5$) and McLaren [59] also obtained a max experimental $C_p \approx 0.36$, with the same turbine. On the other hand, for a higher solidity ($\sigma = 0.54$) Li $et\ al.$ [60] showed max C_P values of around 0.27, although with a wind speed of $7.7\ m/s$.
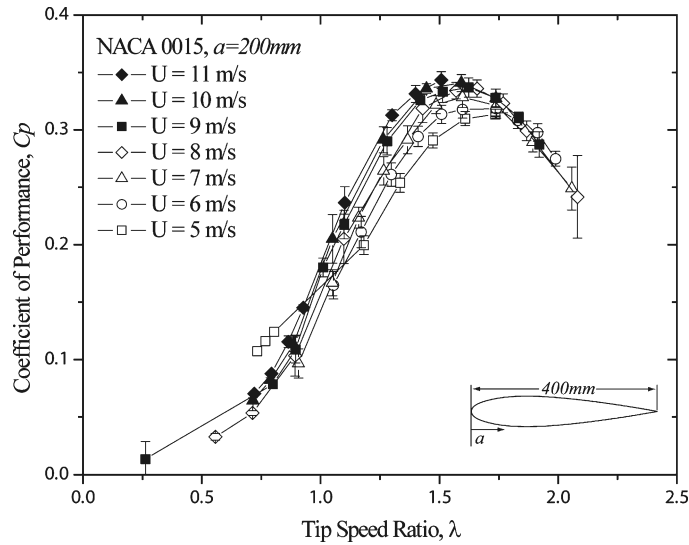
Figure 2.4: C_P curves for $\sigma = 0.48$, reproduced from [58].

This comes to show approximately the expected range of the turbine's C_P, considering also the similar performance of both NACA0015 and NACA0018 in the $Re_c \approx 1 \times 10^5$ range [55], even if other factors also influence the final performance. These results also shows that the maximum C_P could have been somewhat increased by adjusting the solidity to smaller values. However the design was too constrained by the wind tunnel dimensions and the minimum acceptable blade chord to allow any smaller σ values.

2.1.5 Reynolds number and tip-speed-ratio

For Darrieus turbines, the Reynolds number is based on the blade chord, and even though it can be defined using the apparent wind velocity, W:

$$Re_c = \frac{Wc}{\nu}, \tag{2.4}$$

the most common definition uses the tangential velocity component, $V = \Omega R$:

$$Re_c = \frac{\Omega R c}{\nu}. \tag{2.5}$$

Higher Reynolds numbers typically increase the power coefficient, as can be seen, for example, in [55]. The measurements by Sheldahl $et\ al.$ [61] showed that increasing Re_c has unsubstantial effects at lower tip-speeds but increases peak power and the Cp at higher λ (Fig.2.5). Data obtained by Bravo $et\ al.$ [62] seems to indicate values of approximately $Re_c = 4 \times 10^5$ to be the limit of this dependence. In fact,

Armstrong *et al.* [63] observed power values independent of the Reynolds number for $Re_c > 5 \times 10^5$.
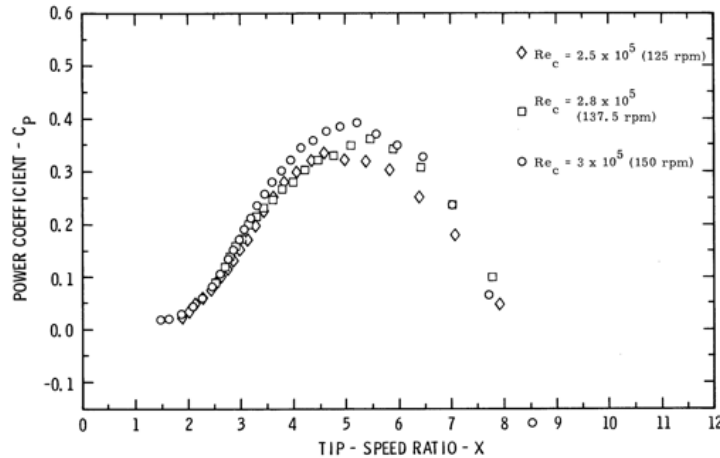
Figure 2.5: C_P curves for different Re_c (NACA0015), reproduced from [61].

The empirical correlation derived in [19] places the optimal tip-speed-ratio of the turbine at around $\lambda = 1.8$, which corresponds to $\Omega = 780\ rpm$ and $Re_c \approx 1 \times 10^5$.

According to Laneville and Vittecoq [10], the dynamic stall losses are present at tip-speed-ratios below five and are even more relevant at ($\lambda < 2.5$), establishing that the eventual beneficial effects of the proposed leading edge modifications will be visible in the turbine's performance.

2.1.6 Blade profile

Symmetrical NACA00xx profiles were common in the first studies of straight bladed Darrieus turbines—e.g., [14]–[16], [61]. More recently, cambered profiles with increased thickness have been proposed as better alternatives, although with limited gains ($< 5\%\ C_P$) [64]. Du *et al.* [1] demonstrated how a symmetrical profile (NACA0021) can achieve a comparable performance to a more complex profile specifically designed for VAWTs applications (DU06W200).

Additionally, symmetrical airfoils also have the advantage of being able to provide the same lift outputs either with positive or negative incidence angles.

As such, the NACA0018 was chosen, also considering it is on of the most widely adopted profiles in VAWTs designs.

2.1.7 Turbine final dimensions

The chosen final dimensions and characteristics of the baseline turbine are compiled in table 2.1.

2.2 Leading edge protuberances

As already mentioned in chapter 1, the geometry of leading edges protuberances is defined by a sinusoidal line with amplitude, A_{vg}, and wavelength, λ_{vg}, Fig. 2.6 (a). To create the protuberances, the profile is stretched or shortened to follow the sinusoidal line at the leading edge. This shape modification is only applied to the front section of the airfoil, in front of the maximum thickness point (at 30% of the chord for any four-digit NACA airfoil), Fig. 2.6 (b).

Table 2.1: Turbine final dimensions.

H-Darrieus rotor	
Number of blades - N	3
Height / blade span - H	0.45 m
Diameter - D	0.45 m
Chord - c	0.075 m
Airfoil	NACA0018
Swept area - A	0.203 m^2
Rotor aspect ratio - AR	1.0
Solidity - σ	0.5
Blade aspect ratio - AR_b	6.0

(a)   (b)
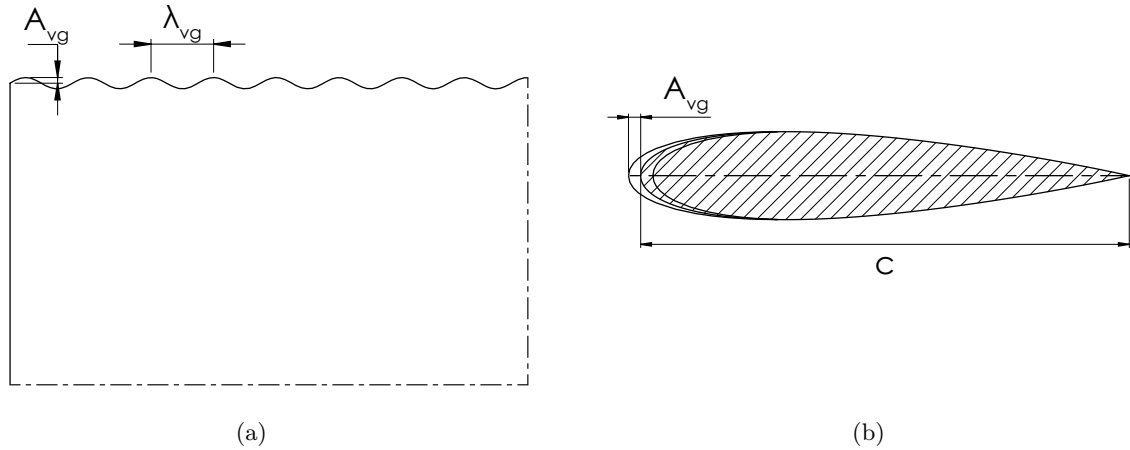
Figure 2.6: Sinusoidal leading edge parameters.

2.3   Design process

With the dimensions and parameters established in section 2.1, the aerodynamic design of the baseline unmodified turbine was essentially established.

To design the leading edge protuberances for the modified turbine, however, further analysis was required to ensure that the chosen configuration was reasonably optimised for these turbine dimensions and operating conditions.

To that end, a CFD study described in chapter 3 and 6 was performed with the commercial software STAR-CCM+ to define the modified leading edge design. This CFD analysis comprised multiple infinite blade and half-turbine (finite blade) turbine simulations, performed in parallel with the wind tunnel tests, following the general workflow described below and illustrated in Fig. 2.7.

1. An initial infinite blade simulation was adjusted to match the baseline turbine experimental results.

2. A parametric study of the leading edge geometry was then carried out, using the same infinite blade setup.

3. The leading edge configuration that presented the highest performance gain in the infinite blade analysis was then implemented in the finite blade domain, where half of the turbine was modelled

with the same numerical models and mesh dimensions. This way, the numerical results could be more realistically compared with the experimental values, in order to validate the turbulence model and other numerical settings used and, therefore, substantiate the leading edge configuration chosen with the parametric study.

4. If the half-turbine results did not reasonably match the experimentally measured performance of the modified turbine, the numerical models and the mesh parameters would be tuned until the estimated C_P was in agreement with the wind tunnel values and a final infinite blade parametric analysis could be performed.

After the half-turbine simulations were altered to better match the experimental results, the parametric study was revisited. Since the best leading edge geometry estimated in the first parametric study ended up being also the best configuration suggested by the final parametric analysis, only one set of modified blades had to be manufactured and tested in the wind tunnel.
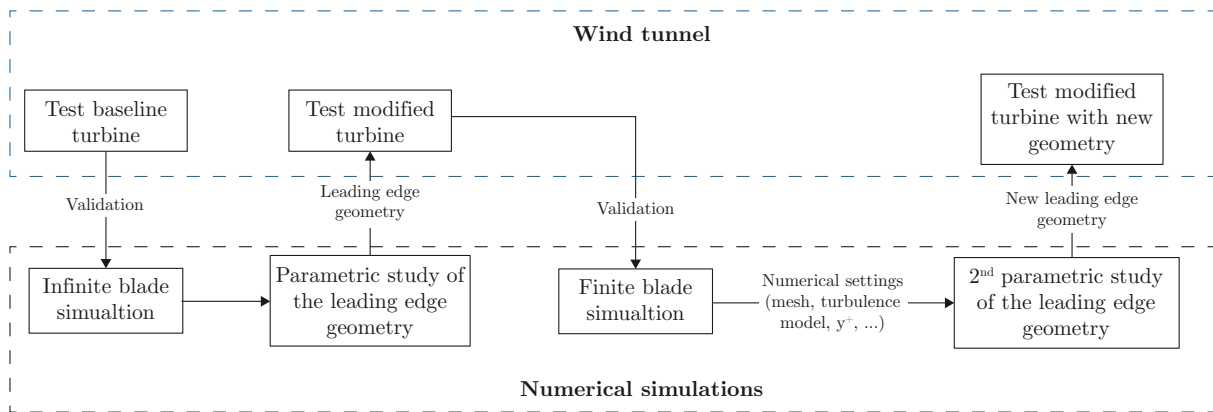
Figure 2.7: Leading edge geometry design process.

3 Infinite blade simulations

This chapter describes the infinite blade CFD study revised after the half-turbine simulations and used to define the final modified leading edge geometry

Ideally, the finite blade mesh delineated in chapter 6 would also have been used for this study, however, the half turbine simulations proved too costly for this purpose.

3.1 Problem definition

Rotational speed and free-stream velocity

All CFD calculations were performed at $U_\infty = 8 \ m/s$ and the turbine's rotational speed was chosen to replicate the maximum power output conditions, in this case $\Omega = 560 \ rpm$, which equates to the $\lambda_{Cp \ max} = 1.65$ observed in the wind tunnel tests of the baseline turbine (Fig. 5.11). The interest in this values was also to place the turbine in significant dynamic stall operational conditions.

Performance evaluation

The efficiency/performance of each simulated turbine geometry was evaluated and compared with the experimental results through the estimated power coefficient, C_P. This coefficient was calculated with Eq. (1.12), using the mean torque obtained from the pressure and viscous forces applied to the turbine's surfaces over one rotation.

3.2 Mathematical models and numerical methods

Even if the chord Reynolds number at this rotational speed, $Re_c = 6.6 \times 10^4$, did not place the blades' airfoils close to the transition point [65], turbulent flow is clearly expected, especially considering the dynamic stall effects.

Therefore, Reynolds Averaged Navier-Stokes (RANS) models were chosen to approximate the turbulence field, instead of computing directly the whole scales of turbulence through Direct Numerical Simulations (DNS) or even just the scales above a certain length using Large Eddy Simulations (LES), mainly due to the computational cost associated with the latter methods.

3.2.1 RANS

In all RANS models, turbulence is modelled by decomposing each fluctuating flow property in the Navier-Stokes equations, ϕ (e.g., velocity, U), in to a time averaged value, $\bar{\phi}$, and in to a fluctuating component, ϕ':

$$\phi = \bar{\phi} + \phi'. \tag{3.1}$$

The resulting Reynolds averaged Navier-Stokes equations are:

$$\frac{\partial (\rho U_i)}{\partial t} + \frac{\partial}{\partial x_j} (\rho U_i U_j) = -\frac{\partial P}{\partial x_i} + \frac{\partial}{\partial x_j} \left[\mu \left(\frac{\partial U_i}{\partial x_j} + \frac{\partial U_j}{\partial x_i} \right) - \rho \overline{u_i' u_j'} \right], \tag{3.2}$$

which are identical to the original equations, except for the additional Reynolds stress term, $-\rho \overline{u_i' u_j'}$. Different models are then used to close the RANS equations by modelling the Reynolds stress term from mean flow quantities ($\bar{U}_i$), instead of solving for the fluctuating components (U_i') directly.

3.2.2 Turbulence and transition models

Two turbulence models where considered, realizable $k - \epsilon$ and $k - \omega$ SST, both two-equation models. The realizable variant of the $k - \epsilon$ model has been shown to provide good predictions in flows with complex recirculating and separation regions, and has successfully been applied to similar leading edge protuberances problems, by Wang et al. [45] and [46], for example. Nevertheless, other authors also reported good results with $k - \omega$ in simulations where the same leading edge modification was applied to VAWTs and HAWTs [42], [47], [66].

Additionally, given the Reynolds number expected in these conditions ($Re_c = 6.6 \times 10^4$), the $k - \omega$ SST with the $\gamma - Re_{\theta_t}$ transition model was also considered in this application.

In both models, and all other eddy viscosity models, the transfer of momentum, which follows the direction of the velocity gradient, is assumed to be proportional to the turbulence strength. Therefore, the Reynolds stress can be assumed to be proportional to the velocity gradient:

$$- \rho \overline{u'v'} = \mu_t \frac{\partial U}{\partial y}, \tag{3.3}$$

where the constant of proportionality, μ_t, is called turbulent (eddy) viscosity, an artificial concept that essentially dictates the intensity of the turbulent diffusion.

This assumption can be extended into three dimensional coordinates by:

$$- \rho \overline{u_i' u_j'} = \tau_{ij} = \mu_t \left(\frac{\partial U_i}{\partial x_j} + \frac{\partial U_j}{\partial x_i} - \frac{1}{3} \frac{\partial U_k}{\partial x_k} \delta_{ij} \right) - \frac{2}{3} \rho k \delta_{ij}, \text{ where } \delta_{ij} = \begin{cases} 1 & i = j \\ 0 & i \neq j \end{cases}, \tag{3.4}$$

and in this from, serve as a basis for all eddy viscosity models.

Even though each model then calculates μ_t differently, Eq. (3.4) is always used to obtain $-\rho \overline{u'v'}$ and subsequently close the RANS equations.

Realizable $k - \epsilon$

In essence, in the standard $k - \epsilon$, two additional transport equations are solved to calculate k and ϵ [67]:

$$\frac{\partial (\rho k)}{\partial t} + \frac{\partial (\rho u_j k)}{\partial x_j} = \tau_{ij} \frac{\partial u_i}{\partial x_j} - \rho \epsilon + \frac{\partial}{\partial x_j} \left[\left(\mu + \frac{\mu_t}{\sigma_k} \right) \frac{\partial k}{\partial x_j} \right] + \rho L_k \tag{3.5}$$

$$\frac{\partial (\rho \epsilon)}{\partial t} + \frac{\partial (\rho u_j \epsilon)}{\partial x_j} = C_{\epsilon 1} f_1 \frac{\epsilon}{k} \tau_{ij} \frac{\partial u_i}{\partial x_j} - C_{\epsilon 2} f_2 \frac{\rho \epsilon^2}{k} + \frac{\partial}{\partial x_j} \left[\left(\mu + \frac{\mu_t}{\sigma_\epsilon} \right) \frac{\partial \epsilon}{\partial x_j} \right] + \rho L_\epsilon \tag{3.6}$$

and Eq. (3.7) is used to compute the turbulent viscosity, μ_t.

$$\mu_t = C_\mu f_\mu \frac{\rho k^2}{\epsilon}, \ C_\mu = 0.09. \tag{3.7}$$

The specific model used in this analysis also uses a two layer approach, so that it can also be applied in finer meshes that resolve the buffer layer and the viscous sub-layer ($y^+ < 30$) [68]. In STAR-CCM+ this two layer formulation works either at meshes with $y^+ \sim 1$ or in meshes with $y^+ > 30$ (through wall-functions) [69].

In this study, the realizable variant of the model was also used, as it is shown to provide better performance in flows involving rotation, separation and boundary layers under strong adverse pressure gradients than the standard formulation. In summary, this variant of the model contains a new transport equation for ϵ and a variable damping function is applied to the coefficient C_μ [70].

$k - \omega$ SST

The original $k - \omega$ was developed as an improvement of the standard $k - \epsilon$ model, particularly to address the already mentioned unreliability in the near-wall behaviour, for example in boundary layers with adverse pressure gradients [71].

In this model, transport equations similar to Eq. (3.5) and (3.6) are solved with different coefficients to determine k and ω instead of k and ϵ, where ω is the specific turbulence dissipation, given by:

$$\omega = \frac{\epsilon}{C_\mu k}. \tag{3.8}$$

The main advantage is the absence of the empirical damping functions used by the $k - \epsilon$ model in the viscous sub-layer, this way the $k - \omega$ model is able to produce more accurate results in the presence of adverse pressure gradients.

On the other hand, the results of this model also present a large dependence on the free-stream turbulence conditions.

Since the $k - \epsilon$ model is not as susceptible to the inlet turbulence conditions, the solution to this dependence is the Shear Stress Transport (SST) $k - \omega$ developed by Menter [72], where, among other minor changes, both models are blended and the $k - \omega$ is only used in the near-wall regions.

The transport equations are thus similar to the ones from the standard $k - \omega$ model:

$$\frac{\partial(\rho k)}{\partial t} + \frac{\partial(\rho u_j k)}{\partial x_j} = \tau_{ij} \frac{\partial u_i}{\partial x_j} - \beta^* \rho \omega k + \frac{\partial}{\partial x_j} \left[(\mu + \sigma_k \mu_t) \frac{\partial k}{\partial x_j} \right] \tag{3.9}$$

$$\frac{\partial(\rho \omega)}{\partial t} + \frac{\partial(\rho u_j \omega)}{\partial x_j} = \frac{\gamma}{\nu_t} \tau_{ij} \frac{\partial u_i}{\partial x_j} - \beta \rho \omega^2 + \frac{\partial}{\partial x_j} \left[(\mu + \sigma_\omega \mu_t) \frac{\partial \omega}{\partial x_j} \right] + 2(1 - F_1) \frac{\rho \sigma_{\omega 2}}{\omega} \frac{\partial k}{\partial x_j} \frac{\partial \omega}{\partial x_j}, \tag{3.10}$$

with the exception of the last term on the right in Eq. (3.10), which differentiates between the $k - \epsilon$ model and the standard $k - \omega$ model, hence function F_1 is used to blend between the two models by enabling or disabling this additional term. This blending function is defined based on the distance to the closest wall, so that $F_1 = 1$ in the near-wall region and the $k - \omega$ model is used, like shown in Fig. 3.1.
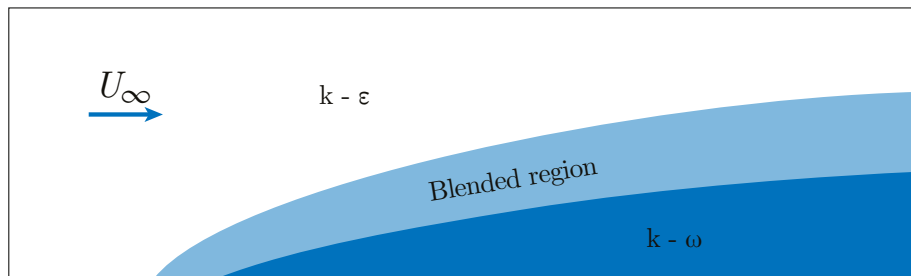

Figure 3.1: $k - \omega$ SST non-slip wall modelling.

$\gamma - Re_{\theta_t}$ transition model

This transition model is coupled to the $k - \omega$ SST turbulence model when a significant portion of the boundary layer is expected to be laminar ($Re \sim 1 \times 10^5$).

An additional transport equation (Eq. 3.11) is solved to obtain the turbulence intermittency, γ, which will then trigger the boundary layer transition, and a fourth transport equation (Eq. 3.12) is used to calculate the local momentum thickness Reynolds number, Re_θ, used to predict the transition point.

$$\frac{\partial(\rho\gamma)}{\partial t} + \frac{\partial\left(\rho u_j \gamma\right)}{\partial x_j} = P_\gamma - E_\gamma + \frac{\partial}{\partial x_j}\left[\left(\mu + \frac{\mu_t}{\sigma_f}\right)\frac{\partial\gamma}{\partial x_j}\right] \tag{3.11}$$

$$\frac{\partial\left(\rho\hat{R}e_{\theta t}\right)}{\partial t} + \frac{\partial\left(\rho u_j \hat{R}e_{\theta t}\right)}{\partial x_j} = P_{\theta t} + \frac{\partial}{\partial x_j}\left[\sigma_{\theta t}\left(\mu + \mu_t\right)\frac{\partial\hat{R}e_{\theta t}}{\partial x_j}\right] \tag{3.12}$$

The results obtained with both turbulence models were compared with the experimental measurements in the half-turbine study (chapter 6). Nevertheless, the realizable $k - \epsilon$ turbulence model with a $y^+ \sim 1$ in the blades' surfaces was used as a starting point in this parametric study, based on the baseline results displayed in table 3.1. Even though the infinite blade configuration is expected to slightly over-predict the turbine's performance, given the lack of tip vortices and other three-dimensional effects, the C_P value obtained with the $k - \omega$ SST is lower than the experimental value.

Table 3.1: Comparison of C_P values obtained with both turbulence models.

Geometry	Turbulence model	y^+	C_P
Baseline	Realizable $k - \epsilon$	~ 1	0.206
Baseline	$k - \omega$ SST	~ 1	0.122
Experimental			0.126

This option of turbulence model and wall distance was also later supported by the turbulence model validation made in the half-turbine study (see chapter 6).

3.3 Mesh

The structured trimmed meshes used in this analysis were based in the ones described by Wang et al. [45], [46], given the similarities of the analysed problems.

3.3.1 Domain and boundary conditions

The parameters of the computational domain were also similar to those used in [46], except for the vertical dimension, that varied between each simulation, as it was set to be equal to two wavelengths of leading edge geometry. This way, the eventual bi-periodic structure over the leading edge protuberances, reported in [37] and [47], could be captured, even if Câmara and Sousa [37] also reported similar aerodynamic forces when only one wavelength was modelled.

To simulate the rotational physics of the turbine, a sliding mesh was employed. As such, the domain was split into a stationary and rotating volume (Fig. 3.2 and 3.3), interacting through two interfacing surfaces.

In the inlet region of the stationary domain, a velocity inlet boundary condition was used, with $U = 8 \ m/s$. The turbulence intensity (TI) in the inlet was set at 1.0 %, between the values measured in the wind tunnel (~ 0.3 %) and the typically higher TI observed in real-world wind conditions [73].

The outlet region was established with constant atmospheric pressure. All other external regions, including the top and bottom planes, were defined with symmetric boundary conditions, in order to approximate the behaviour of infinite blades with no tip vortices.

Periodic boundary conditions were also tested in this span-wise directions but provided the same results as the equivalent symmetry planes. Most likely, due to the fact that these boundaries were aligned with the protuberance's peaks as to not bisect the vortex structure produced by the leading edge (see Fig. 3.9 (b), for example).
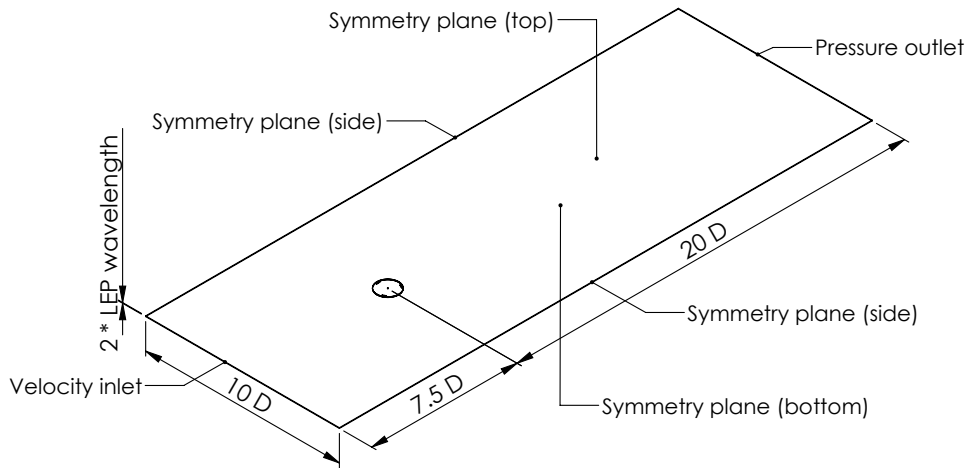
Figure 3.2: Stationary volume.
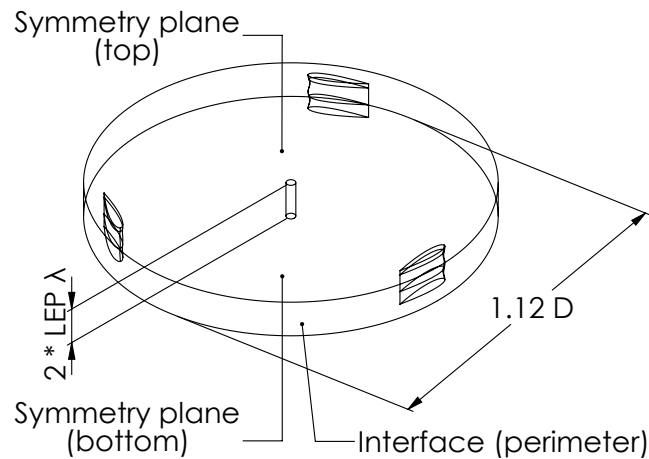
Figure 3.3: Rotating volume.

3.3.2 Mesh settings

The mesh refinement in all regions was defined in function of the cell resolution on the blade's surfaces (Fig. 3.4 (a)). With the trimmed mesh used, the cell size was progressively doubled from the refined section around the blade surfaces to the free-stream region, where the elements were 128 times larger. Apart from the blades, the other turbine surfaces had elements 4 times larger.

The prism layers used over all rotor surfaces were defined both by the y^+ requirements and to provide a smooth transition between the first cell height and the mesh size connected to the last layer.

Prism layers were also used in the interfacing mesh regions, to smooth out the interaction between the rotating and stationary cells (Fig. 3.4 (a)).
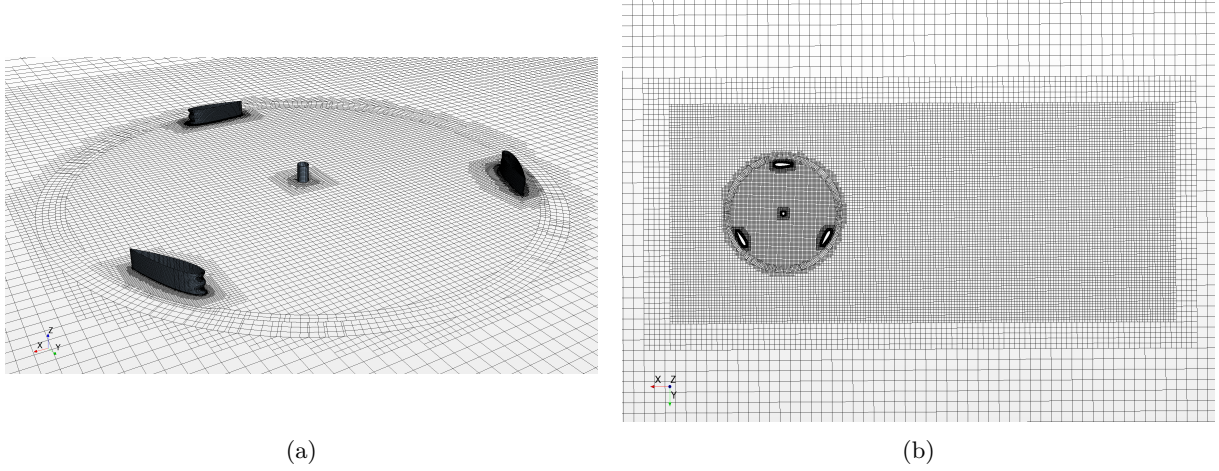
Figure 3.4: Mesh over rotor surfaces (a), Wake and rotating volume mesh refinement (b).

Figure 3.4 (b) shows the refined region placed around the rotor and the initial wake section.

3.3.3 Mesh resolution sensitivity analysis

To determine the final mesh resolution, the whole domain was incrementally refined until the C_P values showed an acceptable convergence. In this case, the leading edge geometry used was: $\lambda_{vg} = 1/6c$; $A_{vg} = 0.015c$.

Table 3.2: Mesh resolution sensitivity analysis.

Number of elements	Blade surface resolution [mm]	C_P
7.5×10^4	1.5	0.174
1.8×10^5	1.0	0.190
3.1×10^5	0.75	0.190
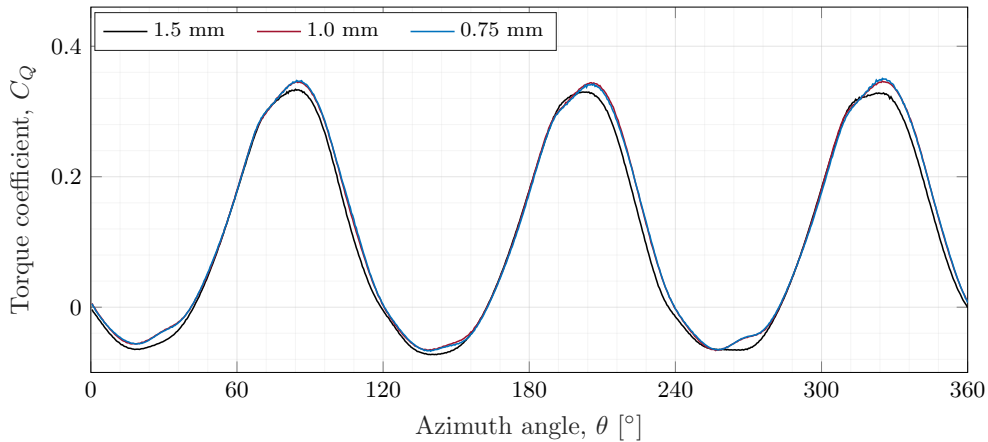
Figure 3.5: C_Q sensitivity to mesh resolution.

From the performance values shown in table 3.5 and the torque curves in Fig. 3.5, both grids equivalent to a blade surface resolution $\leq 1.0\ mm$ were considered suitable for this analysis. However, from this

point on, a blade surface resolution of 0.75 mm was used; not only because the added computational cost was not significant, but also to maintain a stronger consistency with the mesh used in the half-turbine study.

3.3.4 Blade span

The torque coefficient curves (Fig. 3.6) also didn't indicate any discrepancies in the performance predictions between the simulations performed with a blade span equivalent to two and four leading edge wavelengths. In this instance, a geometry with a smaller wavelength was used ($\lambda_{vg} = 1/8c$; $A_{vg} = 0.015c$) to reduce the computational cost of this sensitivity analysis.
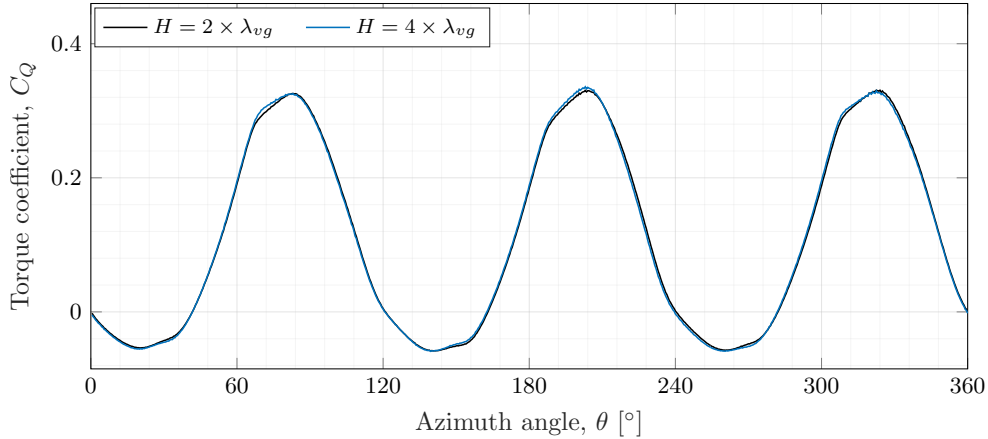
Figure 3.6: C_Q sensitivity to modelled blade span.

3.4 Solver settings and simulation process

A segregated flow solver based on the SIMPLE algorithm [69] was used to solve the mass and momentum conservation equations and a second order upwind space discretisation scheme was employed to compute the convection moment equation.

Given the dependent nature of the problem, a second order implicit unsteady solver was used to control the time discretisation. The time-step was set to the time interval equivalent to an azimuthal increment of $\Delta\theta = 0.5°$, as suggested in [74].

Each simulation was ran until the torque curve stabilised between two consecutive turbine rotations. After the first simulation, to reduce the number of rotations necessary to achieve a converged result, the fields of the previous run were used as initial conditions on the next one.

Table 3.3 summarises all mesh, domain, and solver settings used.

3.5 Leading edge geometry - parametric study

In order to find a suitable leading edge configuration for the optimised turbine rotor, the estimated power coefficients of multiple combinations of different leading edge amplitudes and wavelengths were compared.

Since the amplitude of the sinusoidal line that defines the leading edge protuberances was reported in [40], [45], [47] to have a more significant impact on the wing/blade's behaviour than the corresponding wavelength, the first set of simulations was performed with a constant wavelength of $\lambda_{vg} = 1/6c$ and with amplitudes ranging from 3.5% to 0.8% of the chord.

Table 3.3: Numerical settings used in the infinite blade simulations.

Models and solver settings		Mesh and domain settings	
Software	STAR-CMM+	Number of elements	3.1×10^5
Turbulence model	two-layer realizable $k - \epsilon$		
Solvers		Boundary conditions	
Flow solver	segregated	Inlet	velocity inlet $U_\infty = 8 \ m/s$, $TI = 1\%$
Pressure-velocity coupling	SIMPLE	Outlet	atmospheric pressure outlet
Convection space discretisation	2nd order upwind	Side, top and bottom	symmetry condition
Time discretisation	2nd order implicit unsteady	Moving mesh type	sliding mesh
Time-step	$1.488 \times 10^{-4} \ s$	Minimum cell size	$0.75 \ mm$
Inner steps	20	y^+ on blade surfaces	~ 1

3.5.1 Amplitude

The power coefficients of the fixed wavelength analysis, table 3.4, indicate a clear progression towards the smaller amplitude leading edge geometries, showing significant performance deterioration for $A_{vg} = 1.5\%c - 3.5\%c$ and a slight 4% C_P improvement over the baseline for the configuration with $A_{vg} = 0.8\%c$.

Table 3.4: Leading edge amplitude, A_{vg}, C_P comparison.

Geometry	C_P
Baseline	0.206
$\lambda_{vg} = 1/6c$; $A_{vg} = 0.008c$	0.214
$\lambda_{vg} = 1/6c$; $A_{vg} = 0.015c$	0.190
$\lambda_{vg} = 1/6c$; $A_{vg} = 0.025c$	0.146
$\lambda_{vg} = 1/6c$; $A_{vg} = 0.035c$	0.104

The torque coefficient comparison in figure 3.7 further corroborates this behaviour, displaying a constant decrease in C_Q throughout all rotor positions for the $A_{vg} = 2.5\%c$ and $A_{vg} = 3.5\%c$ geometries. A possible explanation relies in the increased drag in all three blades or mainly on the two blades that do not contribute to the torque generation in each rotor position. The leading edge with $A_{vg} = 1.5\%c$ seems to provide slightly improved torque peaks over the baseline curve accompanied, however, by a worse performance in the negative torque regions. The protuberances with an amplitude of $A_{vg} = 0.8\%c$ show similar improvements in the torque peaks but also in the negative torque troughs.

As a result, in the following wavelength analysis, the calculations were carried out with a fixed amplitude of $A_{vg} = 0.8\%c$. A second fixed amplitude analysis was also made with $A_{vg} = 1.5\%c$ to ensure that the poor results of the larger amplitude geometries shown in the amplitude study were not a consequence of the chosen wavelength ($\lambda_{vg} = 1/6c$).

3.5.2 Wavelength

Again, as reported by several authors in similar studies (e.g., [40], [47]), the variation of the leading edge wavelength had a less significant impact on the power and torque coefficients predicted.

The C_P values for the fixed 0.8%c amplitude, displayed on the left in table 3.5, also suggest the best geometry to be $\lambda_{vg} = 1/6c$; $A_{vg} = 0.008c$, with marginal performance losses with higher and lower
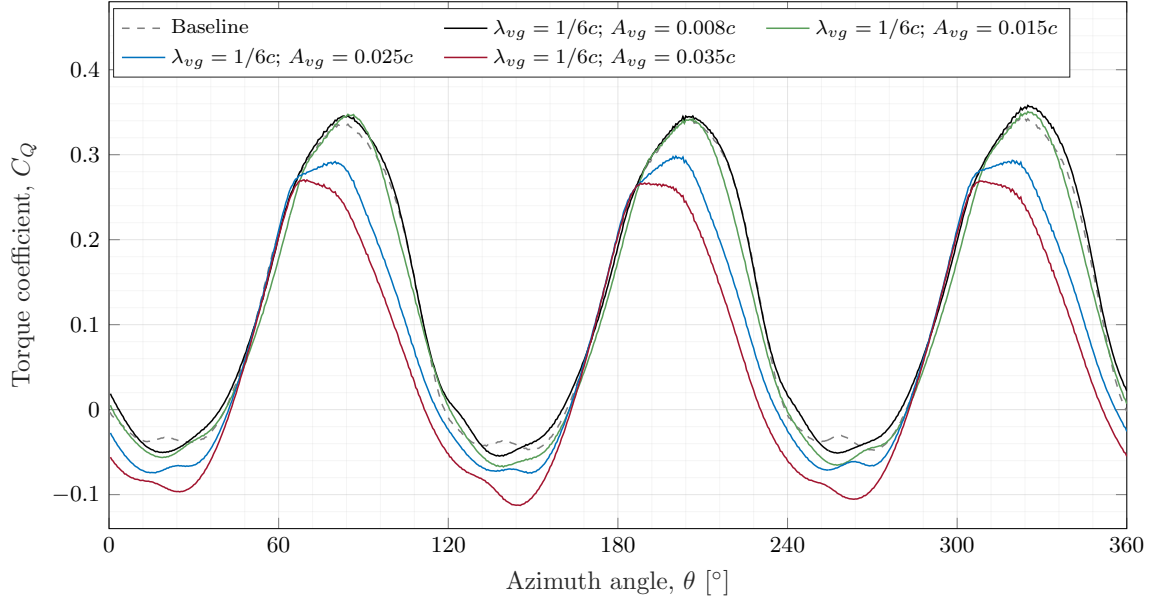
Figure 3.7: C_Q comparison with different leading edge amplitudes, A_{vg}.

wavelength values.

On the other hand, the analysis with the constant $A_{vg} = 1.5\%c$ value shows overall lower power coefficients converging towards the baseline value. Since in this case the leading edge protuberances did not improve the predicted performance, this behaviour naturally issues from the fact that, with the incremental increase in wavelength, the leading edge geometry becomes more conservative and closer to the baseline blade shape.

Table 3.5: Leading edge wavelength, λ_{vg}, C_P comparison.

Geometry	C_P	Geometry	C_P
$\lambda_{vg} = 1/10c$; $A_{vg} = 0.008c$	0.205	$\lambda_{vg} = 1/8c$; $A_{vg} = 0.015c$	0.184
$\lambda_{vg} = 1/8c$; $A_{vg} = 0.008c$	0.212	$\lambda_{vg} = 1/6c$; $A_{vg} = 0.015c$	0.190
$\lambda_{vg} = 1/6c$; $A_{vg} = 0.008c$	0.214	$\lambda_{vg} = 1/3c$; $A_{vg} = 0.015c$	0.199
$\lambda_{vg} = 1/3c$; $_{vg}A = 0.008c$	0.209	$\lambda_{vg} = 1/2c$; $A_{vg} = 0.015c$	0.203
Baseline	0.206		

Figure 3.8 also substantiates the diminished influence of the leading edge wavelength, especially when compared with the variation shown in the constant wavelength analysis (Fig. 3.7). The only discernible behaviour in this torque curve comparison is between all the modified blades and the baseline; all four modified geometries exhibit higher torque peaks and smoother troughs, albeit with increased minimum (negative) torque values.

Ultimately, the geometry with a wavelength of $c/6$ and a amplitude equal to 0.8% of the chord, $\boldsymbol{\lambda_{vg} = 1/6c}$; $\boldsymbol{A_{vg} = 0.008c}$, was chosen to be tested experimentally in the modified turbine.

The amplitude of the selected sinusoidal leading edge is significantly more conservative that the values chosen in other studies, for example $\lambda_{vg} = 1/3c$; $A_{vg} = 0.025c$ in [45] and $\lambda_{vg} = 1/6c$; $_{vg} = 0.025c$ in [46], but closer to the value selected in [47]: $A_{vg} = 0.01c$.

Most likely, the relatively small diameter and lower chord Reynolds number favour leading edges with less amplitude. This because, as mentioned in 1.2.3, this turbine operates at higher rotational speeds than
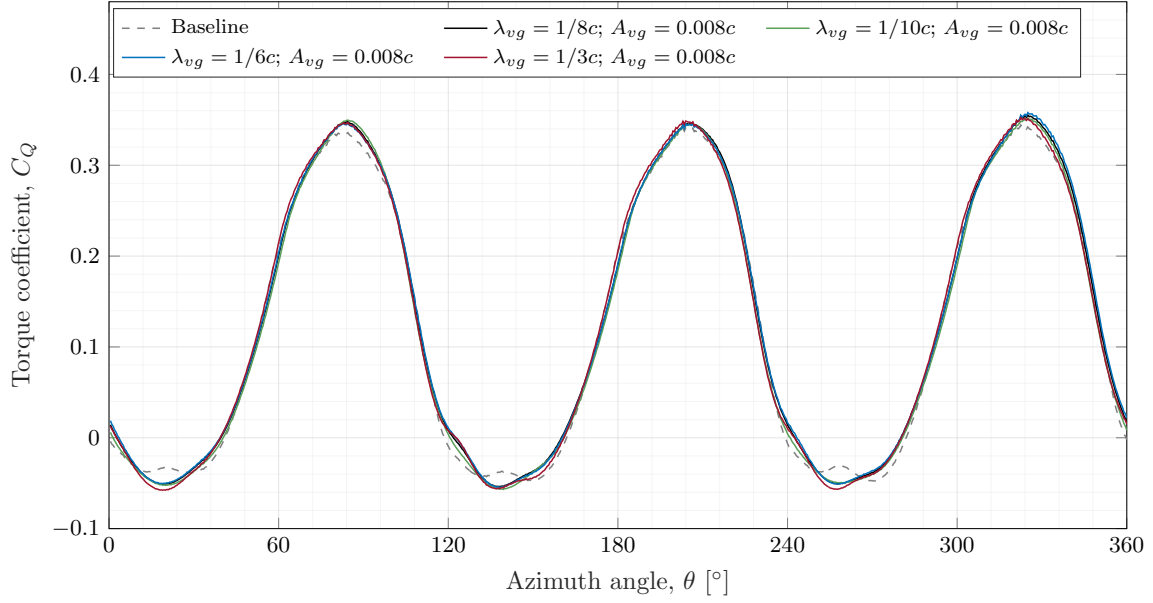
Figure 3.8: C_Q comparison with different leading edge wavelength, λ_{vg}.

an equivalent larger diameter VAWT to achieve the same tip speed ratios, which increases the rate of the flow incidence oscillations. Higher frequencies might not allow enough time for the complete development of larger vortex structures generated by more significant leading edge geometries.

3.6 Flow structure comparison

The counter-rotating vortex structures that travel downstream along the suction side of the blades can be observed by plotting the vectors of the velocity tangential to plane perpendicular to the chord line (see Fig. 3.9 (b)). In comparison, the same tangent velocity was also plotted in the baseline blade (Fig. 3.9 (a)), which naturally shows no circular flow in the same region.

(a) Baseline

(b) $\lambda_{vg} = 1/6c$; $A_{vg} = 0.008c$
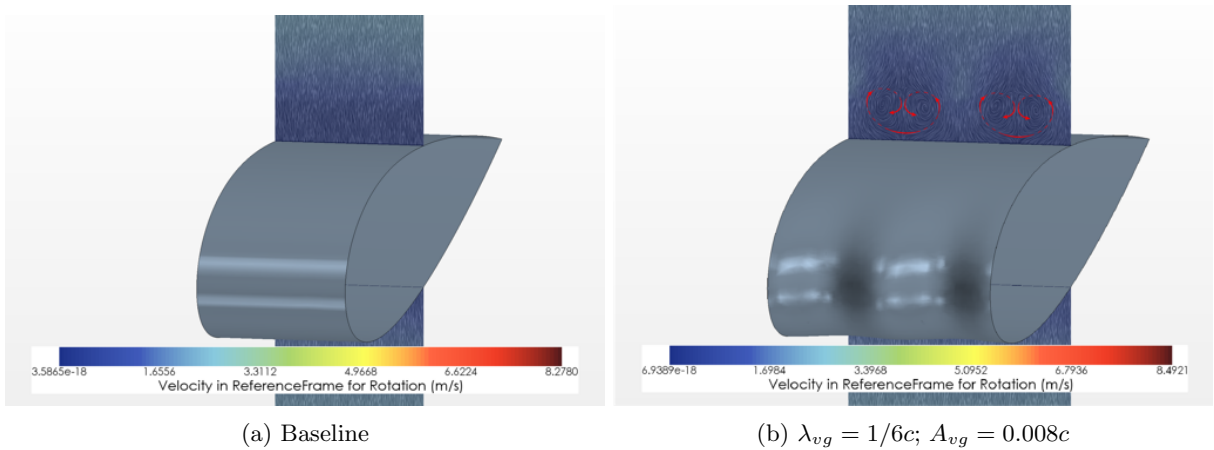
Figure 3.9: Vortex structures over suction side of modified blade at $\theta = 90°$.

3.7 Rotor wake comparison

The velocity contours in Fig. 3.10 were plotted to examine the influence of the chosen leading edge geometry on the wake produced by the rotor. These contours display the flow velocity in the plane perpendicular to the span-wise direction that bisects the domain in half.

This wake comparison does not show significant differences between the two configurations; however, the wake produced by the modified blades, Fig. 3.10 (b), seems to be slightly longer and narrower than its baseline counterpart, Fig. 3.10 (a) .
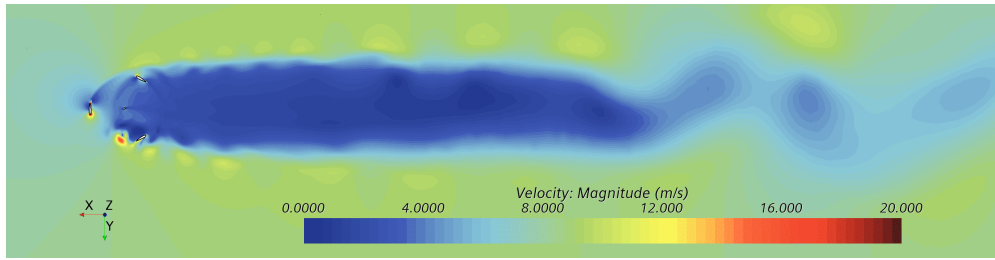
(a) Baseline
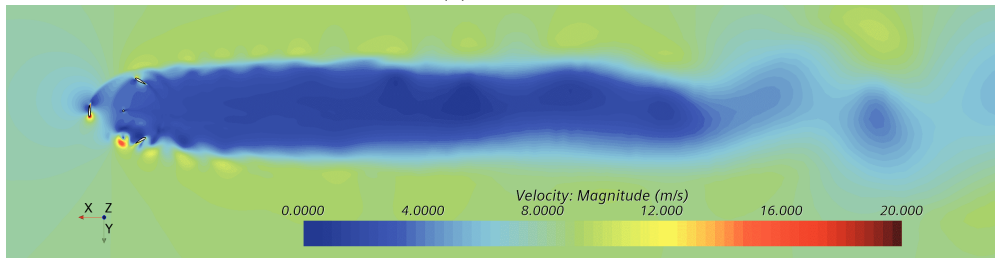
(b) $\lambda_{vg} = 1/6c$; $A_{vg} = 0.008c$

Figure 3.10: Rotor wake - velocity.

Nevertheless, the leading edge protuberances showed more noticeable effects on the intensity of the vortices shed by the blades in the upwind region (see also Fig. 1.9). Figure 3.11 juxtaposes the turbulent kinetic energy contours (plotted on the same plane) from the baseline and modified turbine simulations.

By comparing the shed vortex structure (located below the rotor shaft) between Figure 3.11 (a) and (b), the reduction in intensity, presumably caused by the leading edge protuberances, can be observed.
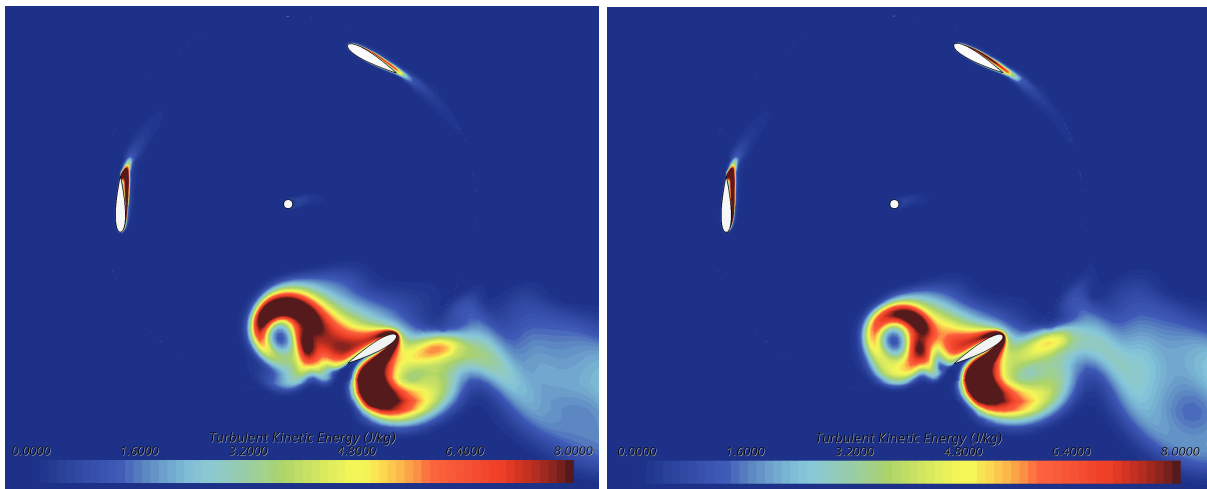
(a) Baseline

(b) $\lambda_{vg} = 1/6c$; $A_{vg} = 0.008c$

Figure 3.11: Rotor wake - turbulent kinetic energy.

4 Experimental setup

This experimental study was performed in the low-speed wind tunnel (LSWT) of the Mechanical Engineering Department at Instituto Superior Técnico (Fig. 4.1). The LSWT is a open-return wind tunnel with a maximum air speed of 10 m/s and a test section with a rectangular cross-sectional area of 800 mm (height) $\times$ 1350 mm (width), and was used in a open-jet configuration to measure the wind turbine's performance. A schematic drawing of the tunnel and of the turbine placement is shown below, where the turbine assembly was bolted to the base of the balance that is normally used with the wind tunnel.
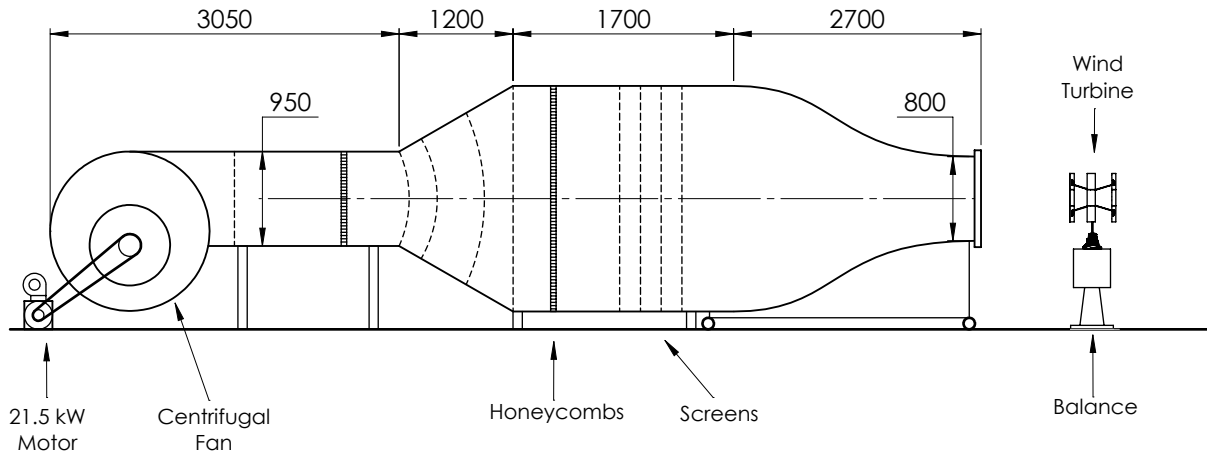
Figure 4.1: LSWT characteristics [mm].

Apart from the rotor dimensions stipulated in 2.1, some other design constraints and objectives were established before the design and manufacturing process of the whole experimental setup:

- Relatively inexpensive materials, components and manufacturing process (e.g., FDM 3D printing) should be used throughout the whole setup, without however meaningful structural or performance compromises. This to ensure and overall low cost of the entire system (around 200€).

- A suitable blade surface finish had to be assured, especially considering the eventual layer lines from the 3D printing process.

- Minimise rotor bearing friction, seeing how it would not be registered by the torque measuring components.

- The whole turbine structure has to be able to operate and withstand the high rotational speeds expected, and the resulting centrifugal loads, in order to cover the predicted tip speed ratio spectrum. This process is also aided by minimising the mass of each blade.

- The shaft and blade supports should be as slender as possible, so not to disturb the downstream

flow too much. Ideally, the rotor shaft would only be supported at one end, provided that excessive rotor oscillations do not occur.

- The measurement apparatus should be designed to provide acceptable precision and accuracy in the rotational speed and torque measurements.

4.1 Turbine assembly

The turbine, Fig. 4.2, can be split up int to two sub-assemblies: the rotor, which comprises the shaft, blade supports and the blades themselves; and the base, which houses the bearings that support the rotor and all the electronic and measuring components.

Figure 4.2: Turbine assembly.

4.1.1 Rotor

Blades

The blades were printed in a standard Fused Deposition Modelling (FDM) 3D printer in PETG plastic, with a layer height of 0.12 mm. The print direction was set to be along the spanwise axis so that there was no need to use printing support structures, which would worsen the surface finish of the parts.

This printing direction, however, coupled with the relative slenderness of the blades, required each blade to be printed in three separate sections. In the 3D printer that was used, the y-axis movement is accomplished by moving the printing bed, so while printing a slender part with a small contact area at the base, the top of the part would move slightly in relation to the printing head, due to the accelerations of the bed. As a result, above a certain height, the surface quality would deteriorate as the part height increased.

Each blade section, with a height of 150 mm, was printed with a 0.8 mm wall and with an internal rib structure (as seen in Fig. 4.3) to increase both the strength and the rigidity of each part.
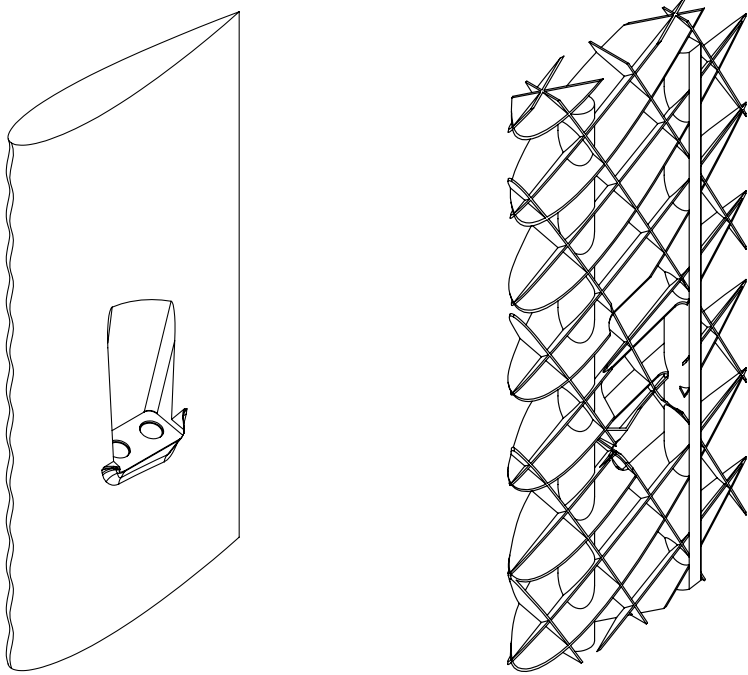
Figure 4.3: Blade section and internal rib structure.

To connect the three sections together and form each blade, two hollow circular aluminium profiles with an outer diameter of 6 mm were used (Fig. 4.4). The two profiles run along almost the entire span of each blade and serve as spars, to increase the strength and to distribute the centrifugal loads between the two anchor points of the supports and the whole blade.

Figure 4.4: Blade assembly.

The aluminium spars and the three blade sections were glued with epoxy, before the whole blade

surface was repeatedly sanded and sprayed with filler primer until the surface was reasonably smooth, Fig. 4.5 and Fig. 4.6 (b).
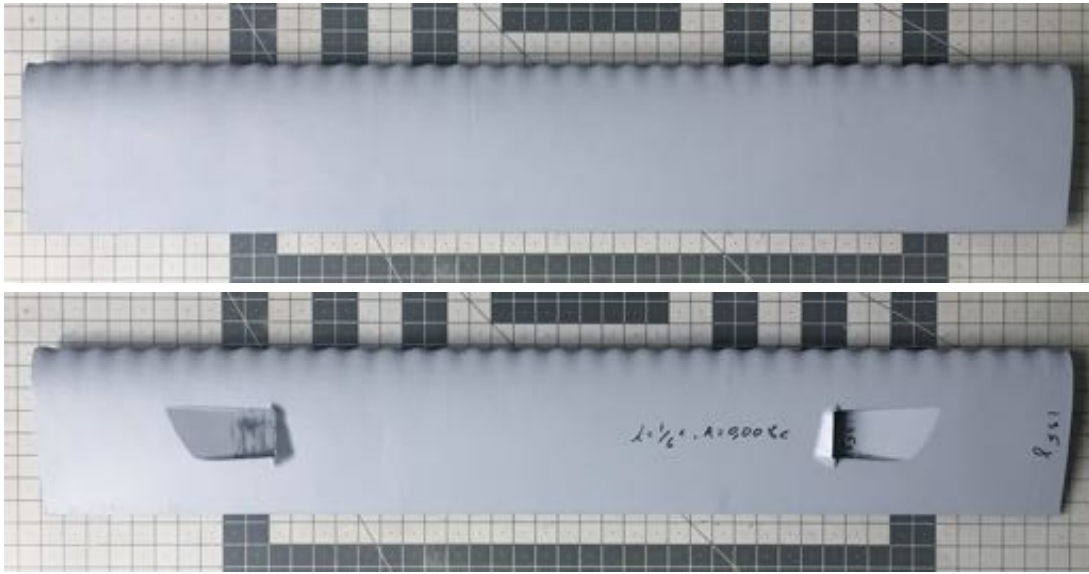
Figure 4.5: Finished blade.

Brass M4 threaded inserts were used in the anchor points to strengthen and increase the longevity of the threads (Fig. 4.6 (a)). Each anchor point indentation was additionally capped with a small part (Fig. 4.6 (b)) in order to minimise the associated flow disturbance.

(a) Brass threaded insert

(b) Blade anchor point

Figure 4.6: Blade assembly details.

Finally, and also to justify the structure described above, it should be mentioned that an initial set of blades was assembled with a less dense internal rib structure and with spars that did not span the entire length of the blades. Above 850 rpm this set of blades was not able to cope with the centrifugal loads and failed, damaging the rotor and destroying all the blades. The blade structure was later revised as described above and the rotational speed was capped at 900 rpm. The final mass of each blade was around 135g, which equates to a reaction force of 270 N (Eq. (1.15)) in both anchor points at $\Omega = 900$ rpm. As such, a static loading of 176 N was applied to each anchor point of the revised blades to verify the validity of this rotational speed limit.

Blade supports

The two blade supports were cut from an aluminium sheet with a thickness of 1.5 mm and stamped to the shape seen in Fig. 4.2 with 3D printed dies (Fig. 4.7) that were clamped and pressed together around the centre section. This also produced the slight angle of the arms, which converted some of the bending moment from the blades' weight into tensile or compression forces.
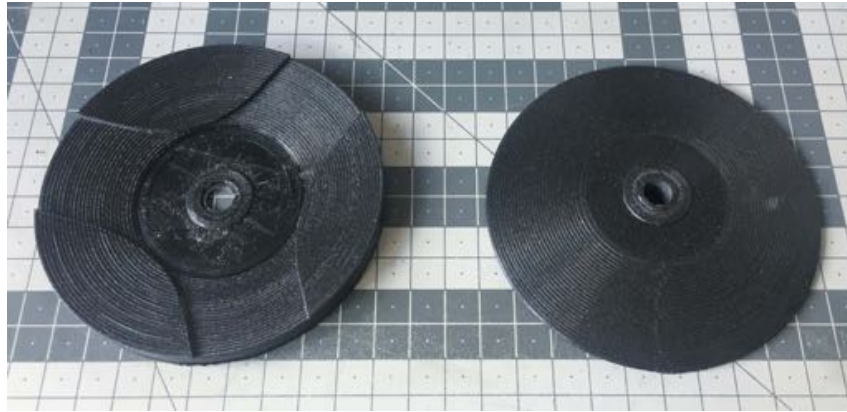
Figure 4.7: Dies used to obtain the final blade support shape.

Both supports are connected to the shaft with 3D printed parts that clamp around it and lock the supports in place (Fig. 4.8). The supports are also bolted to each blade with two M4 bolts (i.e., four bolts per blade) as shown in Fig. 4.6 (b).

(a) Upper support connection

(b) Lower support connection

Figure 4.8: Support to shaft connections.

Shaft

A hollow circular aluminium profile with an outer diameter of 12 mm and a 1 mm wall thickness was utilised as a shaft, to support the rotor and transmit the torque to the turbine base. To decrease oscillations of the whole turbine rotor while in operation, a hollow 10 mm steel profile was pressed inside the aluminium profile to increase the stiffness of the shaft, as seen in Fig. 4.8 (a). Each turbine was balanced after the final installation to also minimise rotor oscillations, especially considering how the shaft is only supported at the bottom.

4.1.2 Base

As stated above, this sub-assembly houses the rotor's bearings and all the mechanical and electrical components required to measure the rotational speed and the torque produced by the turbine, namely, the brushless motor, the load cell and the motor controller. It is also used to secure the turbine to the bottom of the wind tunnel's balance, as seen in Fig. 4.2.
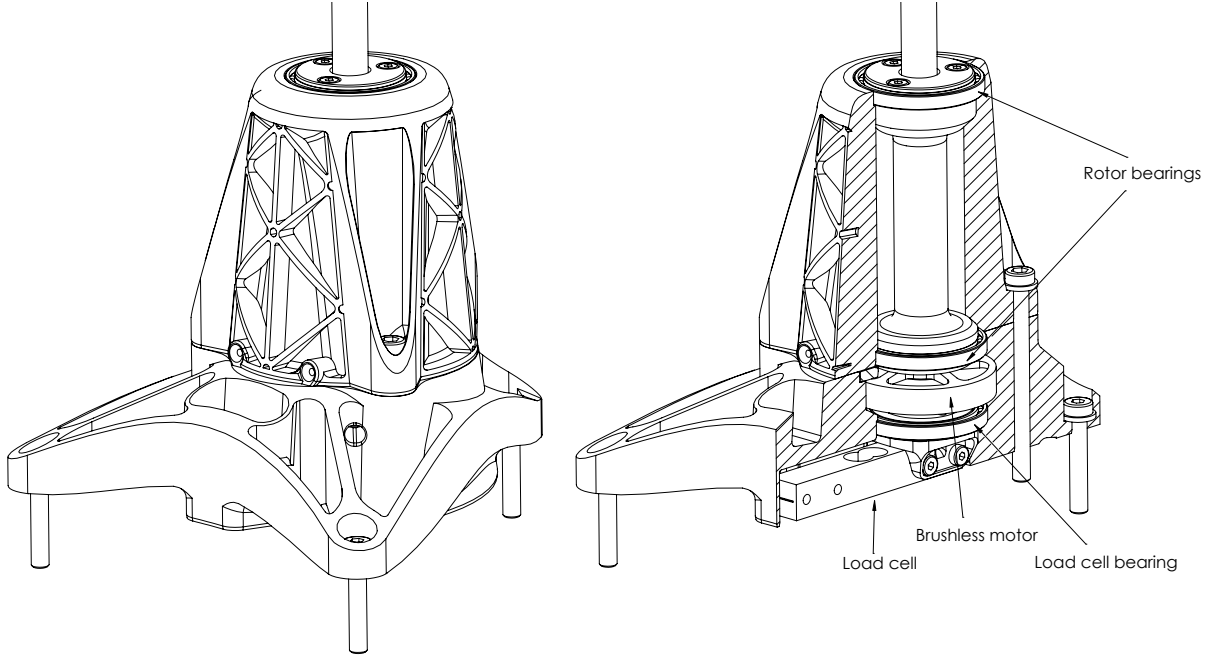
Figure 4.9: Base assembly.

The majority of the structural parts were also 3D printed. Although not solid, as shown in the section view of Fig. 4.4, these parts were printed with a denser internal structure and thicker walls than the blades. In this case, mass was not such a constraint and the structure needed to be strong enough to resist any eventual oscillating loads generated during the turbine's operation.

Rotating assembly

The shaft is coupled to the brushless motor, that is used to apply a braking torque to the rotor, through an aluminium part. The two 6707 deep groove ball bearings that support this rotating assembly are also seated in this aluminium adapter, which is why it had to be turned on a lathe to ensure the necessary concentricity tolerances between the shaft and the bearing seats.

The load cell, used to measure the torque applied by the motor, is supported by a third bearing at one end and is connected to the stator of the motor.

Brushless motor selection

The brushless motor used in this setup is a 3-phase permanent magnet synchronous motor, typically used in multi-rotor drones and, as such, the torque rating is only stated indirectly through the given K_V, velocity constant, value, commonly expressed in rpm/V.

The motor torque constant, K_T can be estimated from the K_V with Eq. (4.1):

$$K_T = \frac{3}{2} \times \frac{1}{\sqrt{3}} \times \frac{2\pi}{60} \times \frac{1}{K_V},$$

(4.1)

where the 3/2 is derived in [75], the $1/\sqrt{3}$ converts from line to phase voltage and $2\pi/60$ converts from rpm to rad/s. The maximum motor torque is then given by:

$$Q_m = K_T I \simeq 8.3 \frac{I}{K_V} \tag{4.2}$$

where I is the maximum current.

The maximum torque produced by the turbine can be estimated with a higher than truly expected maximum $C_Q = 0.03$, which equates to $Q \simeq 0.3 \ N.m$.

A brushless motor with a diameter of 50 mm, $K_V = 360$ and a maximum current of $I = 15 \ A$ was chosen, since this values are equivalent to $Q_m \simeq 0.35 \ N.m$ and therefore larger than the safe estimation of turbine torque.

4.2 Dimensional verification

Before printing any parts, the conversion factor between motor steps and axis travel was adjusted for each of the three axes of the 3D printer, with the purpose of achieving suitable dimensional tolerances on all printed parts.

Table 4.1 compares the dimensions of the finished blades, with the desired dimensions.

Table 4.1: Blade dimensions verification.

	Blade height [mm]	Chord length [mm]	Maximum thickness [mm]
Target	450.00	75.00	13.50
Average baseline blades	450.67	75.13	13.47
Average modified blades	450.83	74.10	13.45

The only discrepancy considered meaningful was registered in the chord length of the modified blades ($\sim 1 \ mm$). Since the maximum blade thickness did not also show a similar disparity from the target value, the difference in chord length was attributed to a slight deviation in the trailing edge geometry that was somewhat amplified in the printing process (due to the relative thinness of the trailing edge).

Therefore, this difference in the chord value was not included in the evaluation of the experimental results because the majority of the airfoil's geometry was not affected.

4.3 Instrumentation

The variables that needed to be measured in order to evaluate the turbine's performance were: the wind speed, U_∞; the torque produced by the turbine, T; and the rotational speed of the rotor, Ω.

With this, the following dimensionless coefficients can be obtained:

Tip speed ratio, λ.
$$\lambda = \frac{\Omega R}{U}, \ \text{with} \ U = U_\infty \tag{4.3}$$

Torque coefficient, C_Q.
$$C_Q = \frac{Q}{\frac{1}{2}\rho U_\infty^2 A} \tag{4.4}$$

Power coefficient, C_P.
$$C_P = \frac{Q \ \Omega}{\frac{1}{2}\rho U_\infty^3 A} \tag{4.5}$$

4.3.1 Wind speed

The flow speed in the test section was measured with the FCO12 micromanometer from Furness Controls Limited, which displayed the dynamic pressure between the stagnation port, located just before the start of the test section, and the static (atmospheric) pressure. The pressure differential is displayed in mmH_2O with a precision of $\pm 1\%$, after calibration using a Betz manometer..

The wind speed is obtained from Eq. (4.6), where Δh is the dynamic pressure in mH$_2$O.

$$U_\infty = \sqrt{\frac{2 \; \Delta h \; \rho_{H_2O} \; g}{\rho_{air}}} \tag{4.6}$$

The air temperature was also measured before each test and taken in to account to calculate the air density (ρ_{air}) with Eq. (4.7), where P_{atm} is the atmospheric pressure, $R_{specific}$ is the specific gas constant of air, and T_{air} is the air temperature.

$$\rho_{air} = \frac{P_{atm}}{R_{specific} \; T_{air}} \tag{4.7}$$

4.3.2 Turbine torque

As stated above, the torque produced by the turbine is measured indirectly by the load cell installed at the base. The braking torque applied by the brushless motor is controlled through the VESC 4.20 motor controller and the load cell measures the reaction force applied by the motor stator on the stationary turbine structure (Fig. 4.10). Since the load cell and the motor stator are both supported by a third bearing, only the friction forces in these three bearings are not captured in the torque measurement.
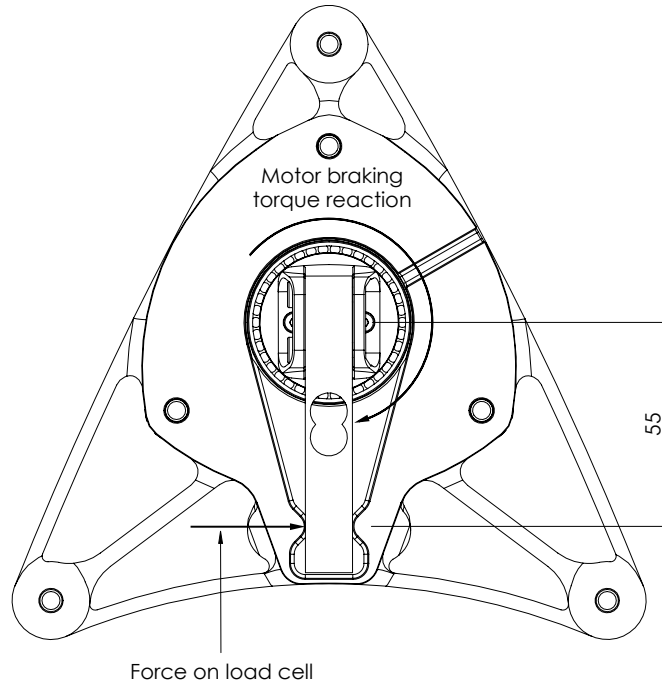

Figure 4.10: Torque measurement diagram.

The dynamic torque produced by the turbine is thus calculated from:

$$Q = F_{Load\;cell} \cdot d = F_{Load\;cell} \cdot 0.055 \tag{4.8}$$

Torque measurement calibration

The torque value measured through the load cell was zeroed at the beginning of each measurement. However, the measurements had to be calibrated so that the load cell's voltage drop, registered by the Analog-to-Digital Converter (ADC), was properly converted to force units.

The calibration setup is described in Fig. 4.11. A lever arm was clamped around a shaft, coupled directly to the motor rotor, and a known mass was suspended from the tip of the arm through a string and a pulley. This way, a constant known torque could be applied to the load cell, while the motor was rotating with a constant speed, simulating the dynamic torque measurement of the turbine's rotor.
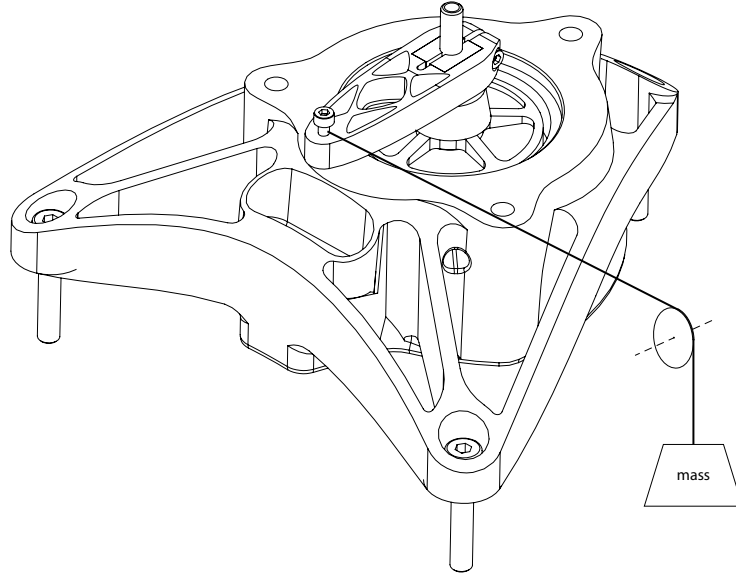
Figure 4.11: Torque calibration setup.

Three different weights were used; for each, the clamping force to the shaft was adjusted so that the arm stayed perpendicular with the string. The conversion factor was repeatedly adjusted, in the Arduino's firmware, until the difference between the applied and measured torque was negligible. The results of the final calibration are shown in table 4.2.

This way, any systematic errors of the system were minimised, being substituted only by the systematic error associated with the measurement of the mass of the three weights.

Table 4.2: Final calibration results.

Mass [g]	Applied torque [$N \cdot mm$]	Load cell measurements [$N \cdot mm$]			
		Mean	Standard uncertainty	Error	Error [%]
25	12.263	12.123	0.206	-0.140	-1.139
41	20.111	20.416	0.226	0.306	1.521
63	30.902	30.765	0.287	-0,136	-0.440
Mean			0.240	0.010	-0.019

4.3.3 Rotor rotational speed

The brushless motor used is a small synchronous three phase motor and, as such, the electric rotational speed, $eRPM$, can be sourced directly from the motor controller in real-time. The actual rotational speed is obtained by dividing the $eRPM$ value by the number of pole pairs of the motor, in this case seven:

$$\Omega = \frac{eRPM}{7} \ rpm \tag{4.9}$$

Rotational speed measurement validation

An optical tachometer was used to validate the rotational speed values measured by the motor controller, at various different speeds. The measured values were found to be within ± 1 rpm of the tachometer values. Fig. 4.12 shows the sampled data of one of these measurements.
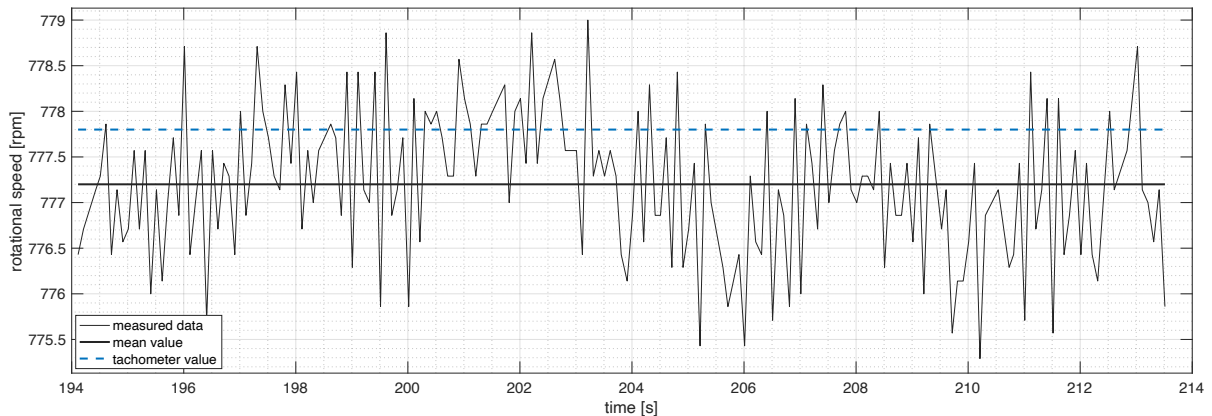

Figure 4.12: Rotational speed validation at 777 rpm.

4.3.4 Data acquisition

An interface was created in MATLAB to control the braking torque applied by the motor and to acquire and save all the data. All the components required for the torque and rotational speed measurement were connected as is shown in the wiring diagram in Fig. 4.13.

An Arduino Nano V3.0 micro-controller was used to establish the connection between the MATLAB interface and the VESC motor controller. The interface is connected through USB to the micro-controller, which in turn receives the Serial rotational speed data from the motor controller and relays the required motor braking current value (in mA).

A three cell (11.1 V) lithium polymer battery was used to receive the power generated by the motor, when under braking, or to supply the necessary current to spin up the turbine, when it failed to self-start, for example.

Regarding the torque measurement, the voltage drop in the load cell, proportional to the applied force, is registered by an HX711 ADC, sent through I^{2}C to the Arduino, and subsequently transmitted to MATLAB. This force value is converted in to torque ($N \cdot mm$) directly in the Arduino's firmware with the constant determined in the calibration process.

The desired applied braking torque is modulated through the MATLAB interface in real-time with the motor current slider, seen in Fig. 4.14. Additionally, the torque and rpm data are plotted, also in real-time, in the interface, as shown in the screenshot in Fig. 4.14.
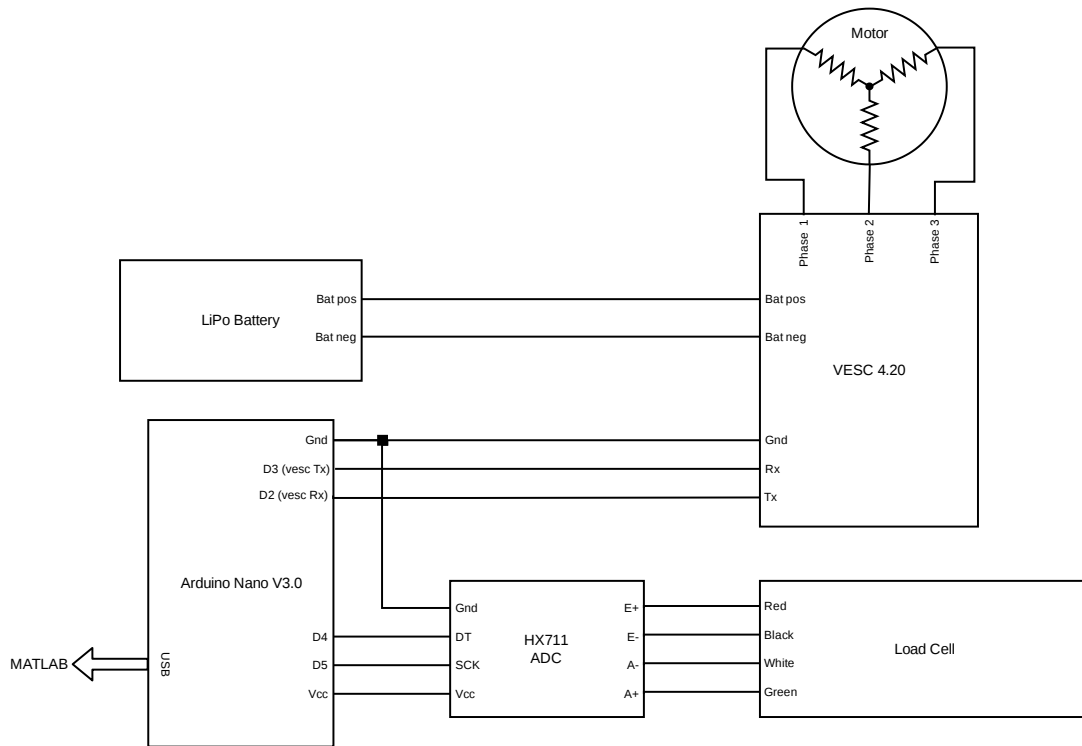
Figure 4.13: Turbine wiring diagram.

The wind speed was also calculated by the interface, from the temperature and dynamic pressure inputs, and saved alongside the torque and rotational speed values.
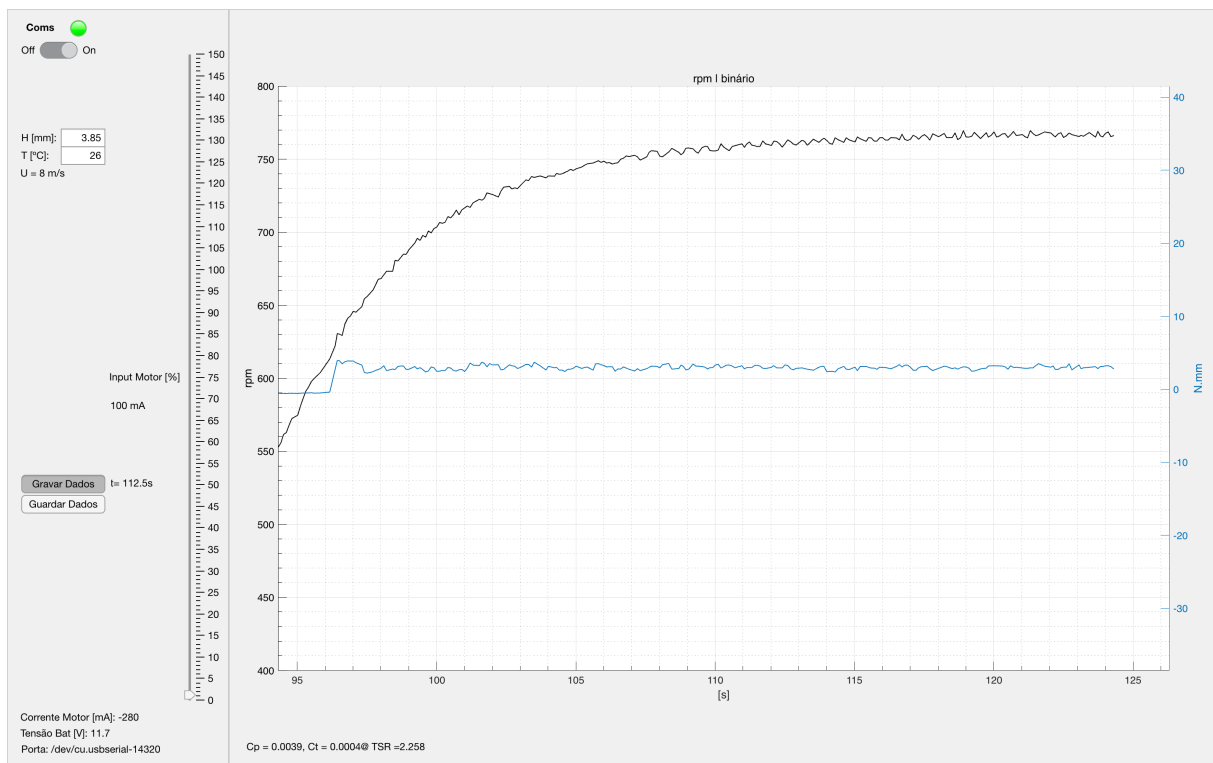

Figure 4.14: MATLAB interface.

5 Experimental results

In order to properly evaluate the possible performance improvements of the leading edge modifications, two similar sets of blades were printed and tested: one with an unmodified leading edge (baseline) and another with the best modified geometry suggested by the CFD parametric study—$\lambda_{vg} = 1/6c$; $A_{vg} = 0.008c$.

The performance of both geometries was measured throughout the whole tip speed ratio range and at multiple wind speeds, starting from the lowest value at which both turbines were not capable to self-start until the maximum flow velocity allowed by the wind tunnel. The start-up behaviour and performance of both were also measured in the entire wind speed spectrum.

5.1 Measurement methodology

Every measurement followed the same procedure, exemplified in Fig. 5.1. This process can be summarised by:

1. The turbine rotor is locked and the flow velocity is increased until the desired value.

2. Once the flow velocity stabilises, the rotor is released.

3. In order to evaluate the starting performance of the turbine, no braking torque is applied while the rotational speed increases (apart from the friction torque from the motor, which is registered by the load cell). This corresponds to approximately the section between 0 and 85 seconds in Fig.5.1

4. When the maximum rate of rotation is reached and stabilises, the applied braking torque can be progressively increased until the maximum torque point, after which the torque should be adjusted to allow the rotor to decelerate relatively smoothly. In the first phase, the torque should be increased relatively slowly, as to prevent any rotational inertia effects on the measurements.

For each rotor geometry, the previous procedure was repeated at least three times for every wind speed value tested.

All experimental data was post-processed in MATLAB.

5.2 Experimental error sources and uncertainty analysis

The 95% coverage interval (analogous to the confidence interval) was calculated through the following process to quantify the uncertainty in the power coefficient measurements.

5.2.1 Error sources

To this end, several potential systematic and random error sources were identified throughout the measurement processes of all the variables used to calculate the C_P (Eq. 1.12).
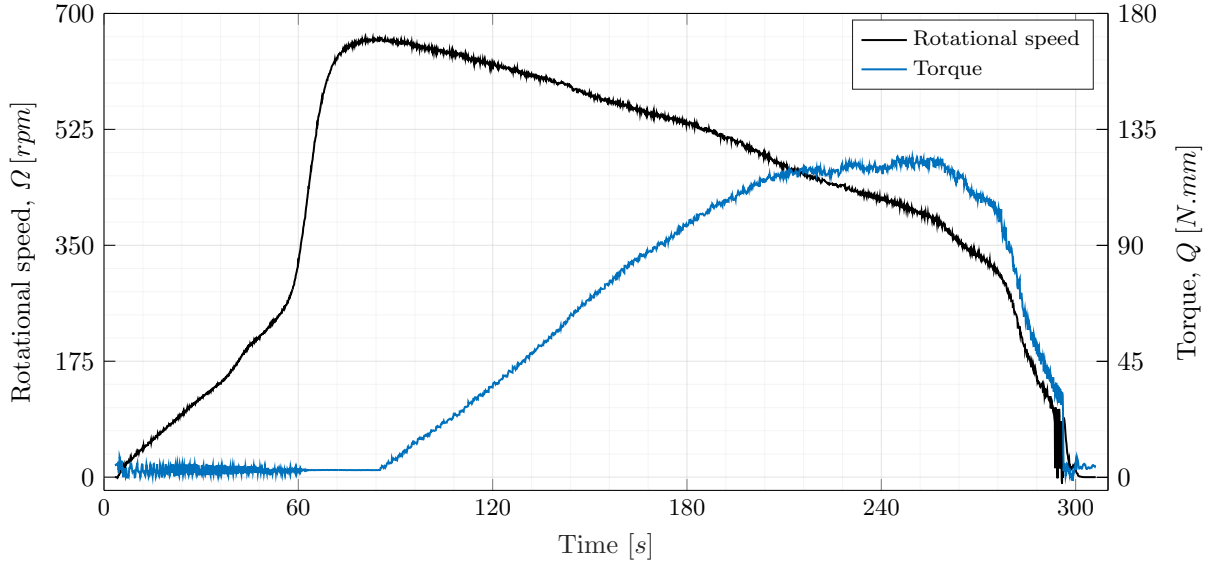
Figure 5.1: Untreated measured data, $U_\infty = 7 \ m/s$.

Torque measurement

Even though the torque value was zeroed before each measurement, there is still signal drift associated to a random error from all the environmental disturbances. The scale used in the calibration process, described in 4.3.2, also introduced a systematic error, quantified by its resolution, $\pm 1 \ g$, equivalent to $\pm 0.5 \ N \cdot mm$ in this case.

Concerning the random error, a normal distribution was assumed, with an estimated standard deviation equal to the mean standard uncertainty obtained in the calibration process.

Rotational speed measurement

The random uncertainty associated with the angular speed measurement was also quantified with values from the validation process. Similarly to the random torque error, the assumed normal distribution's standard deviation was taken from the validation data shown in table 5.1.

Table 5.1: Standard uncertainty from rotational speed measurements made during the validation process.

[rpm]	Measurement 1	Measurement 2	Measurement 3
Mean	480.305	672.535	777.197
Standard uncertainty	2.000	1.666	0.800

Wind speed measurement

The systematic error related with the calculation of U_∞ through Eq. (4.6) was also quantified with the precision of the manometer utilised, equivalent to $\pm 0.01 \ m/s$.

To summarise, the error sources described above were compiled in table 5.2.

Table 5.2: Error sources.

Measurements	Torque [$N \cdot mm$]		Ω [rpm]	U_∞ [m/s]
	random (ε_Q)	systematic (β_Q)	random (ε_r)	systematic (β_U)
Source(s)	load cell	calibration	arduino, motor, motor controller	manometer
Distribution	normal	uniform	normal	uniform
Standard deviation	0.240	—	1.488	—
Amplitude	—	±0.5	—	±0.01

Additional uncertainty between measurements

Notwithstanding, the data from three consecutive measurements plotted in Fig. 5.2 clearly shows a drift in the value of C_P that varies with λ and from one measurement to another. This uncertainty is visibly larger than the dispersion covered by the random errors from the torque and Ω measurements and is also not enveloped by the systematic errors sources identified.

Most likely, this error occurs as a result of small variations in air temperature, load cell temperature and mechanical friction, as the bearings heat up under operation. The torque applied by the brushless motor also becomes progressively more scattered around the mean value for large torque values and low rotational speeds, which is a possible additional source of uncertainty at these conditions.
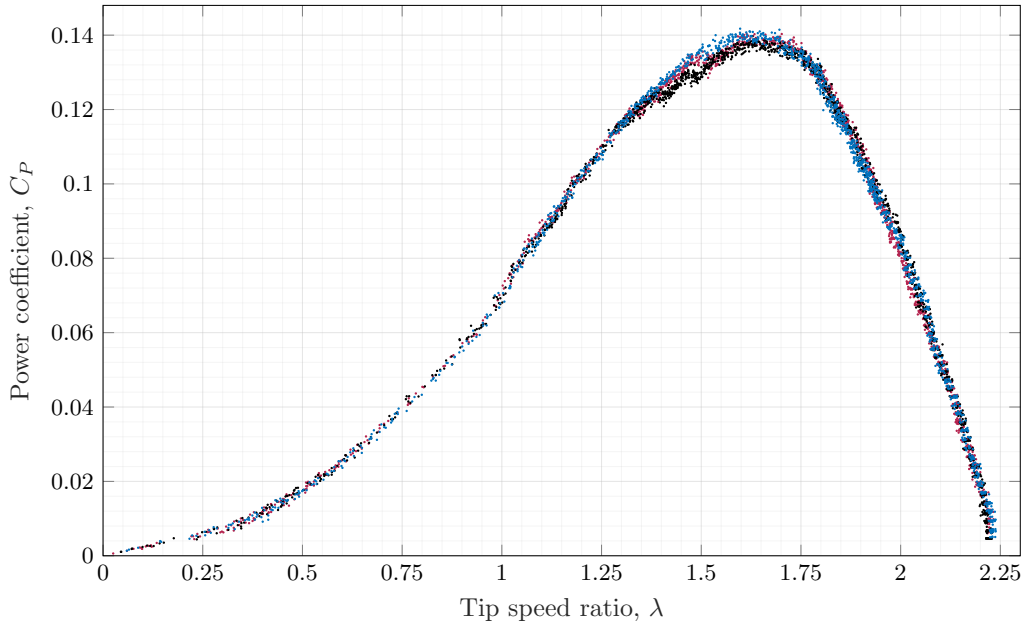
Figure 5.2: Scatter plot of the three measurements performed at $U_\infty = 7$ m/s in the turbine with the modified leading edge.

In order to include this uncertainty in the coverage interval calculation, another normally distributed random error is considered, ε_{Cp}. For each set of measurements at a specific flow speed, a standard uncertainty is obtained as a function of the tip speed ratio, using the mean value of each measurement.

5.2.2 Coverage interval calculation

The coverage intervals were determined by propagating all the errors through the equations used to calculate the C_P, using a Monte Carlo method, as described in [76].

The distribution of C_P values for a specific λ is first determined through an iterative process with M iterations. For every iteration (i), an error value is randomly sampled from the distribution assumed for each error source and is then added to the corresponding variable. In this case:

$$Q(i) = Q_{true} + \varepsilon_Q(i) + \beta_Q(i), \tag{5.1}$$

$$\Omega(i) = \Omega_{true} + \varepsilon_r(i), \tag{5.2}$$

$$U_\infty(i) = U_{\infty\ true} + \beta_U(i). \tag{5.3}$$

The *data reduction equation*, i.e., Eq. (1.12), is then used to calculate the C_P for each iteration:

$$C_P(i) = \frac{Q(i)\Omega(i)}{\frac{1}{2}\rho U_{\infty(i)}^3 A} + \varepsilon_{Cp}. \tag{5.4}$$

From the distribution of C_P, the *95% coverage uncertainty limits*, $C_{P\ low}$ and $C_{P\ high}$, are then obtained through:

$$C_{P\ low} = \text{result number}(0.025M) \tag{5.5}$$

$$C_{P\ high} = \text{result number}(0.975M). \tag{5.6}$$

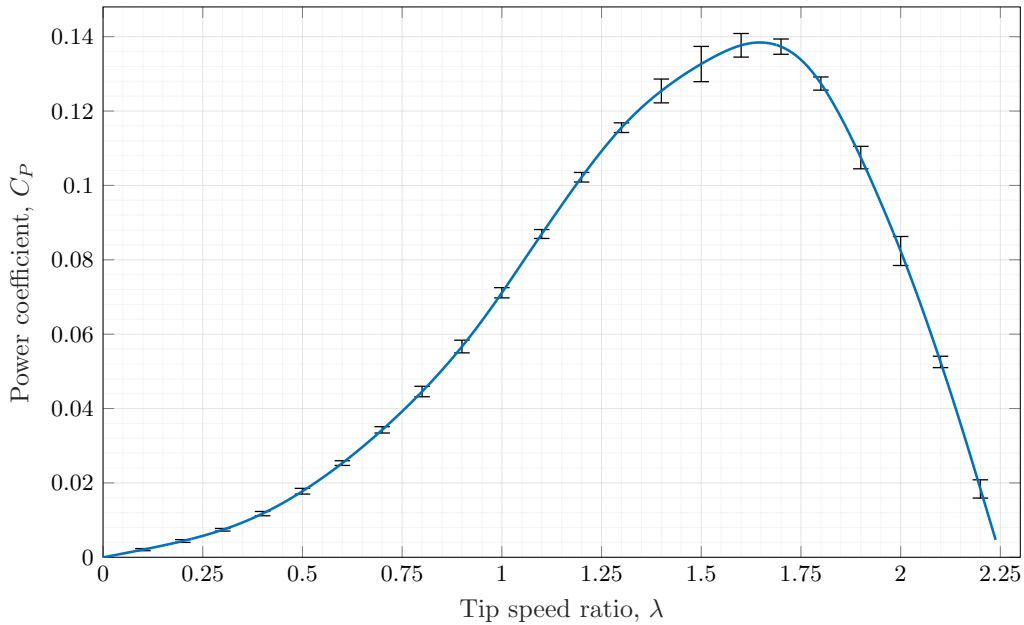For the set of measurements exhibited in Fig. 5.2, the 95% coverage interval obtained is shown in Fig. 5.3.

Figure 5.3: C_P curve with coverage interval for $U_\infty = 7\ m/s$, $M = 100000$.

5.3 Turbine start-up behaviour

H-Darrieus turbine are notorious for their poor starting performance. The start-up operation of both geometries was tested and compared, as it is an important factor in the overall power generation capabilities

of each turbine, particularly in varying wind speed conditions.

5.3.1 Sensitivity to azimuth angle

The sensitivity of the self-starting behaviour to the azimuthal blade position, θ, was evaluated in the first place.

Both blade geometries performed similarly: they were both able to achieve rotation, without external input, in almost all positions. In a small interval around $\theta = 40° + n120°$, however, the stationary torque produced by each blade cancelled out and neither turbine was able to initiate operation. This behaviour persisted throughout the entire wind speed range analysed, even if at higher values the interval where the rotor remained stationary seemed to shrink slightly, possibly aided by the increased turbulent flow around the stationary blades.

The leading edge protuberances did not have any meaningful impact in this behaviour, they possibly contributed to a slightly smaller no-start interval around $\theta = 40° + n120°$, however, if present, this effect would be too insignificant to quantify.

This sensitivity to blade position is intrinsic to most straight bladed Darrieus designs and is typically solved with the implementation of helical (Gorlov) rotor configurations.

5.3.2 Self-starting performance

The self-starting performance of both tested geometries was evaluated and compared, in several wind velocities, with the maximum rotational speed achieved by each design, Ω_{max}, and with the time elapsed between rest and Ω_{max}.

It was observed that, for a specific increment in wind speed, each turbine experienced a significant increase in the maximum tip speed ratio achieved, from around $\lambda_{max} < 0.5$ to $\lambda_{max} > 2$. As such, if the turbine was not able to reach speeds clearly above $\lambda = 0.5$, it was determined that it failed to self-start, even if said turbine was capable of achieving nominal operation, in the same wind conditions, by externally increasing its speed above $\lambda \sim 1$.

Having said this, its clear from the data shown in Table 5.3 that both turbines failed to start at $U_\infty = 5.5\ m/s$, so no lower speeds were tested. The start-up analysis was also only performed up to $U_\infty = 8.5\ m/s$, seeing how testing the turbines' unrestrained performance above this flow velocity would exceed the stipulated rotational speed limit (900 rpm).

Table 5.3: Self-starting performance.

$U_\infty\ [m/s]$	$\Omega_{max}\ [rpm]\ /\ \lambda_{max}$		Time to $\Omega_{max}\ [s]$	
	Baseline	$\lambda_{vg} = 1/6c;\ A_{vg} = 0.008c$	Baseline	$\lambda_{vg} = 1/6c;\ A_{vg} = 0.008c$
5.5	48 / 0.21	92 / 0.39	—	—
6.0	62 / 0.24	557 / 2.19	—	212
6.5	121 / 0.44	602 / 2.18	—	113
7.0	137 / 0.46	660 / 2.22	—	77
7.5	693 / 2.18	725 / 2.28	164	63
8.0	770 / 2.27	782 / 2.30	100	58
8.5	820 / 2.27	838 / 2.32	88	48

Influence of leading edge protuberances

Figure 5.4 summarises the start-up performance comparison between the baseline and the modified turbine. The significant performance improvement provided by the leading edge vortex generators is evident.
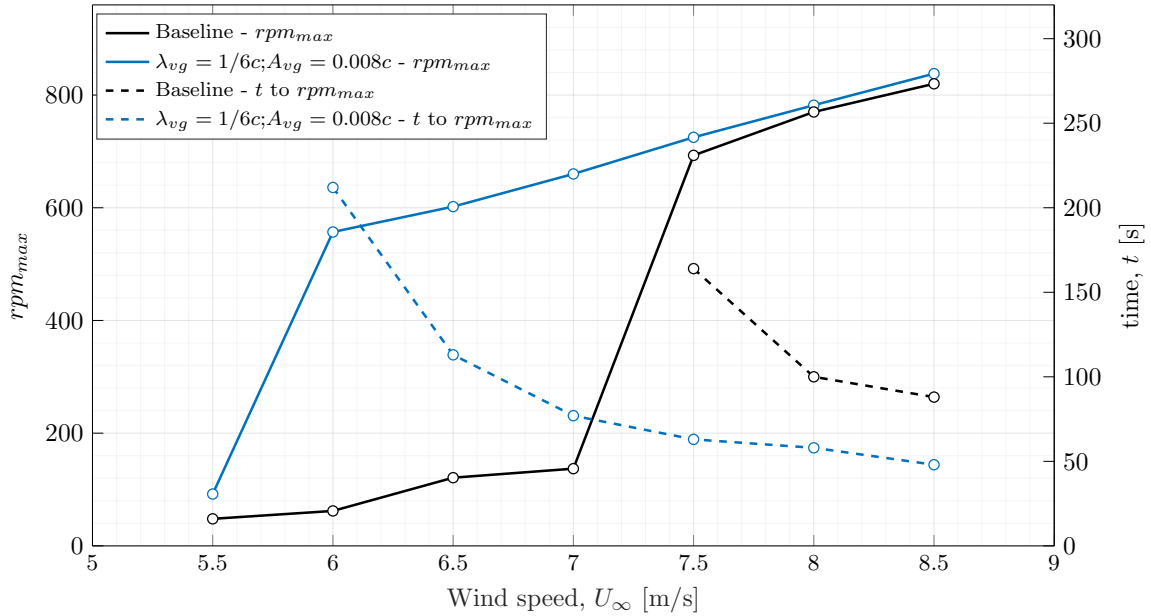

Figure 5.4: Self-starting performance comparison.

The leading edge protuberances not only improved considerably the wind speed at which the turbine is able to self-start and achieve nominal operation—the modified turbine self-starts at 20% lower wind speeds—but also reduced the time necessary to reach said nominal operation. For the flow conditions where both rotors achieved nominal speeds, $U_\infty = 7.5$ - 8.5 m/s, the time to reach λ_{max} was on average 50% smaller.

Even if the efficiency of the turbine had not improved with the leading edge vortex generators, this enhancement of the start-up performance alone would still be beneficial to the real-world power output. In varying wind speed environments, faster and earlier start-up equates to less time not producing power once the wind conditions became favourable.

5.4   Turbine performance

To quantify and compare the performance of the baseline with the optimised turbine, the torque, rotational speed and wind speed values obtained in each wind tunnel test were compiled in to standard C_P versus tip speed ratio curves.

In the wind velocities were each turbine failed to start, the rotating speed was increased by the brushless motor until $\lambda \sim 1$, where both turbines were able to achieve what can be considered nominal operation, even at the lowest values of U_∞. Note that this does not influence the performance results in any way, only the start-up process.

The maximum C_P values alone show that this leading edge modification significantly improved the efficiency, and consequently, the performance of the turbine throughout the whole analysed range of flow velocities (see Fig. 5.5).

As the wind speed increases, the efficiency gain decreases progressively from above 40% to around 20%. This diminishing improvement seems to be, however, a result of a slight increase in performance from the baseline turbine, seeing how much smoother the optimised turbine's C_{Pmax} progression is,

especially between $U_\infty = 7\ m/s$ and $U_\infty = 8\ m/s$ (which also coincides with the range were the baseline turbine no longer fails to self-start; Fig. 5.4).

Since the range of tip speed ratios remains more or less the same throughout all the measurements, this behaviour seems to indicate that the performance progression of the modified turbine is also slightly less sensitive to changes in Reynolds number, at least in this range.

Table 5.4: Maximum power coefficient values.

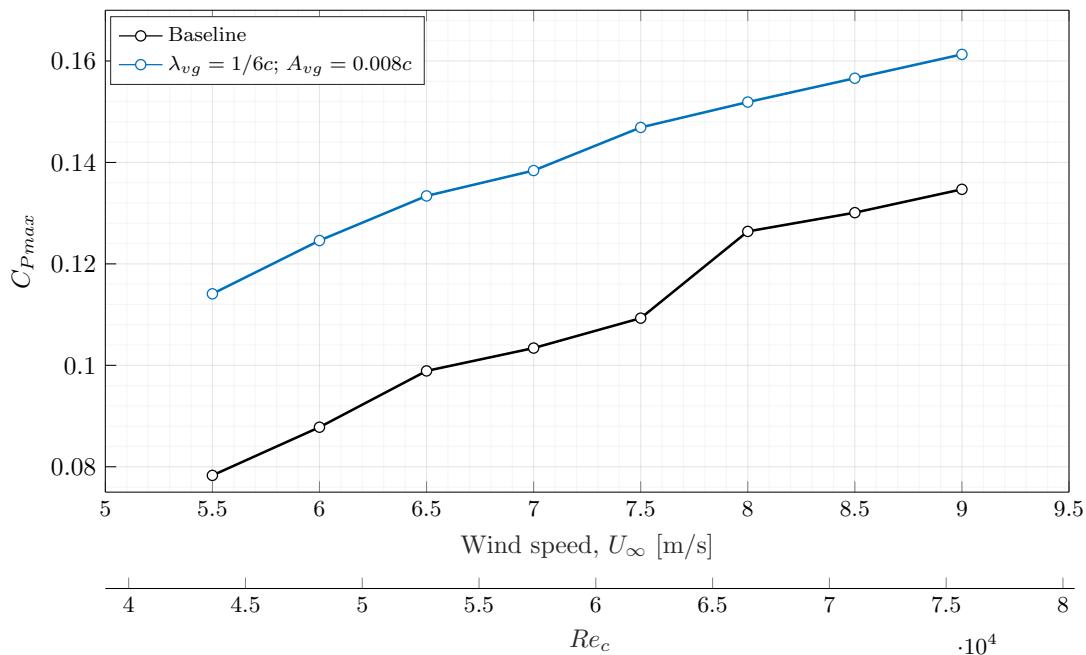| $U_\infty\ [m/s]$	C_{Pmax}	
	Baseline	$\lambda_{vg} = 1/6c;\ A_{vg} = 0.008c$
5.5	0.0783	0.1141
6.0	0.0878	0.1246
6.5	0.0989	0.1334
7.0	0.1034	0.1384
7.5	0.1093	0.1469
8.0	0.1264	0.1519
8.5	0.1301	0.1566
9.0	0.1347	0.1613

Figure 5.5: Maximum power coefficient comparison.

The C_P curves (Fig. 5.6 to 5.13) complement this analysis by indicating that the tip speed ratio at which maximum power output occurs is almost not affected by the leading edge modification. Additionally, it is also apparent that the performance improvement is roughly proportional to the C_P in the entire λ range only until $U_\infty = 6.5\ m/s$. Above $U_\infty = 7\ m/s$, the leading edge protuberances only provide a noticeable improvement above $\lambda \sim 1$.

The curves at $U_\infty = 9\ m/s$ seem to deviate from this behaviour, even with the modified leading edge line dipping below the baseline; however, the uncertainty is also higher in this section ($\lambda \sim 1-1.5$), most likely due to the higher torque required from the motor at these tip speed ratios and higher U_∞.

As mentioned in chapter 4, the turbine's shaft was only supported at the bottom, which made the turbine rotor somewhat susceptible to increased oscillations during operation.

Both rotors were balanced beforehand and were brought to their maximum rotational speed at $U_\infty = 0$ m/s without showing any meaningful vibrations.

It was therefore concluded that the occasional rotor oscillations observed were perhaps caused by fluctuating aerodynamic loads matching the harmonic frequencies of the system.

In this respect, the turbine with the modified blades also showed less significant oscillations in this situations, which is consistent with lower intensity dynamic stall conditions producing weaker fluctuating aerodynamic loads on the blades.
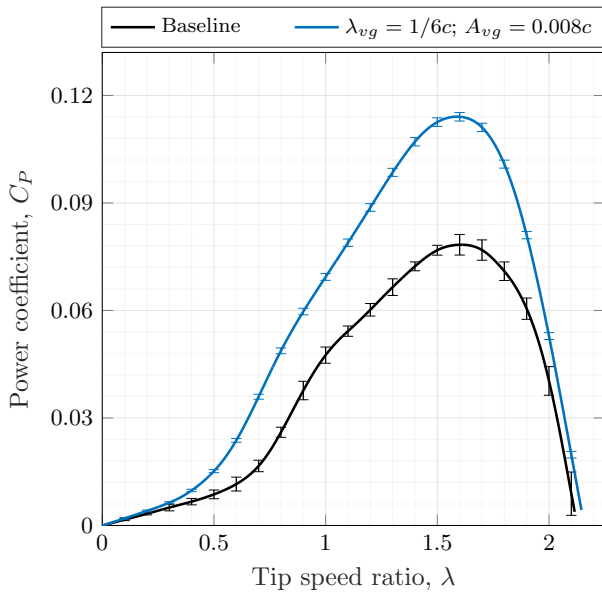

Figure 5.6: $U_\infty = 5.5$ m/s.

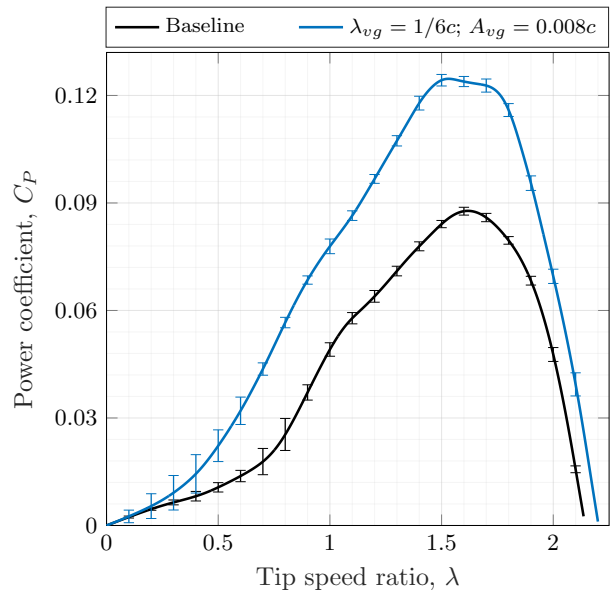Figure 5.7: $U_\infty = 6$ m/s.

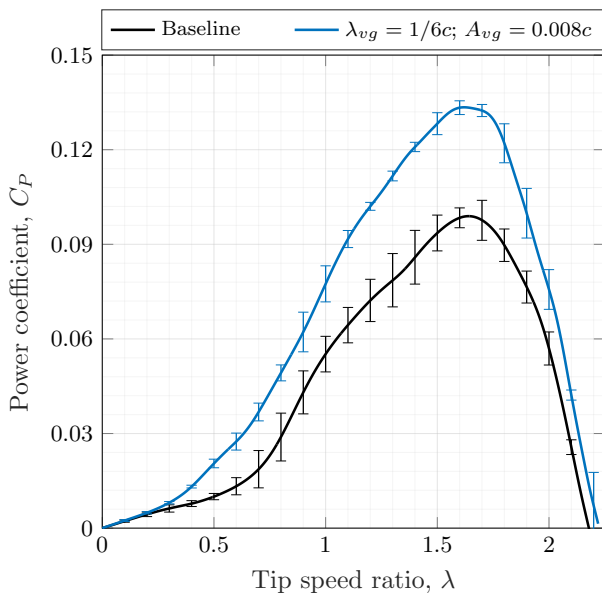Figure 5.8: $U_\infty = 6.5$ m/s.
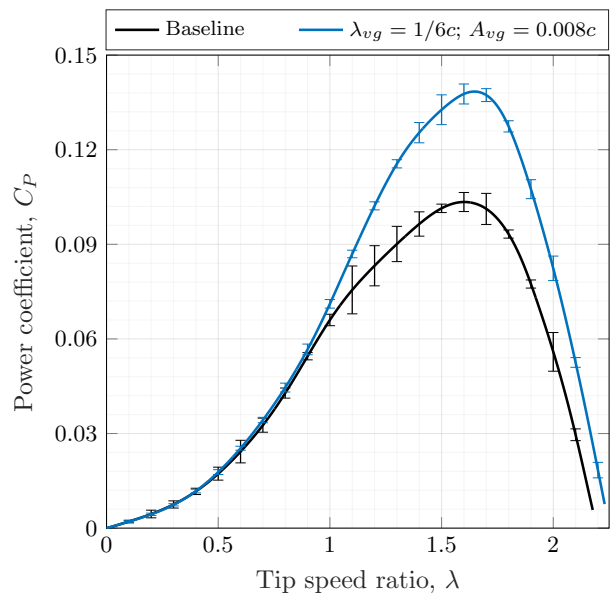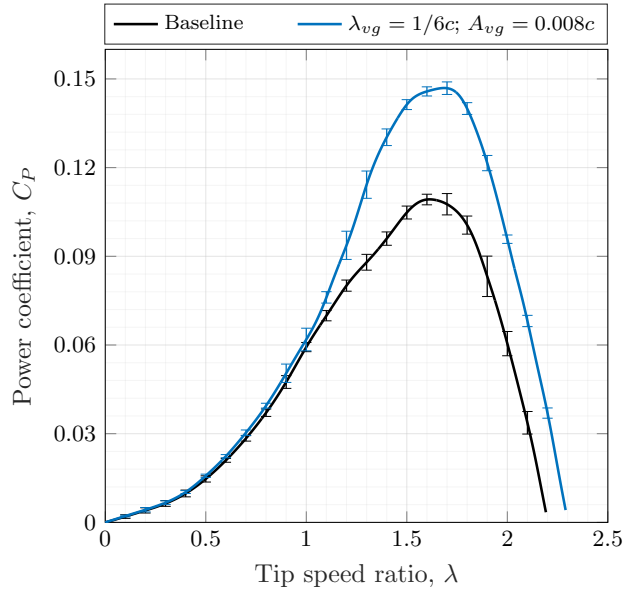

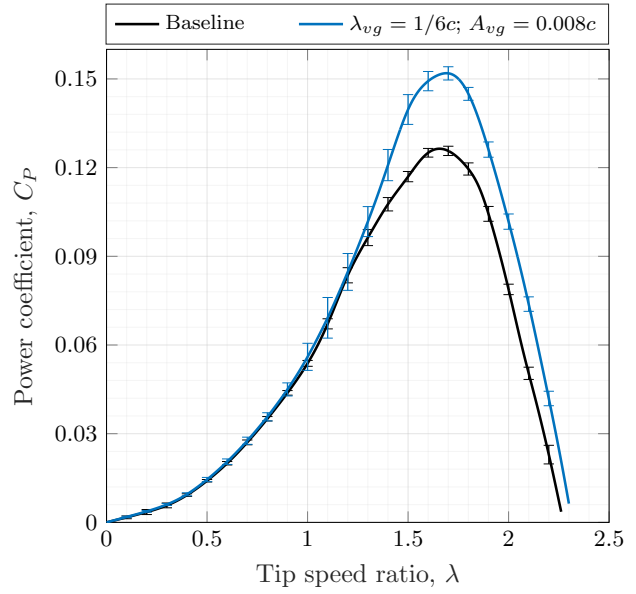Figure 5.9: $U_\infty = 7$ m/s.

Figure 5.10: $U_\infty = 7.5\ m/s.$

Figure 5.11: $U_\infty = 8\ m/s.$
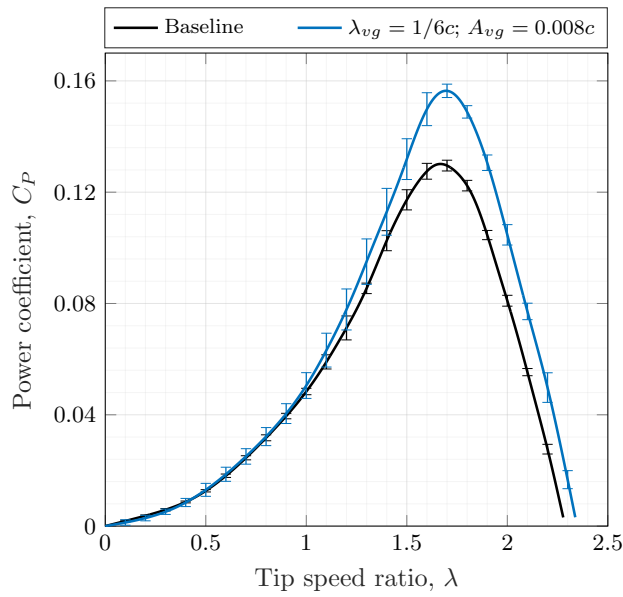

Figure 5.12: $U_\infty = 8.5\ m/s.$
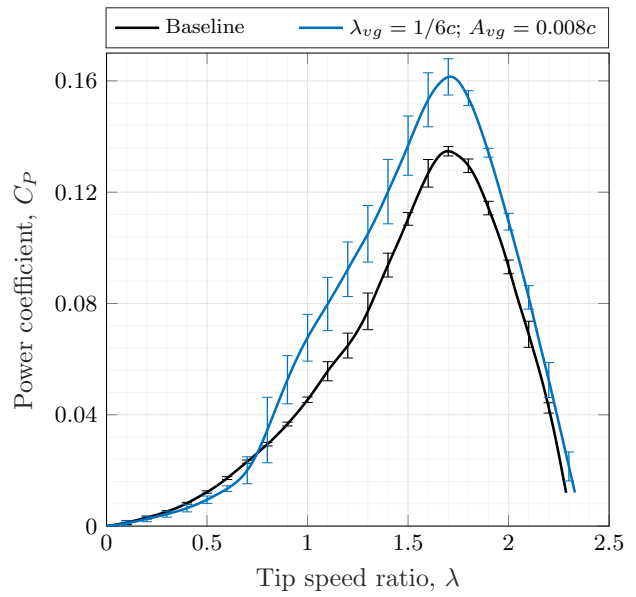

Figure 5.13: $U_\infty = 9\ m/s.$

6 Half-turbine simulation

The aim of this set of simulations was mainly to validate the mesh and the models used throughout the numeric analysis, seeing how it would not be reasonable to directly compare the infinite blade results with the experimental values. As such, the best modified leading edge geometry suggested by the initial infinite blade study was used: $\lambda_{vg} = 1/6c$; $A_{vg} = 0.008c$.

6.1 Problem definition

All the same inlet and rotational speed conditions were maintained from the infinite blade simulations—i.e., $U_\infty = 8 \ m/s$, $\Omega = 560 \ rpm$ and $\lambda = 1.65$.

The turbine's performance was also evaluated in the same way; the C_P was obtained from the torque value averaged over one full rotation, once the torque curve had stabilised.

6.2 Mesh

Similarly, the same mesh configuration and refinement patterns were carried over from the infinite blade study, seeing how the mesh used for the previous infinite blade simulations was essentially a slice of the mesh used in the present analysis.

6.2.1 Domain and boundary conditions

The parameters of the computational domain were also based on those used in [46] with some key differences, seeing how the rotor used has a different aspect ratio and how only half of the flow around the turbine is being modelled.

The inlet and outlet boundary conditions were carried over from the infinite blade simulations. All other external regions, including the bottom plane (mid-plane), were likewise defined with symmetric boundary conditions, in order to approximate the free-stream flow conditions around a complete turbine.

The domain was again split into a rotating and a stationary volume (Fig. 6.1 and 6.2) so that a similar sliding mesh configuration could be used to model the rotating physics of the turbine rotor.

In the rotating volume (Fig. 6.2), two of the outside surfaces interfaced with the stationary volume and the bottom region was also defined as a symmetry boundary. All turbine surfaces (i.e., blades, shaft, and blade supports), were set as no-slip walls.
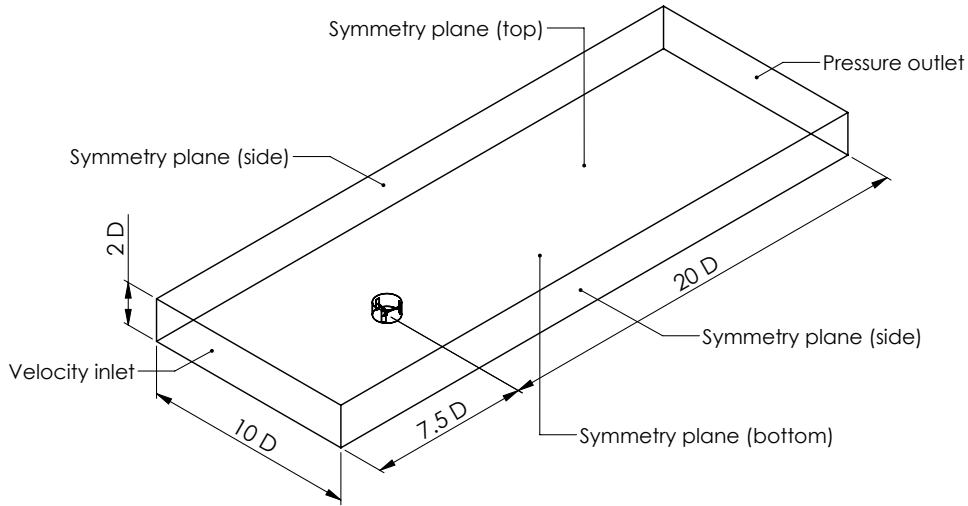
Figure 6.1: Stationary volume.
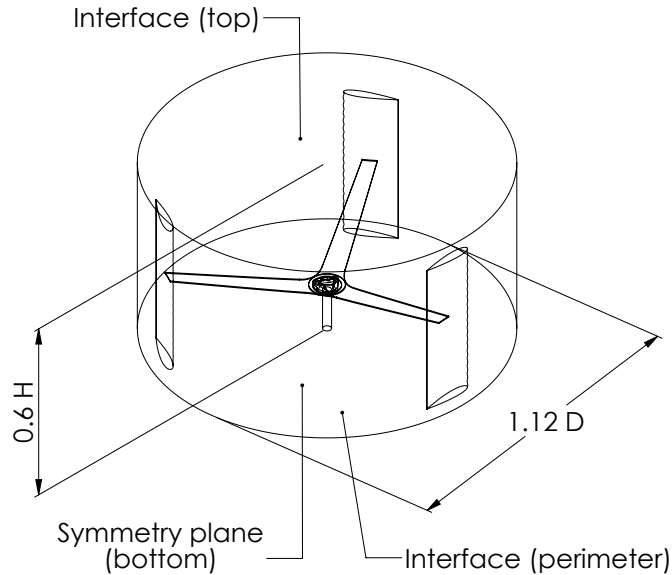
Figure 6.2: Rotating volume.

6.2.2 Mesh settings

The mesh refinement in all regions was similarly defined in function of the cell resolution on the blade's surfaces, Fig. 6.3 (b). The prism layers and refinement pattern around the rotor, Fig. 6.3 (a), and the initial wake section, Fig. 6.4, were also defined to match the infinite blade mesh and the mesh described in [46].

6.2.3 Mesh resolution sensitivity analysis

To determine the final mesh resolution, the whole domain was also incrementally refined until the C_P values showed an acceptable convergence. Given the progressively higher cost of each simulation and the fact that this numerical analysis was only meant to indicate the best leading edge configuration, the convergence shown in table 6.1 was deemed adequate to establish that increasing the mesh refinement above the resolution defined by a blade surface element with 0.75 mm was not worthwhile (in both turbulence models).

(a) (b)
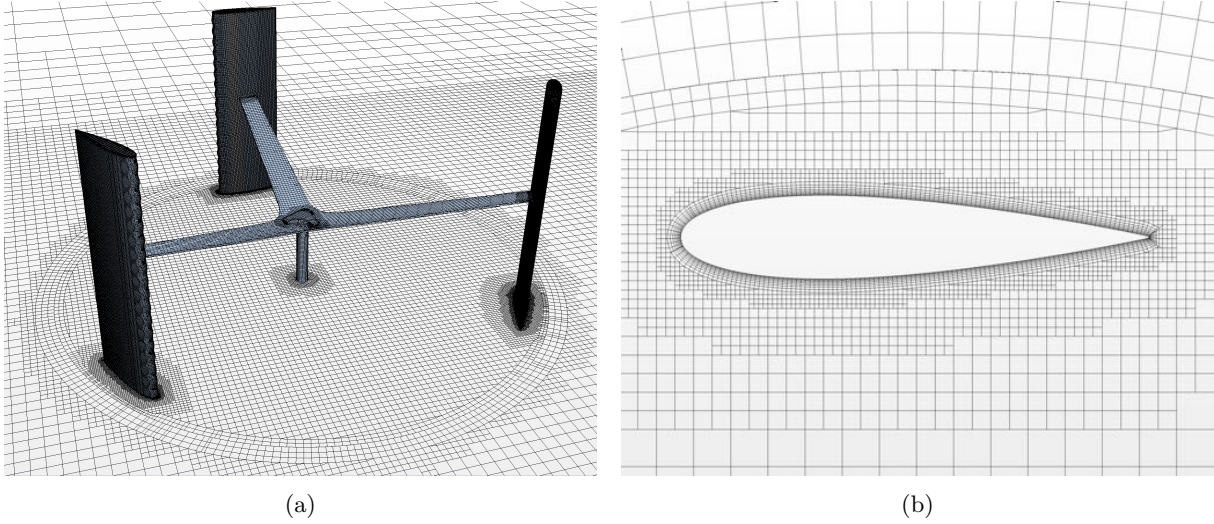
Figure 6.3: Mesh over rotor surfaces (a), Mesh refinement around blade profile (b).
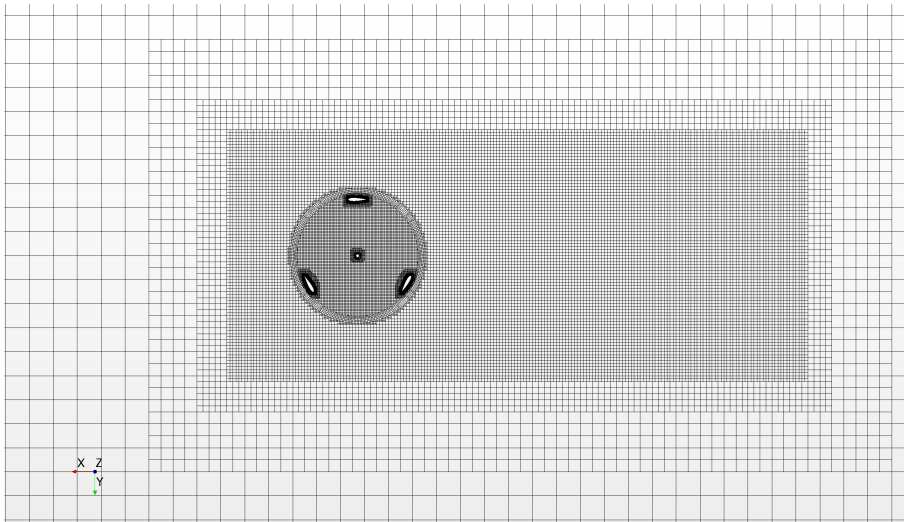
Figure 6.4: Wake and rotating volume mesh refinement.

6.2.4 Wall distance

The height of the first element over the blades surfaces is defined by the number and total thickness of the prism layers used and was set to match the $y^+ \sim 1$ required by the $\gamma - Re_{\theta_t}$ transition model [77] and suggested for the $k - \epsilon$ two layer model used [69].

A second mesh, with a first element height equivalent to $y^+ > 30$, was also generated to ascertain if larger y^+ values (and the associated use of wall functions) improved the predictions of the $k - \epsilon$ model in this scenario.

6.3 Solver settings and simulation process

As with most numerical settings, the solver settings and simulation process were equivalent to those established in the infinite blade study.

Table 6.1: Element size sensitivity.

Number of elements	Blade surface resolution [mm]	C_P	
		Realizable $k - \epsilon$	$k - \omega$ SST
1.1×10^6	1.5	0.110	—
2.4×10^6	1.0	0.145	0.096
4.6×10^6	0.75	0.152	0.120
8.2×10^6	0.55	0.156	0.124

6.4 Comparison with complete turbine numerical results

Before the numerical results were compared with the experimental value, a complete turbine simulation was performed. The mesh used was fundamentally the same, but completely enclosed the entire turbine rotor—i.e., without bisecting it in half. The turbine shaft was also extended until the bottom boundary to better approximate the real rotor structure.

Figure 6.5: C_Q comparison between half and complete turbine rotor.

Both calculations provided the same performance values, $C_P = 0.152$, and the torque curves (Fig. 6.5) show essentially the same behaviour. This established that approximating this specific problem with a domain bisected with a symmetry plane resulted in negligible effects on the performance predictions.
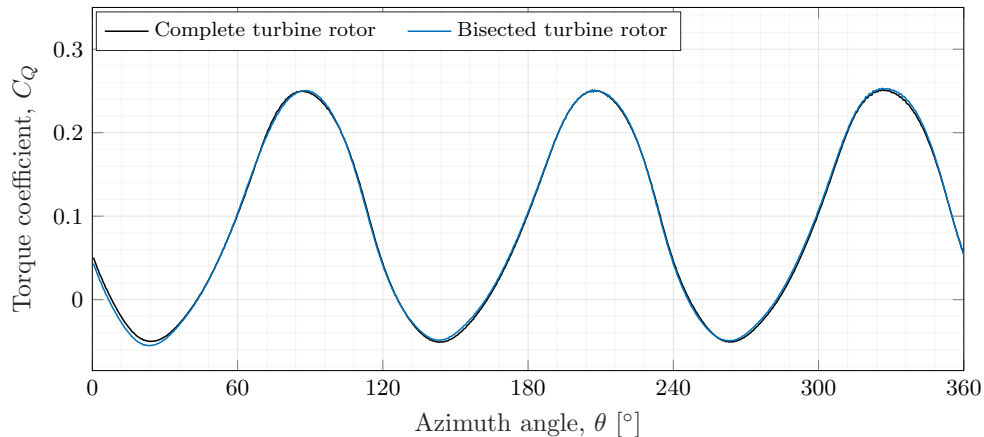
6.5 Validation with experimental results

6.5.1 Turbulence model and mesh resolution

The C_P values, from the mesh resolution sensitivity analysis of both turbulence models, were plotted against the experimental value in figure 6.6. The value obtained in the mesh established in 6.2.3 with the $k - \omega$ SST model without any transition model was also included.

From this comparison it is evident that the $k - \omega$ SST, both with or without the $\gamma - Re_{\theta_t}$ transition model, underestimates the modified turbine's performance.

On the other hand, the C_P predicted with the realizable $k - \epsilon$ seems to show a much better correlation with the experimental value and was, therefore, used in all subsequent calculations.
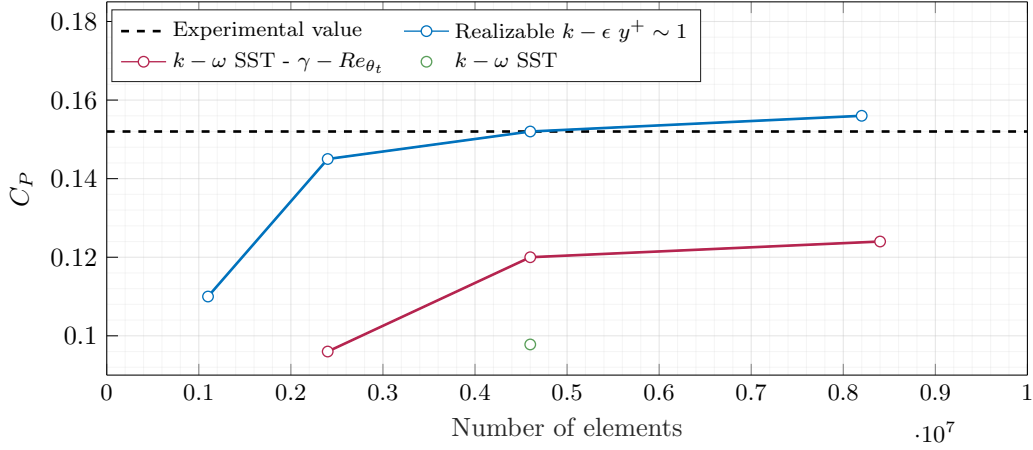
Figure 6.6: Turbulence models' results comparison.

6.5.2 Wall distance

As mentioned in 6.2.4, a mesh with a first cell height (over the blades' surfaces) equivalent to $y^+ > 30$ was also tested with the realizable $k - \epsilon$ model. However, this mesh overpredicted the torque output of the turbine (see table 6.2). As such, the finer mesh equivalent to $y^+ \sim 1$ was used henceforth.

Table 6.2: Turbulence model and y^+ influence on predicted C_P.

Number of elements	Blade surface resolution [mm]	Turbulence model	Blade surface y^+	C_P
4.6×10^6	0.75	$k - \omega$ SST	$\sim 0.1 - 3$	0.098
4.6×10^6	0.75	$k - \omega$ SST - $\gamma - Re_{\theta_t}$	$\sim 0.1 - 3$	0.105
4.6×10^6	0.75	Realizable $k - \epsilon$	$\sim 0.1 - 3$	0.152
3.1×10^6	0.75	Realizable $k - \epsilon$	$\sim 28 - 34$	0.195
Experimental				0.152

In conclusion, this study's numerical settings are summarised in table 6.3.

Table 6.3: Numerical settings used in half-turbine study.

Models and solver settings		Mesh and domain settings	
Software	STAR-CMM+	Number of elements	4.6×10^6
Turbulence model	two-layer realizable $k - \epsilon$		
Solvers		Boundary conditions	
Flow solver	segregated	Inlet	velocity inlet $U_\infty = 8 \ m/s, TI = 1\%$
Pressure-velocity coupling	SIMPLE	Outlet	atmospheric pressure outlet
Convection space discretisation	2nd order upwind	Side, top and bottom (midplane)	symmetry condition
Time discretisation	2nd order implicit unsteady	Moving mesh type	sliding mesh
Time-step	$1.488 \times 10^{-4} \ s$	Minimum cell size	0.75 mm
Inner steps	20	y^+ on blade surfaces	~ 1

6.6   Comparison with infinite blade results

The performance values predicted by the infinite blade calculations were expectedly higher than those obtained with both the finite blade mesh and in the wind tunnel tests (table 6.4), seeing how the former simulations do not include all the losses associated with the blade tip vortices and with the rotor supports.

Table 6.4: C_P comparison with infinite blade simulation results.

Geometry	Mesh	C_P
$\lambda_{vg} = 1/6c$; $A_{vg} = 0.008c$	Infinite blade	0.214
$\lambda_{vg} = 1/6c$; $A_{vg} = 0.008c$	Finite blade	0.152

In fact, by plotting the torque production distribution over the span of one of the blades (from the finite blade simulation), Fig. 6.7, the performance deteriorating effects of the blade tip losses are evident as the C_Q line moves from the mid blade position ($z = 0$) to the blade tip ($z = H/2$).
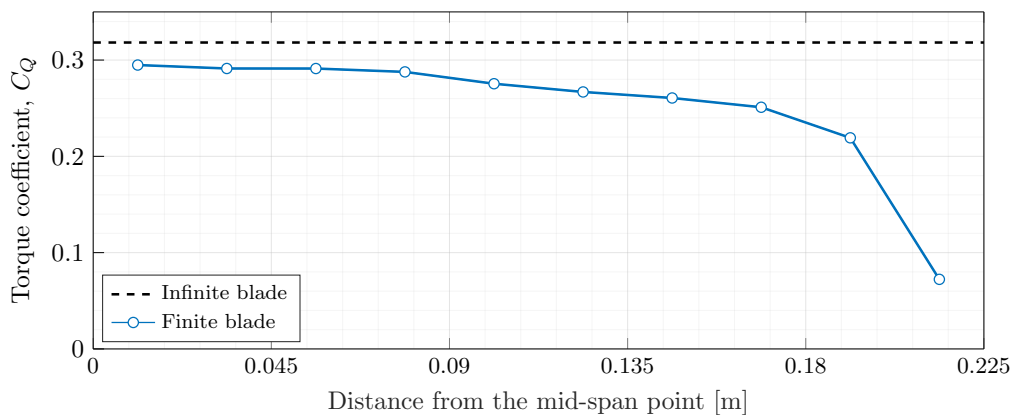

Figure 6.7: Torque comparison with distribution over finite blade span, $\theta = 90°$.

Nevertheless, by comparing the torque coefficient values in the region close to the middle of the blade ($z <\sim 0.05\ m$) with the infinite blade C_Q prediction, the plot indicates that the latter provides a close estimation of the flow behaviour away from the blade tips.

As such, it was established that this infinite blade mesh was suitable for the purpose of choosing a leading edge geometry capable of improving the turbine's performance under dynamic stall conditions, even if the interactions with the blade tip vortex structure were not included.

6.7   Results - dynamic stall process

The following velocity contours and streamlines (Fig. 6.8 - 6.9) were obtained in the mid-span region of the blades ($z = H/2$), away from the blade tip vortices, and show the progressive separation and reattachment of the flow over the blades as the rotor completes one rotation.

The dynamic stall process, in the case of a modified blade at this λ, appears to be similar to the one described in 1.2.2, where, as the angle of attack increases, the trailing edge vortex starts to form, preceded by the reversal of the boundary layer in this section (Fig. 6.8 (b)). At higher incidence angles, a second counter-rotating vortex forms just after the leading edge and progresses downstream (Fig. 6.8 (c)-(d)).

As the blade surpasses the $\theta = 180°$ position and enters the downwind section, the angle of attack

(a) $\theta = 0°$

(b) $\theta = 90°$

(c) $\theta = 120°$

(d) $\theta = 150°$
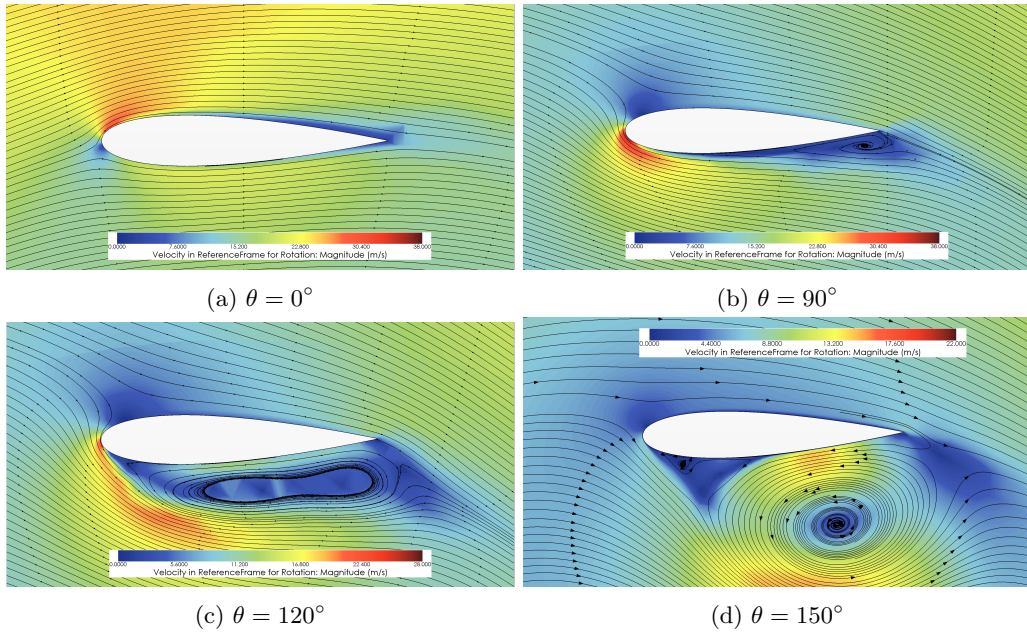
Figure 6.8: Flow separation in the upwind region ($0° < \theta < 180°$).

starts reducing again from its maximum value and the vortex structure over the blade breaks down (Fig. 6.9 (a)-(b)) and the flow reattaches 6.9 (d).

(a) $\theta = 210°$

(b) $\theta = 240°$

(c) $\theta = 270°$

(d) $\theta = 330°$
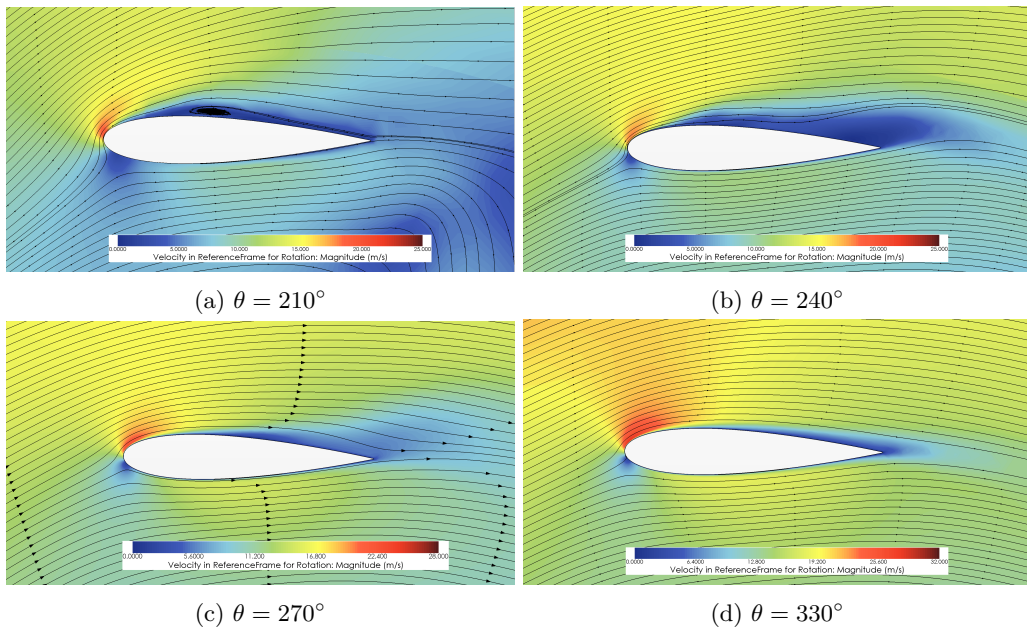
Figure 6.9: Flow reattachment in the downwind region ($180° < \theta < 360°$).

6.8   Results - flow structure over modified blades

The vortex structure over the blades, the tip vortex, and their interaction at $\theta = 120°$ is shown in Fig. 6.10. At this blade position, the flow is fully separated from the suction surface, however, the vortex sections aligned with the leading edge troughs still remain attached until around 0.3c, where the entire structure separates.
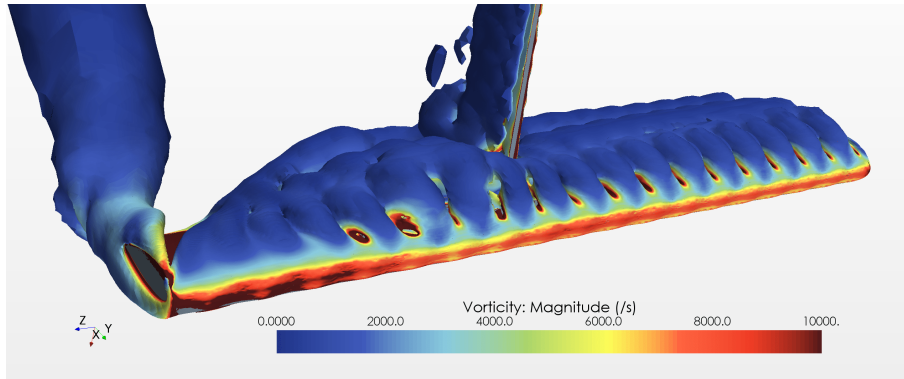
Figure 6.10: Iso-surface Q-criterion$= 1 \times 10^4$ coloured by the vorticity magnitude.

The Q-criterion iso-surface also indicates that the interaction with the tip vortex overpowers the effects of the modified leading edge in a significant portion of the blade span.

In fact, the counter-rotating vortex pairs that travel downstream along the suction side of the blades can be observed by plotting the vectors of the tangential velocity in a plane perpendicular to the chord line and, even though they are visible in the mid-span region of the blade (Fig. 6.11 (b)), the same does not apply near the blade tip. Figure 6.11 (a) shows that this pair of vortices is suppressed by the blade tip vortex structure.

(a) Tip section

(b) Mid-span section
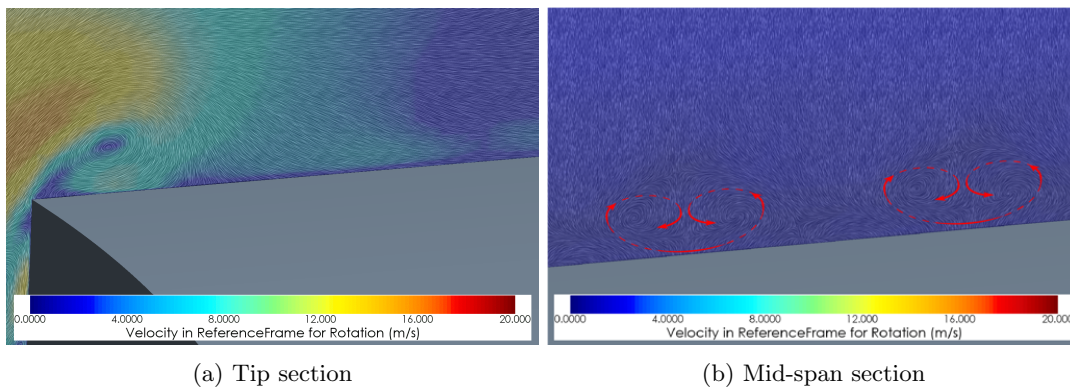
Figure 6.11: Vortex structure over suction side at $\theta = 90°$ - interaction with tip vortex.

Additionally, figure 6.12 displays the velocity streamlines (rotating reference frame) over the suction side at $\theta = 330°$, where the flow is already fully reattached (see Fig. 6.9 (d)). Here, the effects of the vortex pairs seen in Fig. 6.11 (b) can also be observed, especially in the sections aligned with the leading edge troughs, where the transfer of momentum from the higher flow layers to the boundary layer is noticeable.
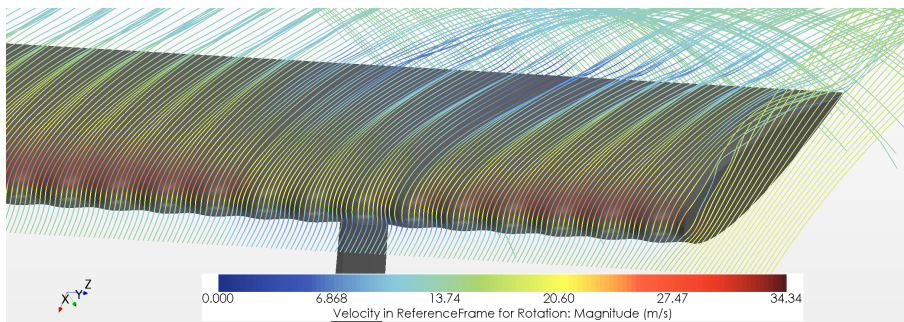
Figure 6.12: Velocity streamlines over modified blade at $\theta = 330°$.

7   Conclusion

The main objective of the work described in this dissertation was to experimentally evaluate the capability of leading edge protuberances to improve the performance and efficiency of a small vertical axis wind turbine in dynamic stall flow conditions. To this date, and to the author's knowledge, no similar experimental analysis of this topic has been published.

This study comprised three main targets: predict the behaviour of the modified blades through numerical models, with enough fidelity to implement a parametric analysis of the leading edge dimensions in the design process; develop an inexpensive but suitable experimental setup to be used in the existing wind tunnel; and lastly, evaluate the performance of the modified turbine and compare it with the baseline behaviour.

7.1   Main conclusions

The main conclusions of this study are:

1. Even though the half-turbine finite blade simulation predicted performance values consistent with the experimental data, a very significant sensitivity to the turbulence models and y^+ values was observed. Further dependency analyses would be required to draw final performance conclusions only from the numerical results.

2. The infinite blade simulations produced good estimates of the flow behaviour in the regions away from the tips in a finite blade and also showed that the leading edge amplitude has a more significant performance influence than the wavelength. Nevertheless, this mesh and models were not capable of predicting the full performance improvements of the modified blades measured in the wind tunnel. In fact, although the real C_P improvement ranged around 20% for $U_\infty = 8$ m/s, this simulations predicted only a 4% increase, possibly due to the lack of the tip vortices interactions and other three-dimensional effects. The absence of blade supports also surely contributed to this discrepancy. Even so, the parametric study made with this mesh produced a significantly improved geometry, with sinusoidal protuberances with $\lambda_{vg} = 1/6c$ and $A_{vg} = 0.8\%$ of the chord.

3. The experimental setup, developed especially for this study, proved adequate for the suitable evaluation of the turbine's performance in the wind tunnel, fulfilling all the prerequisites established in the design process. Particularly, the components and methods used to measure the desired variables showed an acceptable level of uncertainty in the final performance results. 3D printing also proved to be a cost-effective and straightforward manufacturing method for the majority of structural parts and the multiple sets of blades required for the experimental tests.

4. The baseline turbine displayed a relatively low maximum power coefficient, C_P, although in the expected range for a turbine of this dimensions and operating in this conditions.

5. The modified blade geometry tested experimentally ($\lambda_{vg} = 1/6c$; $A_{vg} = 0.008c$) markedly enhanced the start-up performance of the turbine in all wind speeds ($U_\infty = 5.5 - 9\ m/s$). The wind speed at which the turbine fails to start was reduced from $U_\infty = 7\ m/s$ to $U_\infty = 5.5\ m/s$ and the time to reach the maximum rotational speed was essentially reduced by half in the conditions where both turbines were able to self start.

6. Similarly, the leading edge protuberances significantly increased the power output/efficiency of the turbine throughout the whole analysed wind speed spectrum. Between $U_\infty = 5.5\ m/s$ and $U_\infty = 6.5\ m/s$ the modified turbine displayed better performance in the entire tip speed ratio range, with around 40% higher peak C_P values. Above $U_\infty = 7m/s$, the performance gains were in general only noticeable above $\lambda > 1$, where the improvement of the maximum C_P fell from 34% to 20%, as the wind speed was increased until $9\ m/s$.

7. The experimental performance results also showed that the leading edge protuberances did not have a significant effect on the tip speed ratio behaviour—i.e., the modified turbine achieved maximum power output at roughly the same tip speed ratio as the baseline and the λ_{max} only increased by a small margin.

7.2   Future studies

Several other aspects can be analysed to provide further insight on the favourable effects of leading edge protuberances in the performance of small vertical axis wind turbines.

A common solution for the fluctuating torque production and oscillating structural loads, characteristic of straight bladed VAWT designs, is to employ a helical blade configuration (Fig. 7.1) so that the torque ripples of each blade section are distributed throughout the entire rotation cycle.
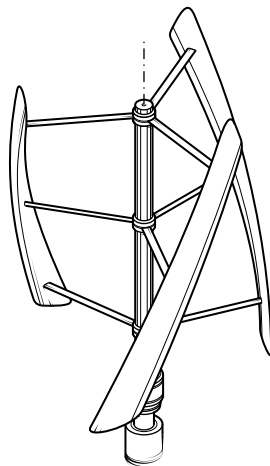
Figure 7.1: Helical (Gorlov) rotor configuration [2].

Since this is a typical VAWT rotor configuration, the interactions of the leading edge protuberances with this design should also be relevant.

A scenario where VAWTs are also known to outperform traditional HAWT designs is in skewed flow [6], where the approaching flow direction is not perpendicular with the vertical axis. It would also be interesting to investigate if the performance gains provided by this leading edge modification also extend to skewed flow conditions, especially considering how the protuberances are aligned with the chord line.

Lastly, analysing the possible applications of this technology in larger diameter VAWTs is also of interest, even if those designs are typically less hindered by dynamic stall losses.

Bibliography

[1] L. Du, "Numerical and Experimental Investigations of Darrieus Wind Turbine Start-up and Operation", Ph.D. dissertation, Durham University, 2016.

[2] R. Bos, "Self-starting of a small urban Darrieus rotor", Ph.D. dissertation, Delft University of Technology, 2012.

[3] E. Möllerström, F. Ottermo, A. Goude, S. Eriksson, J. Hylander, and H. Bernhoff, "Turbulence influence on wind energy extraction for a medium size vertical axis wind turbine", *Wind Energy*, vol. 19, no. 11, pp. 1963–1973, 2016.

[4] S. Mertens, *Wind energy in the built environment: concentrator effects of buildings*. Multi-Science, 2006.

[5] S. Mertens, G. van Kuik, and G. van Bussel, "Performance of an H-Darrieus in the Skewed Flow on a Roof", *Journal of Solar Energy Engineering*, vol. 125, no. 4, pp. 433–440, Nov. 2003.

[6] C. Simao Ferreira, K. Dixon, C. Hofemann, G. van Kuik, and G. van Bussel, "VAWT in Skew: Stereo-PIV and Vortex Modeling", in *47th AIAA Aerospace Sciences Meeting including The New Horizons Forum and Aerospace Exposition*, American Institute of Aeronautics and Astronautics, 2009.

[7] M. Kinzel, Q. Mulligan, and J. O. Dabiri, "Energy exchange in an array of vertical-axis wind turbines", *Journal of Turbulence*, vol. 13, no. 38, pp. 1–13, 2012.

[8] J. O. Dabiri, "Potential order-of-magnitude enhancement of wind farm power density via counter-rotating vertical-axis wind turbine arrays", *Journal of Renewable and Sustainable Energy*, vol. 3, p. 043 104, Jul. 2011.

[9] J. T. Hansen, M. Mahak, and I. Tzanakis, "Numerical modelling and optimization of vertical axis wind turbine pairs: A scale up approach", *Renewable Energy*, vol. 171, pp. 1371–1381, Jun. 2021.

[10] A. Laneville and P. Vittecoq, "Dynamic Stall: The Case of the Vertical Axis Wind Turbine", *Journal of Solar Energy Engineering*, vol. 108, pp. 140–145, May 1986.

[11] J. G. Leishman, *Principles of Helicopter Aerodynamics*, 2nd ed. Cambridge University Press, 2006.

[12] J. W. Larsen, "Nonlinear Dynamics of Wind", Ph.D. dissertation, Aalborg University, 2005.

[13] N. Fujisawa and S. Shibuya, "Observations of dynamic stall on Darrieus wind turbine blades", *Journal of Wind Engineering and Industrial Aerodynamics*, vol. 89, no. 2, pp. 201–214, Feb. 2001.

[14] J. H. Strickland, "The Darrieus turbine, A performance prediction using the double-stream tube analysis", Sandia Laboratories, Tech. Rep. 2, Oct. 1975.

[15] B. F. Blackwell, R. E. Sheldahl, and L. V. Feltz, "Wind tunnel performance data for the Darrieus wind turbine with NACA 0012 blades.", Sandia Laboratories, Tech. Rep. May, 1976.

[16] M. H. Worstell, "Aerodynamic Performance of the DOE/Sandia 17-m-Diameter Vertical-Axis Wind Turbine.", *Journal of energy*, vol. 5, no. 1, pp. 39–42, 1981.

[17]   T. D. Ashwill, "Measured data for the Sandia 34-meter vertical axis wind turbine", Sandia National Laboratories, Tech. Rep. SAND91-2228, 1992.

[18]   A. Bianchini, G. Ferrara, and L. Ferrari, "Design guidelines for H-Darrieus wind turbines: Optimization of the annual energy yield", *Energy Conversion and Management*, vol. 89, pp. 690–707, Jan. 2015.

[19]   A. Rezaeiha, H. Montazeri, and B. Blocken, "Towards optimal aerodynamic design of vertical axis wind turbines: Impact of solidity and number of blades", *Energy*, vol. 165, pp. 1129–1148, Dec. 2018.

[20]   L. Du, G. Ingram, and R. G. Dominy, "Experimental study of the effects of turbine solidity, blade profile, pitch angle, surface roughness, and aspect ratio on the H-Darrieus wind turbine self-starting and overall performance", *Energy Science & Engineering*, vol. 7, no. 6, pp. 2421–2436, Dec. 2019.

[21]   W. Joo, B.-S. Lee, K. Yee, and D.-H. Lee, "Combining Passive Control Method for Dynamic Stall Control", *Journal of Aircraft*, vol. 43, no. 4, pp. 1120–1128, Jul. 2006.

[22]   L. W. Carr, K. W. Mcalister, and N. Ames, "The Effect of a Leading-Edge Slat on the Dynamic Stall of an Oscillating Airfoil", in *AlAA Aircraft Design, Systems and Technology Meeting*, 1983.

[23]   D. Baldacchino, C. Ferreira, D. D. Tavernier, W. Timmer, and G. J. W. van Bussel, "Experimental parameter study for passive vortex generators on a 30% thick airfoil", *Wind Energy*, vol. 21, no. 9, pp. 745–765, Sep. 2018.

[24]   C. Zhu, J. Chen, J. Wu, and T. Wang, "Dynamic stall control of the wind turbine airfoil via single-row and double-row passive vortex generators", *Energy*, vol. 189, Dec. 2019.

[25]   C. Zhu, T. Wang, and J. Wu, "Numerical Investigation of Passive Vortex Generators on a Wind Turbine Airfoil Undergoing Pitch Oscillations", *Energies*, vol. 12, no. 4, Feb. 2019.

[26]   D. De Tavernier, C. Ferreira, A. Viré, B. LeBlanc, and S. Bernardy, "Controlling dynamic stall using vortex generators on a wind turbine airfoil", *Renewable Energy*, vol. 172, pp. 1194–1211, Jul. 2021.

[27]   T. Lee and P. Gerontakos, "Unsteady Airfoil with Dynamic Leading- and Trailing-Edge Flaps", *Journal of Aircraft*, vol. 46, no. 3, pp. 1076–1081, May 2009.

[28]   P. Gerontakos and T. Lee, "Dynamic Stall Flow Control via a Trailing-Edge Flap", *AIAA Journal*, vol. 44, no. 3, pp. 469–480, Mar. 2006.

[29]   J. L. McCloud III, L. P. Hall, and J. A. Brady, "Full-scale wind-tunel tests of blowing boundary layers control applied to a helicopter rotor", National Aeronautics and Space Administration, Tech. Rep., 1960.

[30]   M. A. Karim and M. Acharya, "Suppression of dynamic-stall vortices over pitching airfoils by leading-edge suction", *AIAA Journal*, vol. 32, no. 8, pp. 1647–1655, 1994.

[31]   J. C. Magill and K. R. Mcmanus, "Control of Dynamic Stall using Pulsed Vortex Generator Jets", American Institute of Aeronautis and Astronautics, Tech. Rep., 1997.

[32]   J. Yen and N. A. Ahmed, "Enhancing vertical axis wind turbine by dynamic stall control using synthetic jets", *Journal of Wind Engineering and Industrial Aerodynamics*, vol. 114, pp. 12–17, Mar. 2013.

[33]   R. Firdaus, T. Kiwata, Kono Takaaki, and K. Nagao, "Numerical and experimental studies of a small vertical-axis wind turbine with variable-pitch straight blades", *Journal of Fluid Science and Technology*, vol. 10, no. 1, 2015.

[34] D. S. Miklosovic, M. M. Murray, L. E. Howle, and F. E. Fish, "Leading-edge tubercles delay stall on humpback whale (Megaptera novaeangliae) flippers", *Physics of Fluids*, vol. 16, no. 5, p. L39, May 2004.

[35] F. E. Fish, P. W. Weber, M. M. Murray, and L. E. Howle, "The Tubercles on Humpback Whales' Flippers: Application of Bio-Inspired Technology", *Integrative and Comparative Biology*, vol. 51, no. 1, pp. 203–213, Jul. 2011.

[36] J. T. Hrynuk and D. G. Bohl, "The effects of leading-edge tubercles on dynamic stall", *Journal of Fluid Mechanics*, vol. 893, A5, Jun. 2020.

[37] J. Camara and J. Melo De Sousa, "Numerical Study on the Use of a Sinusoidal Leading Edge for Passive Stall Control at Low Reynolds Number", in *51st AIAA Aerospace Sciences Meeting including the New Horizons Forum and Aerospace Exposition*, American Institute of Aeronautics and Astronautics, 2013.

[38] J. L. E. Guerreiro and J. M. M. Sousa, "Low-Reynolds-Number Effects in Passive Stall Control Using Sinusoidal Leading Edges", *AIAA Journal*, vol. 50, no. 2, pp. 461–469, Feb. 2012.

[39] N. Rostamzadeh, K. L. Hansen, R. M. Kelso, and B. B. Dally, "The formation mechanism and impact of streamwise vortices on NACA 0021 airfoil's performance with undulating leading edge modification", *Physics of Fluids*, vol. 26, no. 10, p. 107 101, Oct. 2014.

[40] H. Johari, C. Henoch, D. Custodio, and A. Levshin, "Effects of Leading-Edge Protuberances on Airfoil Performance", *AIAA Journal*, vol. 45, no. 11, pp. 2634–2642, Nov. 2007.

[41] A. Esmaeili, H. E. Delgado, and J. M. Sousa, "Numerical simulations of low-Reynolds-Number flow past finite wings with leading-Edge protuberances", in *Journal of Aircraft*, vol. 55, American Institute of Aeronautics and Astronautics Inc., 2018, pp. 226–238.

[42] W. Ke, I. Hashem, W. Zhang, and B. Zhu, "Influence of leading-edge tubercles on the aerodynamic performance of a horizontal-axis wind turbine: A numerical study", *Energy*, vol. 239, p. 122 186, Jan. 2022.

[43] G.-Y. Huang, Y. Shiah, C.-J. Bai, and W. Chong, "Experimental study of the protuberance effect on the blade performance of a small horizontal axis wind turbine", *Journal of Wind Engineering and Industrial Aerodynamics*, vol. 147, pp. 202–211, Dec. 2015.

[44] Y.-N. Zhang, H.-J. Cao, and M.-M. Zhang, "Investigation of leading-edge protuberances for the performance improvement of thick wind turbine airfoil", *Journal of Wind Engineering and Industrial Aerodynamics*, vol. 217, p. 104 736, 2021.

[45] Z. Wang and M. Zhuang, "Leading-edge serrations for performance improvement on a vertical-axis wind turbine at low tip-speed-ratios", *Applied Energy*, vol. 208, pp. 1184–1197, Dec. 2017.

[46] Z. Wang, Y. Wang, and M. Zhuang, "Improvement of the aerodynamic performance of vertical axis wind turbines with leading-edge serrations and helical blades using CFD and Taguchi method", *Energy Conversion and Management*, vol. 177, pp. 107–121, Dec. 2018.

[47] Y. Yan, E. Avital, J. Williams, and J. Cui, "Aerodynamic performance improvements of a vertical axis wind turbine by leading-edge protuberance", *Journal of Wind Engineering and Industrial Aerodynamics*, vol. 211, p. 104 535, Apr. 2021.

[48] B. K. Kirke, "Evaluation of Self-Starting Vertical Axis Wind Turbines for Stand-Alone Applications", Ph.D. dissertation, Griffith University, 1998.

[49] R. Gosselin, G. Dumas, and M. Boudreau, "Parametric study of H-Darrieus vertical-axis turbines using CFD simulations", *Journal of Renewable and Sustainable Energy*, vol. 8, no. 5, Sep. 2016.

63

[50] Q. Li, T. Maeda, Y. Kamada, J. Murata, K. Furukawa, and M. Yamamoto, "Effect of number of blades on aerodynamic forces on a straight-bladed Vertical Axis Wind Turbine", *Energy*, vol. 90, pp. 784–795, Oct. 2015.

[51] P. Delafin, T. Nishino, L. Wang, and A. Kolios, "Effect of the number of blades and solidity on the performance of a vertical axis wind turbine", in *Journal of Physics: Conference Series*, vol. 753, 2016.

[52] R. Dominy, P. Lunt, A. Bickerdyke, and J. Dominy, "Self-starting capability of a Darrieus turbine", *Proceedings of the Institution of Mechanical Engineers, Part A: Journal of Power and Energy*, vol. 221, no. 1, pp. 111–120, Feb. 2007.

[53] S. Brusca, R. Lanzafame, and M. Messina, "Design of a vertical-axis wind turbine: how the aspect ratio affects the turbine's performance", *International Journal of Energy and Environmental Engineering*, vol. 5, no. 4, pp. 333–340, Dec. 2014.

[54] Q. Li, T. Maeda, Y. Kamada, *et al.*, "Effect of rotor aspect ratio and solidity on a straight-bladed vertical axis wind turbine in three-dimensional analysis by the panel method", *Energy*, vol. 121, pp. 1–9, Feb. 2017.

[55] S. Roy, H. Branger, C. Luneau, D. Bourras, and B. Paillard, "Design of an Offshore Three-Bladed Vertical Axis Wind Turbine for Wind Tunnel Experiments", in *Volume 10: Ocean Renewable Energy*, vol. 10, American Society of Mechanical Engineers, Jun. 2017.

[56] A. Sagharichi, M. Zamani, and A. Ghasemi, "Effect of solidity on the performance of variable-pitch vertical axis wind turbine", *Energy*, vol. 161, pp. 753–775, Oct. 2018.

[57] S. Worasinchai, "Small Wind Turbine Starting Behaviour", Ph.D. dissertation, Durham University, 2012.

[58] A. J. Fiedler and S. Tullis, "Blade Offset and Pitch Effects on a High Solidity Vertical Axis Wind Turbine", *Wind Engineering*, vol. 33, no. 3, pp. 237–246, May 2009.

[59] K.W. McLaren, "Unsteady loading of high solidity vertical axis wind turbines", Ph.D. dissertation, McMaster University, 2011.

[60] L. Zou, K. Wang, Y. Jiang, A. Wang, and T. Sun, "Wind Tunnel Test on the Effect of Solidity on Near Wake Instability of Vertical-Axis Wind Turbine", *Journal of Marine Science and Engineering*, vol. 8, no. 5, p. 365, May 2020.

[61] R. E. Sheldahl, P. C. Klimas, and L. V. Feltz, "Aerodynamic performance of a 5-metre-diameter Darrieus turbine with extruded aluminum NACA-0015 blades.", Sandia Laboratories, Tech. Rep., 1980.

[62] R. Bravo, S. Tullis, and S. Ziada, "Performance testing of a small vertical-axis wind turbine", *21st Canadian Congress of Applied Mechanics CANCAM*, no. June 2007, pp. 2–3, 2007.

[63] S. Armstrong, A. Fiedler, and S. Tullis, "Flow separation on a high Reynolds number, high solidity vertical axis wind turbine with straight and canted blades and canted blades with fences", *Renewable Energy*, vol. 41, pp. 13–22, May 2012.

[64] C. Masson, C. Leclerc, and I. Paraschivoiu, "Appropriate Dynamic-Stall Models for Performance Predictions of VAWTs with NLF Blades", *International Journal of Rotating Machinery*, vol. 4, no. 2, pp. 129–139, 1998.

[65] T. M. Kirk, "The Later Stages of Transition over a NACA0018 Airfoil at a Low Reynolds Number", M.S. thesis, University of Waterloo, 2014.

[66] Z. Yi-Nan, C. Hui-Jing, and Z. Ming-Ming, "A calculation method for modeling the flow characteristics of the wind turbine airfoil with leading-edge protuberances", *Journal of Wind Engineering and Industrial Aerodynamics*, vol. 212, May 2021.

[67] W. P. Jones and B. E. Launder, "The Prediction of Laminarization With a Two-Equation Model of Turbulence.", *International Journal of Heat and Mass Transfer*, vol. 15, pp. 301–314, 1973.

[68] W. Rodi, "Experience with two-layer models combining the k-epsilon model with a one-equation model near the wall", in *29th Aerospace Sciences Meeting*, American Institute of Aeronautics and Astronautics, 1991.

[69] Siemens Digital Industries Software, *Simcenter STAR-CCM+ User Guide, version 2020.2*. 2020.

[70] T. H. Shih, W. W. Liou, A. Shabbir, Z. Yang, and J. Zhu, "A new k-ϵ eddy viscosity model for high reynolds number turbulent flows", *Computers & Fluids*, vol. 24, no. 3, pp. 227–238, Mar. 1995.

[71] D. C. Wilcox, "Reassessment of the scale-determining equation for advanced turbulence models", *AIAA Journal*, vol. 26, no. 11, pp. 1299–1310, Nov. 1988.

[72] F. R. Menter, "Two-equation eddy-viscosity turbulence models for engineering applications", *AIAA Journal*, vol. 32, no. 8, pp. 1598–1605, Aug. 1994.

[73] G. Ren, J. Liu, J. Wan, F. Li, Y. Guo, and D. Yu, "The analysis of turbulence intensity based on wind speed data in onshore wind farms", *Renewable Energy*, vol. 123, pp. 756–766, Aug. 2018.

[74] A. Rezaeiha, I. Kalkman, and B. Blocken, "CFD simulation of a vertical axis wind turbine operating at a moderate tip speed ratio: Guidelines for minimum domain size and azimuthal increment", *Renewable Energy*, vol. 107, pp. 373–385, Jul. 2017.

[75] D. Y. Ohm, "Dynamic model of pm synchronous motors", Tech. Rep., 2000.

[76] H. W. Coleman and W. G. Steele, *Experimentation, Validation, and Uncertainty Analysis for Engineers*, 4th ed. John Wiley & Sons, 2018.

[77] R. B. Langtry, "A Correlation-Based Transition Model Using Local Variables for Unstructured Parallelized CFD codes", Ph.D. dissertation, University of Stuttgart, 2006.